ABSTRACT

A STUDY OF THE EVENT STRUCTURE IN HIGH P_T DIRECT PHOTON AND π^0 PRODUCTION BY 515 GeV/c π^- AND 800 GeV/c PROTON BEAMS INCIDENT ON NUCLEAR TARGETS

Woo-Hyun Chung, Ph.D.

University of Pittsburgh, July 1995

We present the results from a study of hadronic jets in association with high p_t direct photons and π^0's using 515 GeV/c π^- and 800 GeV/c proton beams incident on various nuclear targets. The data used in this analysis were collected during the 1990 and 1991 fixed target runs using the E706 spectrometer at Fermilab. The spectrometer, which triggered on a high transverse momentum electromagnetic deposition, consists of a finely segmented large acceptance liquid argon calorimeter and a large acceptance charged particle spectrometer. Both trigger and recoil jets were reconstructed from direct photon and π^0 events using a standard algorithm.

We measure the fragmentation function of the recoiling jets, and study the correlation between the trigger jet and the recoil jet for both the direct photon and π^0 event samples with different beam types. The results are compared with the predictions of HERWIG Monte Carlo simulations.

ACKNOWLEDGEMENTS

First and foremost, I wish to thank my wife Youmie for her love, support and patience. She always helped to brighten up the gray tiring days with her beautiful smile.

I would like to express my sincere thanks to my advisers, Paul Shepard and Gene Engels for their support and encouragement during my stay in Fermilab. I am greatly indebted to Gene Engels for his suggestions and comments throughout this thesis project.

Special thanks to my mentor Suhdindra Mani for his guidance and friendship. Many thanks to George Ginther and Marek Zielinski for their advice and encouragement on countless occasions.

I would also like to thank my fellow graduate students and post-docs: Lenny Apanasevich, John Bacigalupi, David Brown, Michael Begel, Richard Benson, Steve Blusk, Paoti Chang, Brajesh Choudhary, Lucy de Barbaro, Wiesiek Dlugosz, Jim Dunlea, Sajan Easo, keith Hartman, Vijay Kapoor, Chris Lirakis, Andre Maul, John Mansour, George Osborne, Rob Roser, Dane Skow, Lee Sorrell, David Striley, Nikos Varelas, Dhammika Weerasundara, Carlos Yosef and Vishnu Zutshi. They all make my work in E706 enjoyable.

Last but not least I owe a great debt of gratitude to my parents for their love, sacrifice and encouragement.

TABLE OF CONTENTS

LIST OF FIGURES

LIST OF TABLES

CHAPTER 1

Introduction

1.1 Parton Model and QCD

Over the last three decades our understanding of the fundamental nature of matter has undergone a revolution. Since the early deep-inelastic scattering experiment at SLAC[1] [1], a series of experimental discoveries has firmly established the subnuclear world of *quarks* and *leptons*. It is now clear that the proton, the neutron, and other hadrons are not elementary. Instead, they are composite systems made up of constituents called quarks [2] [3], much as an atom is a composite system made up of electrons and a nucleus. So far, there are known to be six varieties, or *flavors* of quarks, labelled as d (down), u (up), s (strange), c (charm), b (bottom) and t (top) for historical reasons. These spin $\frac{1}{2}$ fermions are grouped into three distinct doublets, or generations.

$$Quarks: \begin{pmatrix} u \\ d \end{pmatrix}, \begin{pmatrix} c \\ s \end{pmatrix}, \begin{pmatrix} t \\ b \end{pmatrix} \tag{1.1}$$

The top row has electric charge $q = \frac{2}{3}e$ and the bottom row has $q = -\frac{1}{3}e$, where e is the magnitude of the electron's electric charge.

[1]Stanford Linear Accelerator Center

Unlike the neutron and the proton, the electron has survived the revolution intact as an elementary constituent of matter, structureless and indivisible. However, we now know that there are six electron-like particles called leptons. The flavors of leptons are also arranged in three families of doublets,

$$Leptons: \begin{pmatrix} \nu_e \\ e \end{pmatrix}, \begin{pmatrix} \nu_\mu \\ \mu \end{pmatrix}, \begin{pmatrix} \nu_\tau \\ \tau \end{pmatrix} \tag{1.2}$$

The electron(e), muon(μ), and tau(τ) have electric charge -e, and each is associated with a neutrino of electric charge zero. According to our present understanding, then, ordinary matter is composed of quarks and leptons which are all spin 1/2 fermions.

It is known that a formidable interaction, called the *strong force*, binds quarks together into hadrons but does not influence leptons. Both quarks and leptons are acted upon by the other three fundamental forces: the electromagnetic force, the weak force and the gravitational force. For each interaction, the force between particles is mediated by another class of particles. Since the quantum field theory that allows us to calculate the behavior of the particles is a *gauge* theory, they are called gauge bosons. These gauge bosons have integral spins. These *mediators* include photons for the electromagnetic force, $W^{\pm}$ and Z^0 for the weak force, and *gluons* for the strong force. Quarks and gluons are collectively called *partons*.

So far, only two types of hadrons made from combinations of quarks are known. The *baryons* are bound states of three quarks (qqq) and the *mesons* are bound states formed by a quark-antiquark pair ($q\bar{q}$). In order to preserve the Pauli exclusion principle in the formation of baryons, a new quantum number called *color* [4] was introduced. Quarks carry three primary color charges and combine to make color neutral (colorless) hadrons. Gluons mediate the strong interaction between color charged particles, just as photons mediate the electromagnetic interaction between electrically charged particles. While photons have no electric charge, gluons carry

color charges and can thus interact directly with other gluons. The gauge theory of the strong force acting between color charges among the partons is called Quantum Chromodynamics (QCD) in analogy with Quantum Electrodynamics (QED). The property of QCD is defined by the non-Abelian SU(3) color symmetry [5].

The important property of QCD which distinguishes it from QED is asymptotic freedom [6] [7]. This term is used to describe the weakening of the effective quark-gluon coupling at short distances or, equivalently, large momentum transfers. The property of asymptotic freedom allows the application of well-known perturbative techniques to the problem of obtaining predictions for processes that are dominated by short-distance interactions. This is exactly why high p_T processes play an important role in testing QCD.

1.2 QCD and High P_T Phenomena

In QCD, the hard scattering process between two hadrons is described as the interaction between quarks and gluons which are the constituents of the incoming hadrons. Figure 1.1 shows a schematic illustration of a high p_T hadronic interaction. The distribution function $G_{a/A}(x)$ represents the probability of finding a parton a in hadron A with momentum fraction lying between x and $x + dx$. The fragmentation function $D_{C/c}(z)$ represents the probability of obtaining hadron C with momentum fraction between z and $z + dz$ from parton c.

The parton distribution and fragmentation functions cannot be calculated using perturbation theory and thus must be determined by measurements using some reference process. The distribution functions are often determined by measurements made in deep-inelastic lepton-nucleon scattering, and fragmentation functions are often studied in e^+e^- annihilation or deep-inelastic scattering.

In the parton model, hard scattering is described by the lowest order subpro-

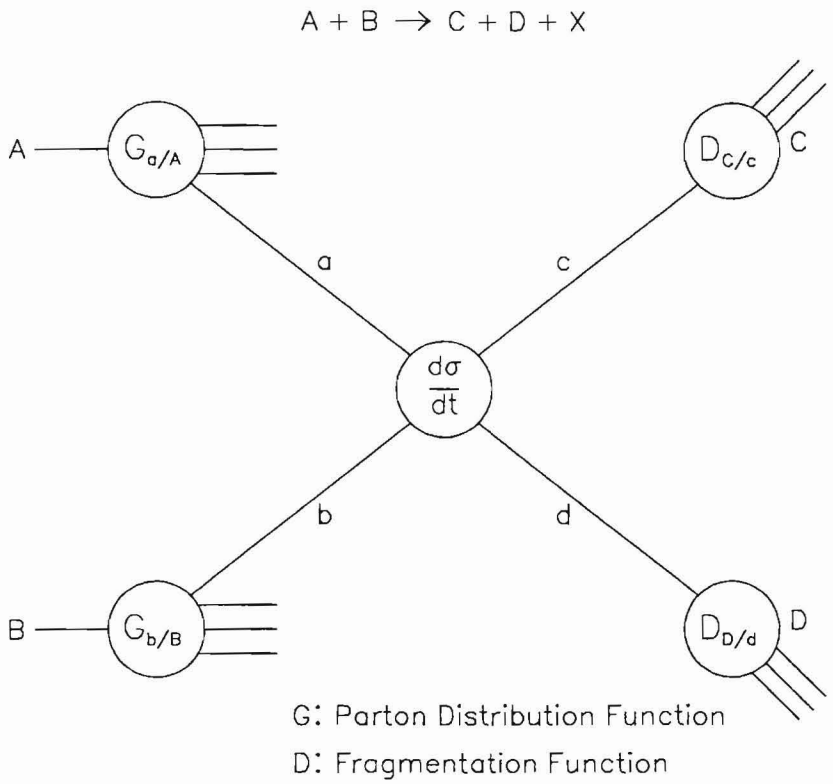

Figure 1.1: Schematic illustration of a high p_T reaction factorized into parton distribution functions (G), parton fragmentation functions (D), and a hard-scattering subprocess.

cesses which are two-body scatterings. If the calculations are made to all orders of perturbation theory, and only the leading logarithmic contribution from each order is retained, this is called the leading logarithmic approximation. If it is assumed that the initial and final partons are collinear and the partons are massless, then the expression for the invariant cross section in the leading logarithmic approximation [8] is

$$E_C \frac{d\sigma}{d^3p_C}(AB \to C + X) = \sum_{abcd} \int dx_a dx_b dz_c G_{a/A}(x_a) G_{b/B}(x_b) D_{C/c}(z_c) \frac{\hat{s}}{z_c^2 \pi} \frac{d\sigma}{d\hat{t}}(ab \to cd) \delta(\hat{s} + \hat{t} + \hat{u}), \tag{1.3}$$

where x_a and x_b are the fraction of longitudinal momentum carried by parton a in hadron A and parton b in hadron B respectively, and z is the fraction of momentum of parton c carried by hadron C.

The leading order expression for the strong interaction [9] coupling constant is given by

$$\alpha_s(Q^2) = \frac{12\pi}{(11N_c - 2n_f)\ln(Q^2/\Lambda^2)} \tag{1.4}$$

where n_f is the number of quark flavors and N_c is the number of colors. Q^2 represents the momentum transfer and Λ is the momentum scale which is not predicted by the theory but is determined by experiments. If a process involves a large momentum transfer ($Q^2 \to \infty$), α_s becomes small. Then one can calculate perturbatively the hard scattering of the hadron constituents. When Q^2 is small ($\sim \Lambda^2$), α_s becomes large and the perturbation expansion breaks down. Thus in the long distance interaction, quarks and gluons arrange themselves into strongly bound clusters, namely, hadrons.

1.3 High P_T Photon Physics

In high p_T hadron-hadron interactions, QCD predicts the emergence of jets[2]. Jets result from the process of hadronization, wherein the scattered partons are converted to the hadrons appearing in the final state. Since the four-vector of the jet is closely related to that of the parent partons, one can extract the physics of constituent interactions by studying jet production. However, aside from the experimental difficulties of such a task, there are inherent theoretical ambiguities in the definitions of jets that limit the use of this procedure, particularly for quantitative studies. Also, there is a large number of subprocesses to disentangle. It is, therefore, of interest to consider a process in which one can directly constrain the underlying kinematics of a small number of subprocesses. Direct photon production is such a reaction.

1.3.1 Direct Photon Physics

The term "direct photon" describes a photon that is directly involved in a hard scatter, as opposed to a photon from the production of a hadron that subsequently decays electromagnetically. There are advantages in studying high p_T direct photons produced in the hard scattering of hadron constituents. The reasons for the continuing interest in the study of direct photon physics are:

- There are only two first order subprocesses: the *Compton* diagram ($qg \rightarrow \gamma q$) and *annihilation* diagram ($q\bar{q} \rightarrow \gamma g$).

- The electromagnetic coupling of the quark-photon vertex is well understood.

[2]The term *jet* refers to a collimated collection of hadrons emerging from the hard scattering reaction.

- To first order, direct photons are not accompanied by additional hadrons, hence the measurements can be directly compared to theory without the complication of a fragmentation function. Experimentally, the kinematics of the direct photon can be measured with good precision.

In the Compton diagram, a gluon is involved in the initial state, whereas in the annihilation diagram, a gluon appears in the final state. If the contributions from these two leading-order graphs can be isolated, direct photon production can be used to extract information on both gluon fragmentation and on the gluon structure of hadrons (i.e., the momentum distribution of gluons within hadrons).

The relative importance of the Compton and the annihilation diagram in direct photon production depends mainly on the incident beam particle type and the kinematic region. In pp interactions, for example, the Compton diagram should be the dominant one because of the lack of antiquark content in the proton. However, in $\bar{p}p$ or $\pi^- p$ collisions, because of the enhanced possibility of $\bar{u}u$ (valence) interactions, the ratio of annihilation to Compton production increases with increasing x_T ($= 2p_T/\sqrt{s}$) [10]. So, for sufficiently high p_T ($\sim 6\ GeV$ at $\sqrt{s} \sim 30\ GeV$), the annihilation diagram dominates.

1.3.2 High P_T π^0 Physics

Experimentally, studies of direct photon production suffer from potentially large backgrounds. The source of high p_T background photons can be largely attributed to high p_T production (and subsequent electromagnetic decay) of mesons such as π^0 and η. The primary contribution comes from π^0's. In high p_T photon physics, it is very important to understand π^0 production in order to estimate precisely its contribution to the background associated with direct photon events.

Extracting direct photon signals is technically challenging because of the greatly

reduced yield of direct photons and the substantial background from π^0 and η mesons. Fortunately, it is expected that the γ/π^0 production ratio will increase with p_T because the photon carries away the entire p_T of the parton, whereas π^0's and η's are fragments of the emerging hard scattered partons.

1.4 Jet Studies

Even though inclusive direct photon production provides a valuable test of QCD, the simultaneous measurement of the triggering direct photon and the recoiling away-side jet allows the underlying parton-level kinematics to be more tightly constrained.

1.4.1 Fragmentation

In spite of the success of perturbative QCD to describe many experimental observations, it is still not very well known how the unobservable quarks and gluons transit to the physically observable hadrons (the so-called hadronization, or fragmentation process). This is a complex sequence of low-Q^2 processes for which the techniques of perturbative QCD are not applicable and phenomenological models must be used. It is thus important to obtain experimental insight into the fragmentation process using reactions where the primary parton dynamics are well known. High p_T direct photon production, because of its basic simplicity, is well suited for this purpose.

In QCD, gluons carry a larger color charge than quarks and should radiate more soft gluons and thus fragment into more particles than quarks [11]. This leads to the expectation that gluon jets have a softer particle energy spectrum, a larger angular width and a larger particle multiplicity than quark jets from partons of the same energy [12].

As discussed in the previous section, in pp collision, direct photon production is dominated by the Compton process. Consequently, away-side jets should be mainly

fragments of quarks, in fact, primarily of u quarks. On the other hand, sufficiently high p_T direct photons in $\bar{p}p$ or $\pi^- p$ collisions, are dominantly from the annihilation process and gluon jets should be more abundant in the away-side than in the case of pp collisions.

Thus it should be interesting to compare the results of direct photon events with those of π^0 triggering di-jet events for different incident beam types.

1.4.2 Angular Distribution

The measurement of the angular distribution of the di-jet system can be expressed as a differential cross section with respect to $\cos\theta^*$, where θ^* is the parton-parton center of mass scattering angle. Assuming that the incident hadrons are collinear, this can be determined experimentally by a boost from the laboratory frame to the di-jet rest frame, and θ^* becomes the polar angle between the di-jet axis and the hadron-hadron axis.

Since the dominant two-body parton-parton scattering subprocesses have either $t-$ and/or $u-$ channel poles (e.g., $qq \to qq$) or a sum of $s-$, $t-$ and $u-$ channel poles (e.g., $gg \to gg$, $gq \to gq$), the angular distributions are sharply peaked in the forward and backward directions. A parametrization of the angular dependence is given by

$$\frac{d\sigma}{d\cos\theta^*} \Big/ \frac{d\sigma}{d\cos\theta^*}\Big|_{\cos\theta^*=0} = \frac{1}{2}\left[\frac{1}{(1+\cos\theta^*)^a} + \frac{1}{(1-\cos\theta^*)^a}\right]. \qquad (1.5)$$

The exponent a has been determined by fitting over the range $|\cos\theta^*| \leq 0.5$ for different subprocesses [8]. According to [8], the values of a corresponding to $gg \to gg$, $gq \to gq$, and $qq \to qq$, are 2.02, 2.15, and 2.6, respectively. Perturbative QCD predicts much flatter behavior for the Compton subprocess ($a = 0.9$ due to the fact that it has an $s-$ channel and a $u-$ channel pole term, but no $t-$ channel term).

Thus, if the angular distributions of di-jet events and direct photon events are

compared, there is expected to be a substantial difference. This expectation has been verified by several other experiments [13] [14] which demonstrated very good agreement with the predictions.

1.4.3 Nuclear Effects

Since the first observation of the "anomalous nuclear enhancement" effect in proton-nucleus collisions [15], a large body of data has been accumulated on nuclear target effects in a wide variety of processes. They include di-jet production [16] [17], dihadron production [18], Drell-Yan [19], deep inelastic muon scattering [20] [21] and low p_T hadron production [22]. In this pioneering experiment, it was observed that the cross section per nucleus (σ_A) could be parametrized as

$$\sigma_A = \sigma_0 A^\alpha \tag{1.6}$$

where A is the atomic mass of the target nucleus and σ_0 is a constant. For high p_T collisions, the data have shown that $\alpha > 1$ for p_T's above 2 GeV/c, while α is generally 2/3 for low p_T interactions. A value of α greater than 1 is generally understood as due to soft multiple scattering of the hard-scattered partons as they exit the nucleus. Thus, the measurement of nuclear effects in high p_T scattering is believed to provide a unique opportunity to study the behavior of partons traversing nuclear matter. Recent experiments in di-jet production reported that the multiple nuclear scattering of the outgoing quarks can broaden the back-to-back azimuthal correlation of the outgoing di-jets. Their experimental results using jet analysis show that the angular width of a jet is nearly independent of A and the broadening of the correlation in the azimuthal angle of the di-jet system for a heavy target is caused almost entirely by nuclear scattering of the partons. The broadening of the di-jet azimuthal angular correlation can be parametrized by the variable $k_{t\phi}$, which is related to a single component of the vector p_T imbalance of the di-jet system. $k_{t\phi}$

is defined as

$$k_{t\phi} = \frac{p_{T1} + p_{T2}}{2} \cdot \sin(\Delta\phi) \tag{1.7}$$

where p_{T1} and p_{T2} are the transverse momentum components of two jets and $\Delta\phi$ is the azimuthal opening angle between the two jets. The kinematic variable $k_{t\phi}$ is known to be more directly sensitive to the effects of multiple scattering of partons [23]. The experimentally measured $k_{t\phi}$ is interpreted as a quadratic sum of $k_{t\phi}$ for a nucleon target, $k_{t\phi}$(nuclear) and an instrumental and jet finding contribution to $k_{t\phi}$.

1.5 Thesis Goals

The goal of this thesis is to report the results of studying hadronic jets associated with high p_T direct photons or π^0's using π^- and p beams incident upon nuclear targets. First, we investigate the characteristics of charged particles in the recoil jet by studying the fragmentation function. This is an effort to observe the difference between quark and gluon jets by comparing the fragmentation functions of the jets recoiling against direct photons and π^0's with two different beam types. As discussed earlier, the recoil jets in the direct photon events are expected to be predominantly gluon jets when using a π^- beam, but expected to be mostly quark jets with a p beam. The jets recoiling from the high p_T π^0's with both beam types are also compared with the recoil jets from the direct photon events. The Monte Carlo program (HERWIG [24]) is fully utilized not only to give both perturbative QCD predictions but also to be compared with the data after full detector simulation (GEANT [25]).

Second, the angular distribution of the di-jet events is studied in the parton center of mass system by correlating trigger jet and recoil jet. This study is focused on the comparison of the $\cos\theta^*$ distributions for direct photon events and the di-jet

events containing π^0's as trigger particles. The $\cos\theta^*$ distribution of direct photon events is expected to be much flatter than that of di-jet events because direct photon production is dominanted by the subprocesses with spin 1/2 quark propagators. The results are compared with perturbative QCD calculations using a Monte Carlo program.

As a last subject in this thesis, we extend the correlation study of the di-jet system to the study of the nuclear effects by measuring the azimuthal angular correlation of trigger and recoil jets. The azimuthal correlation of di-jets is investigated as a function of nuclear target mass and the broadening of the correlation is measured by the quantity $k_{t\phi}$. The results are compared with those from other experiments.

CHAPTER 2

The E706 Spectrometer

The E706 spectrometer was located in the Meson West (MWEST) experimental hall and included a downstream muon detector. The muon detector was primarily used by experiment E672, which was an experiment designed to study massive dimuon pairs. The layout of the spectrometer in MWEST is shown in Figure 2.1.

The MWEST spectrometer includes a beam transport system, a charged particle tracking system, a liquid argon calorimeter, a forward calorimeter and the muon detector. The major parts of the charged particle tracking system are:

- A variety of nuclear targets
- A Silicon Strip Detector (SSD) system
- An Analysis Magnet
- A Proportional Wire Chamber (PWC) system
- A Straw Drift Chamber system.

The calorimetry consists of:

- A Liquid Argon Calorimeter (LAC) with Electromagnetic (EMLAC) and Hadron sections (HALAC)

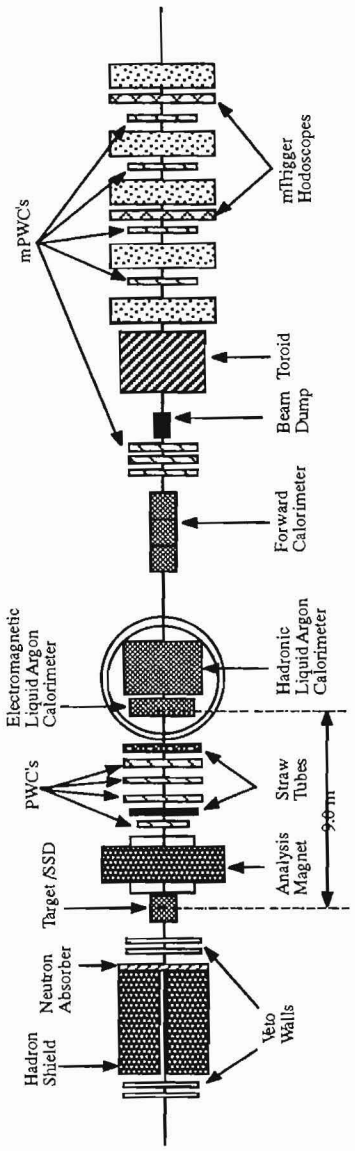

Figure 2.1: Layout of the MWEST spectrometer.

- A Forward Calorimeter (FCAL).

2.1 The Meson West Beamline

The Meson West (MW) beam line was designed to transport both 800 GeV/c primary protons and secondary beams with a momentum range from 25 to 1000 GeV/c. The primary proton beam with momentum 800 GeV/c was extracted from the Fermilab main accelerator, called the Tevatron, and delivered to the MW beam line for 23 seconds per accelerator cycle, followed by 35 seconds between spills. The secondary beam was produced by the interaction of primary protons with a 1.14 interaction length Be target. The positive or negative secondary beams of the desired momenta were obtained by controlling the polarity and magnitude of the beam line magnet current.

During the 1990 run, a negative secondary beam of $\sim$ 515 GeV/c was delivered. In the 1991 run, there were three different beam types: a $\sim$ 530 GeV/c secondary beam with negative and positive polarities and an $\sim$ 800 GeV/c primary proton beam. The 515 GeV/c negative beam consisted of $\sim$ 97% π^- and $\sim$ 3% K^-, while the positive 530 GeV/c beam consisted of $\sim$ 91% p, $\sim$ 7% π^+ and less than 2% K^-. The differential Cerenkov counter, located 90 m upstream of the target region, can be used to tag those incident particle types.

To reduce the background triggers due to muons generated along the beamline incident on the spectrometer, the beamline was equipped with spoiler magnets. μ muons were deflected away from the spectrometer by these spoiler magnets which had three inch diameter vacuum pipes surrounded by soft steel. A 4.7 m long steel hadron shield was located at the front end of the MWEST spectrometer to absorb hadrons in the beam halo. Three scintillation counter veto walls[1], one upstream and

[1]During 1991 run, the fourth veto wall was added

two downstream of the hadron shield, were installed to identify the remaining muons. Neutrons produced in the hadron shield were absorbed in a water tank placed at the downstream end of the hadron shield.

2.2 The Target Region

Upstream of the E706 target, a set of scintillation counters, called the beam hodoscope and beam hole counter, was positioned to define incident beam particles. The beam hodoscope consisted of three view planes (X, Y and U) with overlapping 12 paddles each, covering 2×2 cm^2 area. The beam hole counter was placed just after the beam hodoscope along the beam line, and had an 1 cm radius hole centered on the beam.

Four interaction counters (SE1, SW1, SE2, and SW2) upstream and downstream of the analysis magnet identified interactions from the target region. SE1 and SW1 covered 7.6×15.2 cm^2 and had an 1.9 cm diameter hole between them centered around the beam axis, while SE2 and SW2 covered 10.2×20.4 cm^2 with a 3.8 cm diameter hole.

E706 used nuclear targets, to study nuclear dependence of the production of neutral mesons, direct photons and jets. Be and Cu were used for both the 1990 and 1991 runs and a liquid hydrogen target was added for the 1991 run. Figure 2.2 shows the configurations of the target for the 1990 and 1991 runs.

The 1990 target consisted of two sheets of Cu and two Be pieces of cylindrical shape. During the 1991 run, there were two sheets of Cu followed by the liquid hydrogen of interaction length 50.8 g/cm^2 sandwiched between two Be windows and another Be piece downstream of the Be window. Table 2.1 and 2.2 present the characteristics of each target piece.

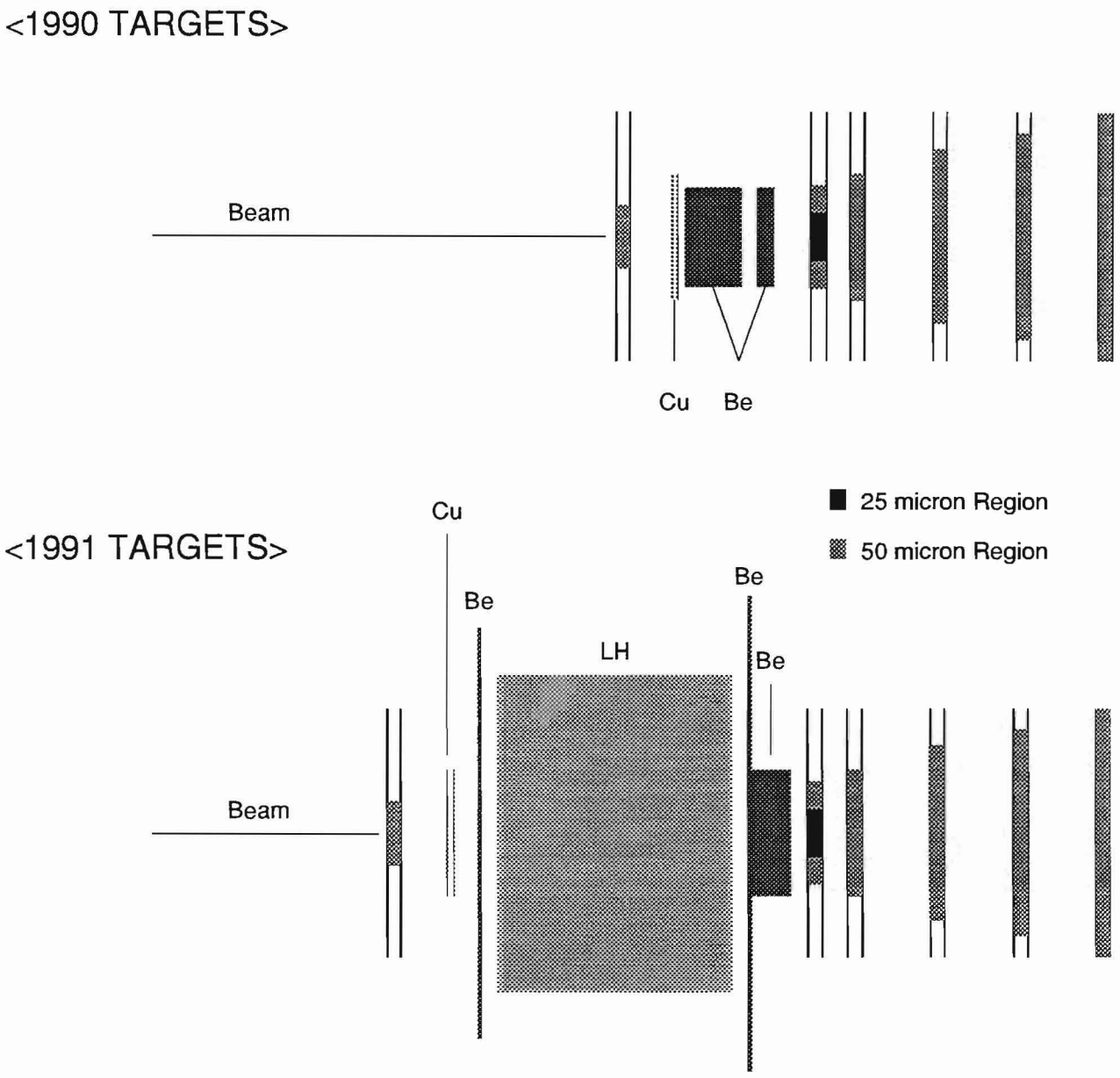

Figure 2.2: Layout of the target for the 1990 and 1991 runs.

Target	z Position (cm)	Thickness (cm)	Radius (cm)
Be 1	-9.36	1.12	1.0
Be 2	-12.81	3.71	1.0
Cu 1	-15.18	0.08	1.27
Cu 2	-15.50	0.08	1.27

Table 2.1: The E706 targets (1990 run).

Target	z Position (cm)	Thickness (cm)	Radius (cm)
Be 1	-8.95	2.54	1.27
Be 2	-10.38	0.28	4.76
Liquid H	-19.31	15.49	3.18
Be 3	-28.24	0.25	4.18
Cu 1	-29.91	0.08	1.27
Cu 2	-30.40	0.08	1.27

Table 2.2: The E706 targets (1991 run).

2.3 The Tracking System

2.3.1 The Silicon Strip Detectors

The SSD system [26] consisted of 8 pairs of planes, 3 for the beam chambers upstream of the target and 5 for the vertex chambers downstream of the target. Each pair consisted of X and Y view planes. The 6 planes (3 per view) in the beam chambers were used to identify beam tracks and 10 planes in the vertex SSD served for determining the primary and secondary vertex positions as well as for charged track finding and momentum measurement through linking at the center of the magnet with the downstream tracks found by the PWC-STRAW system. The characteristics of the SSD wafers are given in Table 2.3.

All the planes in the beam chamber had $3 \times 3\ cm^2$ wafers with 50 μm pitch size while the planes in the vertex chamber had 5×5 wafers with 25 and 50 μm pitch size. The instrumented number of strips for vertex chamber planes was roughly designed to maximize the coverage of the interaction occurred around the target area. The first module of the vertex chambers was designed to have finer pitch size (25 μm) for the inner part of the wafer and 50 μm pitch for the outer part. This was intended to improve the resolution of tracks and reduce the ambiguities in the pattern recognition stage, especially for the study of heavy quark physics.

A detailed description of the properties and the construction of the Silicon Strip Detector and its readout system can be found in [27].

2.3.2 The Analysis Magnet

The analysis magnet, located downstream of the vertex SSD chambers was designed to produce a dipole magnetic field of 6.2 kG which centered about 2 m downstream of the target. The operating current during 1990 and 1991 runs was $\sim$ 1050

Module	Plane Number	Wafer Size (cm^2)	Instrumented Region(cm)	Number of Strips	Strip Width (μm)
1 X	1	3×3	±0.64	256	50
1 Y	2	3×3	±0.64	256	50
2 X	3	3×3	±0.64	256	50
2 Y	4	3×3	±0.64	256	50
3 X	5	3×3	±0.64	256	50
3 Y	6	3×3	±0.64	256	50
4 X	7	5×5	±0.48	384	25
			±0.64	256	50
4 Y	8	5×5	±0.48	384	25
			±0.64	256	50
5 X	9	5×5	±1.28	512	50
5 Y	10	5×5	±1.28	512	50
6 X	11	5×5	±1.76	704	50
6 Y	12	5×5	±1.76	704	50
7 X	13	5×5	±2.08	832	50
7 Y	14	5×5	±2.08	832	50
8 X	15	5×5	±2.5	1000	50
8 Y	16	5×5	±2.5	1000	50

Table 2.3: SSD wafer parameters.

amperes, which generated a 444 MeV/c transverse momentum impulse in the horizontal plane. A helium bag was placed in the aperture of the magnet to minimize the effects of multiple Coulomb scattering. In order to eliminate fringe field effects on SSD and PWC chambers and improve the uniformity of dipole field, the mirror plates were installed on both ends of the magnet.

2.3.3 The Proportional Wire Chambers

The Proportional Wire Chambers (PWC) system [31] was located between the analysis magnet and the Liquid Argon Calorimeter (LAC) and consisted of 4 modules. Each module had X, Y, U and V view planes with wires rotated -90, 0, 37 and -53 degrees with respect to the vertical direction around beam axis.

Each of X-Y and U-V views formed a coordinate system with Z direction of the experiment which is the nominal direction of the beam. This configuration was designed to find the trajectory of charged particles in 3 dimensions and to reduce the ambiguity in pattern recognition. The positions of planes and the number of wires instrumented can be found in [30]. The active area of the chambers varied from $1.22 \times 1.22\ cm^2$ to $2.44 \times 2.44\ cm^2$.

In each view plane, the anode plane was surrounded by two cathode planes and the separations was 5.74 mm. The anodes were made of gold plated tungsten wire with 20 μm diameter and the cathodes were graphite coated 25 μm thick mylar sheets stretched and glued to G-10 frames.

In order to decrease the sensitivity of the anode wires in the high rate central beam region, each cathode plane was divided into three electrically different regions with independent high voltage settings: the central beam region, diffractive region and main region. Their sizes in each module are listed in Table 2.4.

As an ionizing medium, the PWC gas mixture was composed of 80% argon, 18% isobutane, 1.5% isoprophyl alcohol vapor and 0.1% freon.

	Beam		Diffractive		Main	
	X	Y	X	Y	X	Y
Module 1	2.54	2.54	15.2	15.2	162.6	121.9
Module 2	3.81	3.81	20.3	20.3	203.2	203.2
Module 3	3.81	3.81	20.3	20.3	203.2	203.2
Module 4	5.08	5.08	30.5	30.5	243.8	243.8

Table 2.4: Regions of Cathode Segmentation in PWC Modules.

2.3.4 The Straw Drift Tubes

The Straw Drift Tubes system consisted of two different chambers and each chamber had 4 X and 4 Y view planes. The first chamber was placed between PWC module 1 and PWC module 2 and the second chamber between PWC module 4 and the LAC. The number of tubes and tube sizes are listed in Table 2.5.

Module	Number of Tubes	Length of Tubes	Diameter of Tubes
1x (4 planes)	160*4	1.67 m	10.4 mm
1y (4 planes)	128*4	1.26 m	10.4 mm
2x (4 planes)	160*4	2.80 m	15.9 mm
2y (4 planes)	160*4	2.80 m	15.9 mm

Table 2.5: Straw Tubes Parameters

The individual straw tube was made from two spiral wrapped layers of 76 μm mylar with 7.6 μm of aluminum coating on the inner surface. The anode was made of gold plated tungsten wire with 20 μm diameter and stretched with a tension of 50 gm. These straw tubes were glued together to make bundles and there were 16 (10 to 11) tubes per each bundle in module 1 (module 2). Detailed information on the

construction of the straw chambers is given in [32]. The mixture of gas, as an ionizing medium, was 50% argon and 50% ethane, bubbled through 0^0C ethyl alcohol. The readout system of the straw chambers employed Time-to-Digital Converters (TDCs) and integrated with the LAC readout system.

2.3.5 The Liquid Argon Calorimeter

The liquid argon calorimeter (LAC), located 9 m downstream of the target, was designed not only to measure the position and energy deposition of high p_T showers but also to serve as a major component of the trigger system. The LAC was divided into two sections: an electromagnetic section (EMLAC) and a hadronic section (HALAC). The LAC was enclosed in a steel cryostat and suspended from a mobile gantry as shown in Figure 2.3. A comprehensive description of the construction and the design of the LAC can be found in [33] and [34].

The EMLAC

The EMLAC had an annular shape with inner radius of 20 cm and outer radius of 165 cm which covered polar angle $1.3^0 < \theta < 10^0$ in the lab coordinate system. The readout pattern of the EMLAC used the polar (r - ϕ) geometry. As shown in Figure 2.4, it was divided into four independent quadrants, each of which consisted 33 r layers interleaved with 33 ϕ layers. The total thickness of the EMLAC was 75 cm which was about 30 radiation lengths. Each layer contained a 2 mm thick lead sheet and 1.59 mm thick double sided copper-clad G-10 anode board, both surrounded by 2.5 mm liquid argon gaps. The lead sheets were of quadrant size and the G-10 anode boards were of octant size. The lead sheet served both as absorber and high voltage cathode.

The r boards had concentric strips centered around beam axis which were focused at the target area 900 cm upstream of the face of the EMLAC. As a result of this

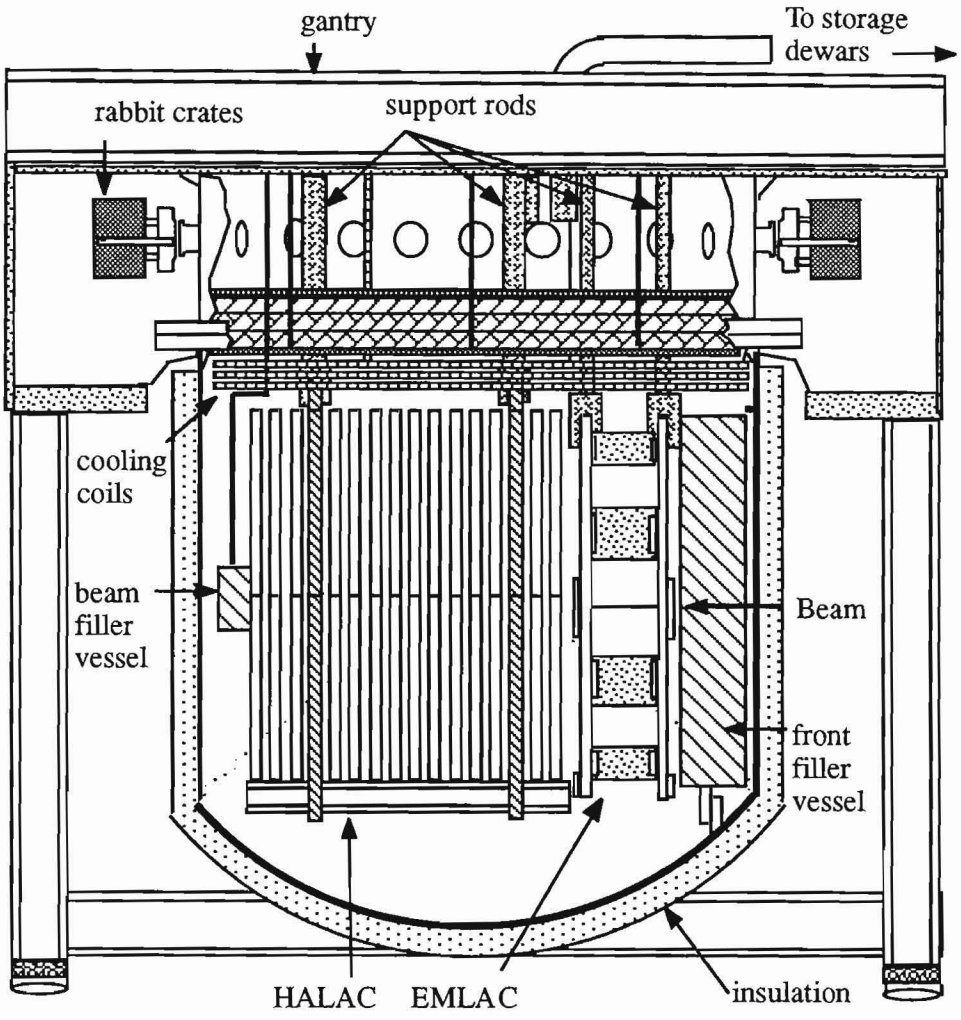

Figure 2.3: A side view of the LAC.

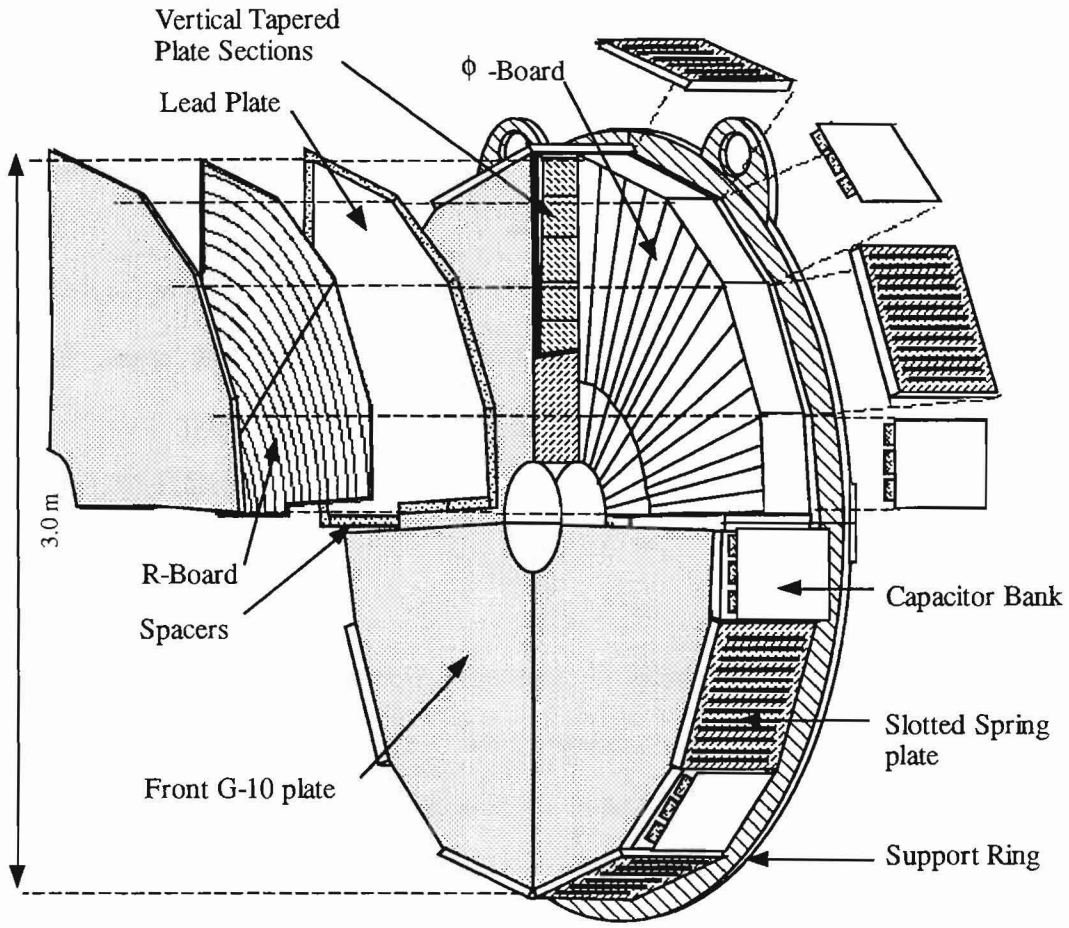

Figure 2.4: Exploded view of the EMLAC.

focusing, the width of strips on an r board increased with depth, so that a shower originating from the target area could pass through the same sequential r strips in each successive r board.

The ϕ board was divided into inner and outer regions by a boundary at a radius of 40.2 *cm* from the center. A strip covered an azimuthal angle of $\pi/192$ in the inner region, and $\pi/384$ in the outer region.

The EMLAC was divided into two sections for the purpose of readout electronics, the front section with 22 layers and the back section with 44 layers. This longitudinal segmentation was useful to discriminate hadronic showers from electromagnetic showers. There were total of 6272 readout channels in the EMLAC.

The HALAC

The HALAC [35], located downstream of the EMLAC, was designed to measure the position and energy of charged and neutral hadrons. The HALAC was $\sim$ 8 interaction length deep and used steel as absorber. There were 52 layers, each of which contained a 2.54 *cm* thick steel plate and 0.32 *cm* liquid argon gap, followed by a readout module, called *cookie* (see Figure 2.5).

One extra cookie was placed in front of the first steel plate to provide a total of 53 cookies. Each cookie was made of 7 layers of G-10 glued together, including two high voltage planes interleaved with 3.2 *mm* G-10 strips, two anode readout boards and vertical G-10 ribs. The high voltage planes were made of 0.8 *mm* double sided copper-clad G-10. The inner side was held at high voltage while the outer side was grounded. The two readout boards were made of single sided copper-clad G-10 boards with vertical G-10 ribs between them. The charge collection pads on the anode boards were cut into equilateral triangles to minimize the X–Y correlation problem during reconstruction. The size of pads was determined to contain 93 % of hadron shower energy in a hexagon formed by six pads and increased longitudinally

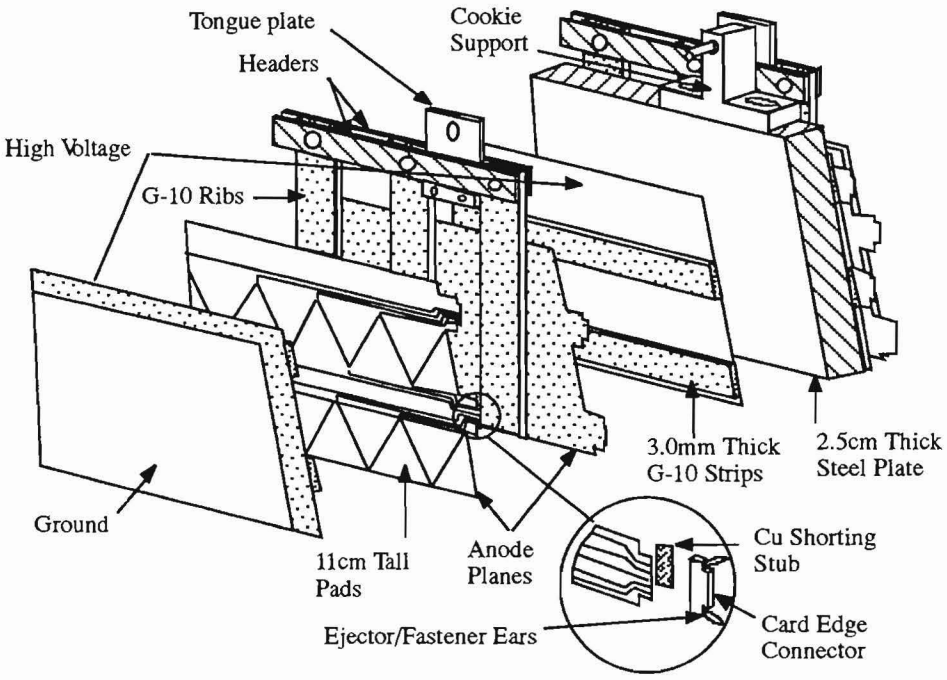

Figure 2.5: Structure of the HALAC cell.

to provide a geometry focused on the target. The readout of the HALAC was also separated into two sections. The front section contained 14 cookies and 13 absorber plates, and the rest of them in the back section.

2.3.6 The Forward Calorimeter

The FCAL [36], located downstream of the LAC ($\sim$ 17 m from the target), was designed to measure the energy and the p_T of the beam jets which were not detected by the LAC or the charged tracking system. The FCAL had three modules, each of which included 28 circular steel absorber plates with thickness of 19 mm, sandwiched with 4.6 mm thick acrylic scintillator sheets (see Figure 2.6).

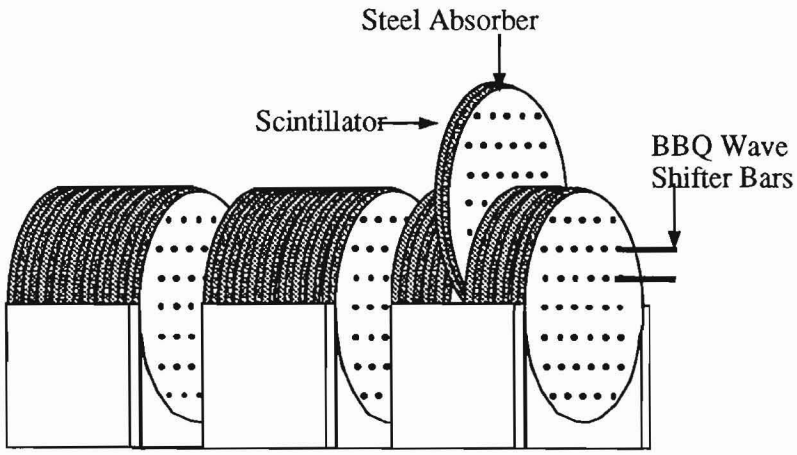

Figure 2.6: The Forward Calorimeter

CHAPTER 3

The E706 Trigger and DA

3.1 Data Acquisition System

The basic structure of the MWEST data acquisition (DA) system is illustrated in Figure 3.1.

The DA system consisted of μVAX, PDP-11 series mini computers and FASTBUS. A μVAX played a central role of controlling other slave modules and recorded the data to the storage medium. The PDP-11's, as front ends of the DA system, were used to read in the data from the various subsystems through serial and parallel CAMAC links. There were three PDP-11's:

- NEU : for the readout of the SSD's, PWC's, trigger system and the scalers.
- ROCH : for the readout of the FCAL.
- MU : for the readout of the E672 di-muon system.

The FASTBUS [37] system was used for LAC and STRAW's readout system. The data read out by those slave modules were concatenated by the μVAX and recorded on the 8 mm magnetic tapes. This whole procedure was controlled by the multilevel program, called VAXONLINE which was a Fermilab on-line data acquisition package.

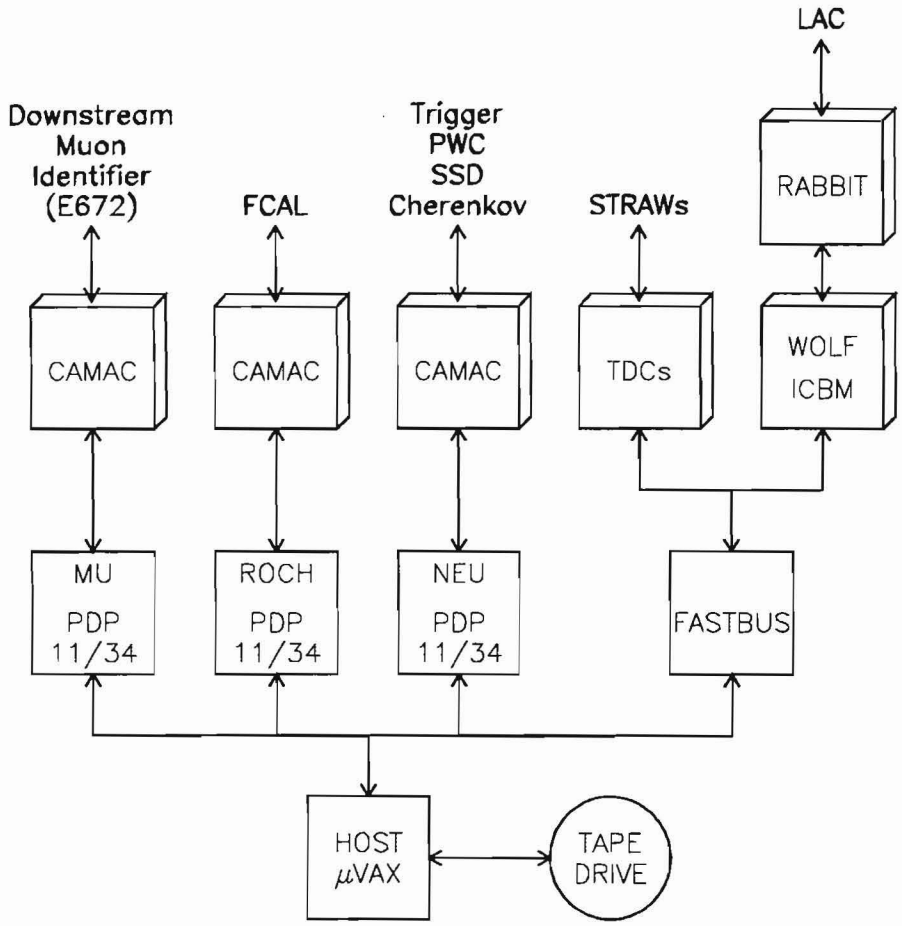

Figure 3.1: Block diagram of the MWEST DA system.

VAXONLINE was run on a μVAX and consisted of four parts:

1. *GLOBAL_MENU* was the menu driven user interface for all VAXONLINE process.
2. *RUN_CONTROL* was the user interface to control and coordinate data taking process.
3. *EVENT_BUILDER* concatenated the data from subsystems and assembled complete event on the μVAX.
4. *OUTPUT* took the events from the staging pool and recorded them to the specified medium.
5. *BUFFER_MANAGER* was a process which sent a fraction of concatenated events to other computers for on-line monitoring.

The design and the operation of the DA system was described in detail in [39] and [38].

3.2 The E706 Trigger

The trigger system in E706 was designed to select events containing high p_T electromagnetic showers. Most of trigger system was controlled by the NEU PDP-11 and various trigger parameters such as delay times, prescale factors and trigger types were loaded through RUN_CONTROL in the DA system. The event selection process were divided into three basic steps:

- Beam and Interaction Definition
- Pretrigger : preliminary p_T measurement
- Trigger : final p_T measurement

A detailed description of the E706 trigger system can be found in [40].

3.2.1 Beam and Interaction

The definition of the 'beam' and the 'interaction' was made by utilizing the information from the accelerator control, beam hodoscope, beam hole counter and interaction counters. The beam from the accelerator was delivered in 23 *sec* spills separated by 35 *sec* acceleration periods. The signal indicating the beginning and end of beam spills was used to generate beam gate (*BMGATE*) signals. The *RF_CLOCK* signal represented the beam structure with a frequency of $\sim$ 53 MHz and was in phase with the accelerator. Also used was the beam hodoscope signal, requiring signals from at least two planes in the same time bucket. Therefore a triggerable beam particle was defined as

$$BEAM1 = (BeamHodoscope) \otimes BMGATE \otimes RF\_CLOCK \qquad (3.1)$$

The interaction (*INTERACTION*) was defined by requiring signals from at least two interaction counters in the same time bucket in coincidence with the beam signal. A *CLEAN* interaction signal was generated when there were no interactions within ± 3 time buckets ($\sim \pm 60$ ns) from a given interaction. In addition to this, the absence of a signal from the beam hole counter ($\overline{BH}$) combined with the computer ready signal (*CMPRDY*) specifying that DA system is ready for taking data, were used in defining a *live triggerable interaction.*

$$LIVE\_INT = BEAM1 \otimes INTERACTION \otimes CLEAN \otimes \overline{BH} \otimes CMPRDY \qquad (3.2)$$

3.2.2 Pretrigger

The pretrigger was designed to provide a fast estimate of the electromagnetic p_T deposited in the LAC and minimize overall trigger deadtime. In each individual LAC octant, *PRETRIGGER* was defined by the coincidence of the following:

- *LIVE_INT*

- Total p_T deposition in the inner or outer section of the octant exceeds 1.7 GeV/c.
- Total p_T in the octant within the previous 200 ns was less than 1.5 GeV/c.
- No signal from the veto wall $(VW1 + VW2) \otimes VW3$.
- Absence of a power supply noise spike (*SCRKILL*).

3.2.3 Final Trigger

In the final stage of the LAC trigger, three different p_T sum signals were used by the trigger logic:

- GLOBAL – total p_T deposited in one octant
- 1/2 GLOBAL – total p_T deposited in the inner or outer region in one octant
- LOCAL – sum of p_T deposited in 16 consecutive r strips ($\sim$ one photon shower width)

Two different p_T threshold levels (*HI* and *LO*) were used with those three p_T signals to generate the following triggers:

- LOCAL GLOBAL HI : the local p_T was above the local *LO* threshold and the global p_T was above the global *HI* threshold in the same octant.
- LOCAL GLOBAL LO : the local p_T was above the local *LO* threshold and the global p_T was above the global *LO* threshold in the same octant.
- SINGLE LOCAL HI : the local p_T was above the local *HI* threshold.
- SINGLE LOCAL LO : the local p_T was above the local *LO* threshold.

- LOCAL 1/2 GLOBAL_HI : the local p_T was above the local LO threshold and the global p_T, either in the inner half octant or in the outer half octant, was above the global HI threshold in the same octant.

- TWO GAMMA : there are at least two distinct octants which satisfy the SINGLE LOCAL LO requirement and the octant pair must be separated from each other by at least two octants.

The generation of at least one of the above triggers sent an *interrupt* signal to the DA system, otherwise, sent the *reset* signal and made the trigger ready for the new event within ~ 20 μs.

CHAPTER 4

Event Reconstruction

The E706 data contain raw information which has gone through discrimination and digitization processes. The results from the reconstruction pass were stored in the Data Summary Tapes (DST's) and then subjected to physics analysis. The main reconstruction code MAGIC [41] is a multi-task program which is designed to accomplish the following:

- Read raw data from tapes
- Convert raw data into physical coordinates and energy measurements
- Perform pattern recognition necessary to identify charged particles and photons based upon information from unpacked data
- Writes out summary output to DST

MAGIC, written primarily in FORTRAN-77 employing the PATCHY [42] code management package for its development and maintenance, used the memory management package ZEBRA [43] for dynamic memory allocation. There were six major reconstructers called from MAGIC in the first pass data processing. They were independent of each other and each reconstructed a specific part of the MWEST spectrometer:

- DLREC (Discrete Logic REConstructor) for trigger logic and Cerenkov detector reconstruction,
- PLREC (PLanes REConstructor) for the reconstruction of charged particles
- EMREC (Electro-Magnetic REConstructor) for the reconstruction of the electromagnetic showers in EMLAC
- HCREC (Hadron Calorimeter REConstructor) for the reconstruction of the hadron showers in HALAC
- FCREC (Forward Calorimeter REConstructor) for the reconstruction of the energy detected in FCAL
- MUREC (MUon REConstructor) for the reconstruction of the muons which penetrated the entire spectrometer

4.1 Charged Particle Reconstruction

Charged tracks were reconstructed by the program called PLREC. This program was divided into several subprograms: PWC tracking, STRAW tracking, SSD tracking, beam tracking, linking and vertex finding. The PWC and STRAW tracking reconstructed tracks downstream of the analysis magnet. Then, track finding in the vertex SSD chambers was performed along with linking at the center of the magnet. Linking was not only important for determining the momentum of tracks, but also helped identify high quality SSD tracks to be used later for vertex finding. The beam tracking was done independently, but the beam track information was helpful in locating the primary vertex.

4.1.1 Downstream Tracking

PWC Tracking

The downstream tracking begins with PWC view track finding. Using 4 planes in each independent view (X, Y, U or V), the view tracks were reconstructed following the steps below:

1. Choose two alternate sets of trial seed planes and investigate each of the possible straight lines determined by connecting a hit from each of those planes.

2. For each straight line, search for hits in the other planes within a window size of 1.5 wire spacing.

3. If more than one hit existed within an window, using a straight line χ^2 fit, select 3 and 4-hit view tracks which passed the χ^2_{dof} cuts (2.0 for 3-hit and 3.0 for 4-hit tracks).

Once all the view track candidates were identified in all 4 views, the selection of candidate space tracks was made by correlating view tracks in X–Y and U–V views separately. Below is the procedure for identifying 3-dimensional space track candidates.

1. A pair of X and Y view tracks served as a candidate space track, correlating X and Y view tracks.

2. Each X–Y space track candidate was projected to the U and V planes in search of hits in the U and V planes within a 1.5 wire spacing window.

3. The same steps were repeated by projecting U–V space track candidates to the X and Y planes but using a window size of 1.0 wire spacing.

4. Using the hits within a search window, all X–Y and U–V space track were refitted. The minimum required number of hits per track was 13. After the

refitting procedure, χ^2_{dof} cuts were applied (2.0 for 13-hit tracks and 3.0 for 14, 15 and 16-hit tracks).

5. Comparing the slopes and intercepts of X–Y and U–V space tracks, the duplicate tracks were removed.

High quality tracks satisfied the following criteria:

- The Y view impact parameter at the center of the target was less than 2.5 cm.
- 16-hit tracks shared fewer than 13 hits with other tracks
- 15-hit tracks shared fewer than 11 hits with other tracks
- 14-hit tracks shared fewer than 9 hits with other tracks
- 13-hit tracks shared fewer than 8 hits with other tracks

All the hits used by those high quality tracks were removed from the pool of available hits in preparation for the second stage tracking.

The procedure for the second stage tracking with those leftover hits was identical with the first stage tracking except that less stringent criteria were applied in order to save wide angle, low momentum tracks which were outside the acceptance of the most downstream chambers. A track identified by the second stage tracking satisfied the following requirements:

- A minimum of 11 hits were required if the track was within the acceptance of PWC module 4.
- A minimum of 10 hits were required if the track was within the acceptance of PWC module 3.

After second stage tracking, high quality tracks satisfied the following requirements:

- The Y view impact parameter projected to the center of the target was less than 2.5 cm.
- 16-hit tracks shared fewer than 14 hits with other tracks
- 15-hit tracks shared fewer than 13 hits with other tracks
- 14-hit tracks shared fewer than 11 hits with other tracks
- 13-hit tracks shared fewer than 10 hits with other tracks
- 12-hit tracks shared fewer than 8 hits with other tracks
- 11-hit tracks shared fewer than 8 hits with other tracks
- 10-hit tracks shared fewer than 8 hits with other tracks

Once again, hits used by these high quality tracks were removed from the available pool prior to the final stage of PWC track finding. The only tracks left to be reconstructed in the third stage were outside the acceptance of PWC 3 and PWC 4. The third stage tracking was also done with exactly the same procedure as the previous stages except that the minimum required number of hits was 6.

STRAW Tracking

After the downstream space tracks were reconstructed using the PWC hits, those tracks were projected to the STRAW chambers. The downstream tracks were refitted using original PWC hits and the STRAW hits associated with the projection of those tracks.

4.1.2 Upstream Tracking and Linking

As mentioned in Chapter 2, the vertex SSD's consisted of 2 views (X,Y) with 5 planes per view. The upstream view tracking is similar to the PWC view tracking.

In fact, the track finding algorithm for the SSD's before the upgrade for 1990 and 1991 runs was very much the same as downstream PWC view tracking. However, the upgraded SSD vertex chambers with 5 planes per view required a much more complex algorithm to maximize the performance of the pattern recognition for selecting high quality tracks. To achieve this goal, the upstream tracking was designed to find tracks in a specific order and the linking with downstream tracks was used as an additional criterion in identifying high quality SSD tracks.

The SSD tracking was divided into two different stages based on the minimum number of hits required. In the first stage, following the same procedure as for PWC view tracking, in each view (X or Y) all possible 5 and 4 hit candidate tracks were selected with a χ^2_{dof} cut of 5.0 for 5 hit tracks and 4.0 for 4 hit tracks. The same procedure was done twice using two alternate sets of trial seed planes. In this initial set of candidate tracks, there existed a large number of candidate tracks sharing many common hits with one another.

These tracks were subjected to linking with already found downstream tracks at the center of the analysis magnet. Before the linking, however, a rough cleaning of candidate tracks was done to eliminate duplicate tracks. At this stage, we had to make sure that good quality tracks were not removed before linking. The track cleaning was carefully performed in three iterations based on the number of hits shared with other tracks and the number of tracks which shared those hits. When comparing two tracks sharing a certain number of hits, 5 hit tracks were alway preferred to 4 hit tracks and if the number of hits on tracks was the same, then the high χ^2_{dof} track was eliminated. The details of this complex step can be found in [44].

The surviving 5 and 4-hit candidate tracks and already found downstream tracks were projected to the center of the magnet and went through the linking procedure. The linking procedure was described in detail in [45]. The following is a brief

summary.

Linking

While all of the SSD tracks were projected to the center of the magnet, only those downstream space tracks with a Y view projection inside the SSD chamber acceptance participated in the linking procedure.

For each eligible downstream space track, the linking window size was determined by estimating the momentum of that track, assuming that it originated from the target. Inside this window, the projection differences, ΔX, ΔY and ΔY_{sl} between a SSD track and the downstream space track at the middle of the magnet were estimated.

At most 5 SSD tracks were selected as linked to a given downstream space track and after ordering them based on their linking χ^2 defined as:

$$\chi^2_x = (\frac{\Delta X}{\sigma_{\Delta X}})^2 \tag{4.1}$$

$$\chi^2_y = (\frac{\Delta Y}{\sigma_{\Delta Y}})^2 + (\frac{\Delta Y_{sl}}{\sigma_{\Delta Y_{sl}}})^2. \tag{4.2}$$

$\sigma_{\Delta X}$, $\sigma_{\Delta Y}$ and $\sigma_{\Delta Y_{sl}}$ were determined from the "momentum dependent linking window" [45].

In each linking window, a SSD track with the smallest total χ^2 was selected as the *best link* and other tracks (maximum 4) were called "extra links", if any. After the linking, the hits used by all the linked SSD tracks were removed from the pool of available SSD hits (including neighboring clusters of hits) in preparation for the second stage SSD tracking. The second stage tracking was performed in the same manner, but required a minimum of 3 hits on SSD tracks and in order not to lose any tracks, 4 sets of seed planes were used. The tracks from the second stage went through the same linking process, but only with unlinked downstream space tracks. Figure 4.1 illustracts the algorithm of upstream SSD tracking.

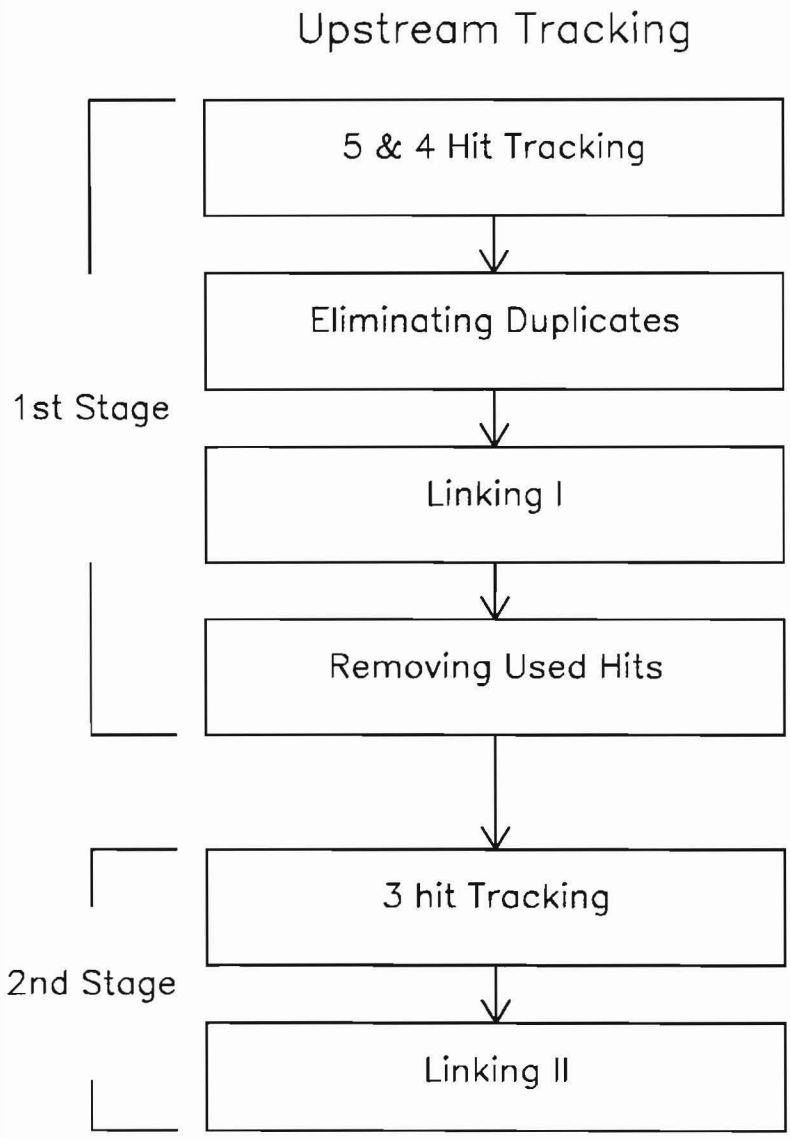

Figure 4.1: The algorithm of upstream SSD tracking.

4.1.3 Beam Tracking

The reconstruction of beam tracks was not much different from the other view tracking procedures. After choosing two alternate sets of trial seed planes, all the possible straight lines were made by connecting any two hits from each of those planes. For each straight line, if a hit was found in the third plane within a window size of 1.5 wire spacing, a χ^2 fit was made. The 3-hit beam tracks were accepted if χ^2_{dof} was less than 2. These 3-hit tracks were removed from the hit array and 2-hit tracks were made using the rest of the unused hits. The requirements on the beam tracks were:

- tracks with slope greater than ± 0.01 were rejected.
- projection to the target should be in target with 1.0 cm tolerance.
- projection to the beam hodoscope should be within 0.7 cm of the hodoscope's boundary.

4.1.4 Vertex Finding

The reconstruction of the primary vertex was performed in each view separately and then the two views matched to determine the three dimensional position of the vertex. In vertex finding, 3 or more SSD tracks were used. The requirements on the set of tracks used in vertex finding had the following hierarchy:

- linked 5 and 4-hit tracks
- linked 3-hit tracks
- unlinked 5 and 4-hit tracks

With a chosen set of tracks, the position of the view was determined by minimizing χ^2 defined as

$$\chi^2 = \Sigma \frac{b_i^2}{\sigma_i^2} \tag{4.3}$$

where b_i was the impact parameter of the i^{th} track and σ_i was the projection uncertainty of the i^{th} track. Once both view vertices were found, those vertices were refitted using the tracks associated with the vertex found in one view and the Z position of the vertex in the other view. The final Z postion of the matched vertex was determined by taking the weighted average of the Z positions of two refitted view vertices. If more than one vertex was found, the most upstream vertex was considered as the primary vertex.

4.1.5 Momentum Determination

As a final step in charged particle reconstruction, the momentum and the sign of the charge of the tracks were determined using the linking results and the reconstructed vertex position. The best linked SSD tracks were used when available to estimate the upstream direction associated with the given downstream track. If a downstream track did not have a linked SSD track in the X view, its X view upstream direction was estimated by assuming that the track originated from the primary vertex location. For those events in which no primary vertex was found, the center of the target volume was used as the vertex position.

The momenta and the sign of the charge were determined using the following equations:

$$Q = sign(\theta_1 - \theta_2) \cdot sign(B_0) \tag{4.4}$$

$$\sqrt{P_x^2 + P_z^2} = \frac{P_T^{kick}}{\sin\theta_1 - \sin\theta_2} \tag{4.5}$$

$$\frac{P_x}{P_z} = \tan\theta_x \tag{4.6}$$

$$\frac{P_y}{P_z} = \tan\theta_y \tag{4.7}$$

where θ_1 and θ_2 are the arc tangents of the upstream and downstream X-slopes. $\tan\theta_y$ is the slope of the upstream track in the Y view. The P_T^{kick} was calibrated using the K_s^0 and J/ψ signals measured in the tracking system. Figures 4.2 and 4.3 show these two mass spectrum, where the π's tend to have lower momenta, while the μ's generally have higher momenta. The magnitude of charge assigned to each charged track is assumed to be 1, since the observed long lived charged particles have unit charge.

4.2 Electromagnetic Shower Reconstruction

The program EMREC reconstructed the energy and the position of the showers detected in the EMLAC. The details of EMREC algorithm has been described in [38]. For the sake of completeness, a brief description of the EMREC algorithm will be presented.

First, the raw ADC count from EMLAC were digitized and converted to energy units and the background pedestal contributions were subtracted. Then the channel contents were corrected for the individual amplifier gains.

4.2.1 Groups, Peaks and Gammas

The showers in each quadrant were reconstructed independently. After summing the corresponding strip contribution from the front and back sections, EMREC searched for *groups* of adjacent strips in each view with energies greater than 80 MeV (95 MeV for the outer ϕ view). A group is defined as a cluster of at least 3 (2 in the outer ϕ view) consecutive strips with a total energy greater than 600 MeV and the energy in at least one of the strips greater than 300 MeV (350 MeV in outer

ϕ view).

Once the groups were found, then a search was made to find *peaks* which were defined as the strip where the position derivative of the energy distribution changes from positive to negative. If a peak was considered significant, another search was performed in the front section only. This was because low energy showers tend to deposit most of their energy in the front section and this search was to recover the peaks that might have been obscured when the front and the back energies were added to form the summed section. An additional search was made in the back section for surviving peaks in order to find corresponding peaks.

In the next stage, single-view showers (*gammas*) were reconstructed from groups based on the number of peaks involved. The gammas and the peaks were similar, but the energy and position of the gamma was determined from the expected shape of the shower. For single-peak groups, the energy and position of the gamma was determined by fitting it with a parametrized shower shape. For multiple-peak groups, the group was split into separated gammas and the energy and position of each gamma was calculated based upon the corrected pulse distribution [46] resulting from the global fit.

4.2.2 Correlation

The next step was to correlate the reconstructed gammas from different views (r and ϕ) to form the *photons*. As mentioned in Chapter 2, in the EMLAC, r view boards and ϕ view boards were alternated. As a result, the showers in r and ϕ views had approximately the same longitudinal energy deposition. So, the total energy and the ratio of the front and back section energies were very close in two views. In addition, the shower development in each view was also used for matching the two gammas to form a photon. These were the primary matching criteria in correlating gammas.

The simplest case was when one r view gamma was correlated with one ϕ view gamma (named 1 - 1 correlation) to form a photon. A more complicated situation arose when two or more photons overlapped in either view, or gammas happened to fall near the boundaries resulting higher order correlations. After all the gammas were correlated, the ϕ view gammas were reevaluated taking into account the position of the correlated r view gammas. The correlation procedure was repeated using the new ϕ view gamma energy values, and the final photon energy and position were determined. The final energy of a photon was determined by the energy sum of the r view gamma and the ϕ view gamma. The positions of the gammas in r and ϕ view formed the two dimensional position of the final photon.

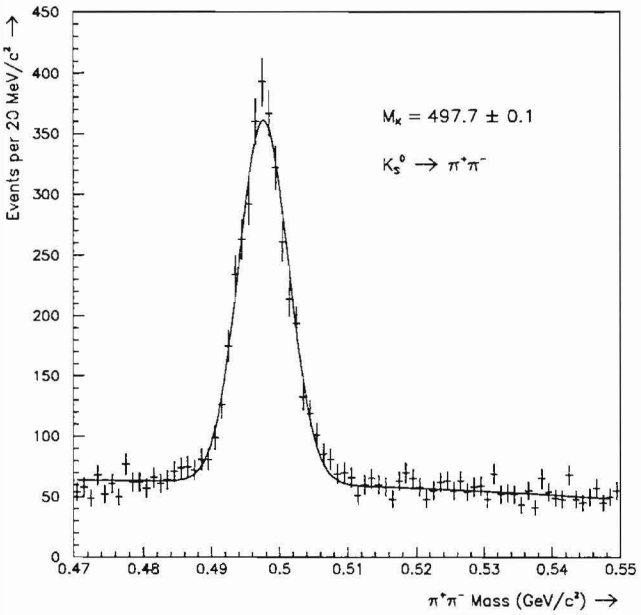

Figure 4.2: $\pi^+\pi^-$ mass spectrum

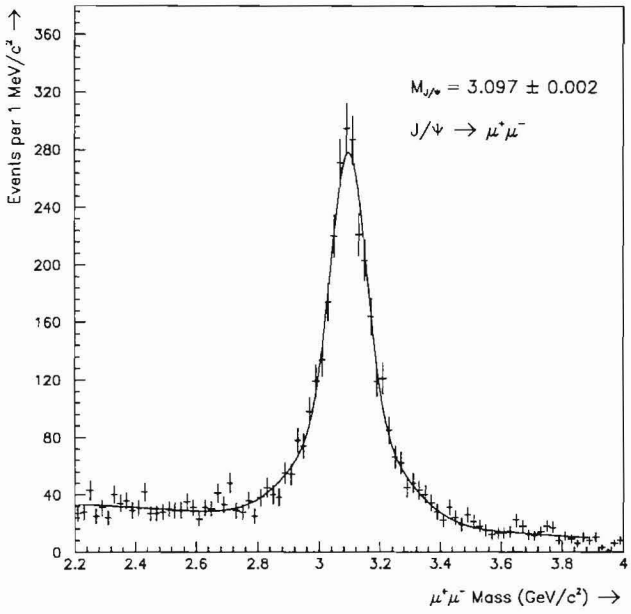

Figure 4.3: $\mu^+\mu^-$ mass spectrum

CHAPTER 5

Monte Carlo Simulation

5.1 Overview

In the course of the data analysis, Monte Carlo (MC) simulation plays an important role for several reasons. First of all, it provides theoretical predictions from a model based on perturbative QCD and the subsequent non-perturbative hadronization. The Monte Carlo method is also used to simulate complicated geometrical factors representing detectors. With the data generated and simulated by the Monte Carlo method, one can not only compare the data directly with the predictions but also determine the reconstruction efficiency and the geometrical acceptance correction.

In studies of direct photon production, it is essential to estimate the background contribution from the electromagnetic decays of hadrons because its cross section is relatively small. The primary source of this background arises from the finite size of the EMLAC, inefficient reconstruction of low energy photons from highly asymmetric π^0 and η decays and coalescence of nearby photons from symmetric decays of very high energy π^0's. The level of contribution to the backgrounds is determined by Monte Carlo methods. The Monte Carlo simulation is largely divided

into two parts, the event generation and the detector simulation.

5.2 Event Generation

Among several Monte Carlo implementations which simulate high p_T hadron-hadron scattering, two event generators, PYTHIA [47] and HERWIG [24] were examined. Their basic ingredients were similar, although they differed in detail with respect to both the perturbative and non-perturbative parts [48] of the programs. The most visible difference in the event structure may be attributed to the difference in their hadronization schemes. PYTHIA uses string fragmentation, while HERWIG employs a cluster model for the fragmentation scheme. Based on our studies of the multiplicities of charged tracks and showers in the electromagnetic calorimeter, HERWIG was chosen to generate events before the detector simulation.

For the jet studies, the QCD $2 \rightarrow 2$ hard parton scattering process and the direct photon + jet production process were selected in HERWIG to generate π^0+jet and γ+jet events. The π^0+jet events were selected from the di-jet events by requiring that at least one π^0 exists with a p_T above a given threshold. In order to simulate experimental conditions, two different incident beam types (530 GeV/c π^- beams and 800 GeV/c p beams) and two different target types (protons and neutrons) were used.

An event generated in HERWIG contains the information on final state hadrons as well as the history of those particles, including information on the partons, jets and all the decays of hadrons. A list of final state particles is input to a detector simulation program based on GEANT [25].

5.3 Detector Simulation

GEANT is a software program developed at CERN to simulate the passage of particles through matter. This program is designed to provide a data base of standard geometrical shapes and material properties which can be tailored to a specific experiment for complete specification of the experimental apparatus and the materials used in its construction. It also controls the development of each "physics" event and simulate the way each detector responds.

The detector simulation itself is divided into two stages. In the first stage, the events generated in HERWIG are processed through the customized GEANT program and provide outputs, assuming that all the detectors are fully efficient. The outputs from this stage contain a set of space points for each charged particle at the location of tracking chambers. For the LAC, the MC stored the amount of energy each strip collected from the ionization in the liquid argon in that event. All the generated final state hadrons in an event are considered to be from the primary vertex. The long life time ($> 10^{-16}$ seconds) particles are not allowed to decay in HERWIG, and those decays are handled by GEANT. The position of the primary vertex is simulated according to the profile of the vertices reconstructed from the experimental data and the subsequent decays create secondary vertices.

The result from the first stage detector simulation is still far from what is observed from the data. In order to simulate the experimental data more realistically, this information is passed on to a program called the "preprocessor" [1] in the second stage. The preprocessor is designed to simulate the effects of the actual performance of the various detectors. The handling of these effects for electromagnetic showers are extensively explained in [49] and will not be discussed here.

[1]This program is a preprocessor to the standard reconstruction package MAGIC and a post-processor of the MC simulation package.

5.3.1 Tracking System

Most of the detector effects associated with the tracking system can be implemented at the stage of digitizing the space point hits. In order to simulate the response of SSD and PWC chambers, those hits at each detector plane should be digitized so that each hit is assigned to the center of the nearest active strip position. This is the ideal situation which represents the perfect detectors.

Plane Efficiency

The first effect installed during the digitization was the "plane efficiency". From the data, a set of high quality tracks were selected in each subsystem. For example, 4 and 5-hit best-linked tracks were chosen in the SSD and the linked tracks of more than 13 hits were used in the PWC. Using the projection of these tracks to each plane, one could estimate the "hit occupancy" across the plane. Even though this does not represent the "true" plane efficiencies, the qualitative pattern should be approximately the same. Later, an appropriate scale factor for each subsystem was introduced by putting these MC results through the same software used to estimate the efficiencies for the data.

Slope Effects

When digitizing hits, a clearly visible difference between the data and the MC was the fact that there were a lot more multiple hits in the data. Multiple hits in the SSD and PWC planes were considered to be caused by several different effects. First of all, double hits were usually created by the "slope effect". For example, in the SSD, according to a previous study [27], it was known that when a charged particle passed straight through the plane spanning $\sim 300\ \mu m$ (thickness of a plane), approximately 24000 electrons were ionized. Fig. 5.1 illustrates how the effect was implemented. In each cell, the number of depleted electrons was determined as

$$N(e)_i = 24000 \times \frac{d_i}{300\mu m} + \sigma(e)_i \geq N(e)_{cut} \tag{5.1}$$

where d_i was the distance the charged particle crossed inside the cell i, $\sigma(e)_i$ was the uncertainty of determining $N(e)_i$ and $N(e)_{cut}$ was the minimum number of electrons required to produce a signal. $\sigma(e)_i$ was selected from a random distribution weighted by a Gaussian function of σ= 1000 electrons. In order to create the signal over the threshold, the total number of the depleted electrons inside a given cell had to be larger than $N(e)_{cut}$. If a track possesses a larger slope, the chance of making double (sometimes even triple) hits increases. As a useful criterion to tune this effect in the MC, the profile of double hits across the plane was divided by the single hit profile, bin by bin. In Fig. 5.2, the value in each bin represents the ratio of double hits to single hits in a specific region of the plane and the ratio increases toward both edges of the plane. Tuning the threshold parameter $N(e)_{cut}$ to be 8000 electrons, we were able to match the slopes of both wings in Fig. 5.2 with those in the data.

The same effect was also simulated in the PWC, but in a much simpler way. Without any sophisticated models as with the SSD, the only consideration was the distance of the track path and a threshold. In order to make a hit signal in the PWC cell, it was required that the distance a track crossed in a cell had to be at least 30 % of the the thickness of the plane. For the PWC, this method resulted in a sufficiently good match with the data.

Delta Ray Effects

The same ratios for triple and more hits did not show much of a slope effect and their distributions were almost flat across the plane. The larger size multiple hits are considered to come predominantly from the "delta ray effect" which is caused by knock-on electrons whose paths are at large angles to the path of the incident charged particle. This effect is assumed to be almost independent of the slope of

incident particles. An attempt to install this effect through the existing routine in GEANT utilizing the Landau distribution was not satisfactory. So, we decided to implement this effect phenomenologically. From the data, the ratios of the total number of multiple (double, triple, quadruple, and so on) hits to the total number of single hits were estimated, respectively. The reason for including double hits in the delta ray effect was to simulate the flat part in Fig. 5.2. In the MC, single hits were converted into multiple hits according to these ratios and this conversion was done randomly so that the profile of each multiple hits should follow that of single hits. This process went through several interations.

Random Noise

So far, the detector effects explained were related to the passage of charged particles through the detector volume and our observation of how each detector component responded. However, there also existed a considerable number of hits which did not seem to be correlated with the tracks. They were called "random noise hits" which were primarily caused by noise from the readout electronics. Naturally, they can be assumed to be randomly scattered all over the plane. We selected the events in which no interaction occurred and required that there existed only one beam track. After removing the hits from the beam track, the profile of multiple hits was made. This pattern was simulated utilizing the same method developed for the delta ray effects, but the ratios were obtained from the data events with only one beam track and no interactions.

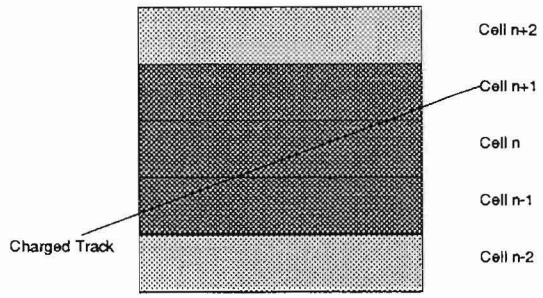

Figure 5.1: Slope effects in digitization of hits.

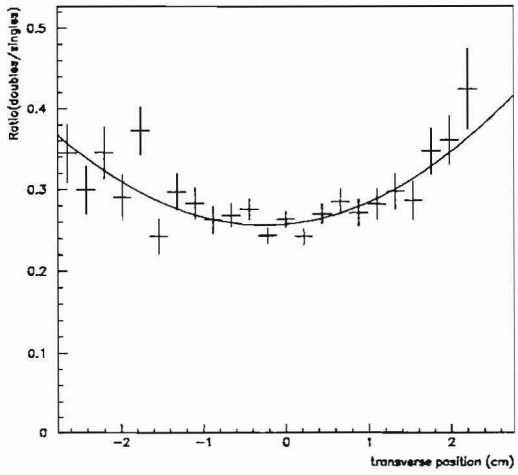

Figure 5.2: The ratio of profile of double hits to that of single hits. The rising trend toward the edges of the plane was attributed to the slope effects when digitizing hits and the flat part was considered to be from the delta ray effects.

CHAPTER 6

Data Analysis

6.1 Event Selection

The data used for this analysis were collected during the 1990 and 1991 fixed target runs. A summary of events recorded during these periods is listed in Table 6.1. For a study of jets, we selected the events containing high p_T π^0 or direct photons, which serve as the trigger particle when jet finding is applied.

Cuts were applied to the data sample to insure that the interaction which generated the trigger particle occured in the target region of the spectrometer.

6.1.1 Vertex Cuts

The reconstructed primary vertex in the event was required to be located inside a target fiducial volume. The distribution of the reconstructed z position of the primary vertex for events containing high p_T π^0's is presented in Figure 6.1. The edges of each target piece are clearly visible and some of the beam and vertex SSDs are also shown. The x and y positions of vertices are shown in Figure 6.2. In these plots the target areas are also shown along with the area (square) covered by the beam hodoscope which was used to define incident beam particles. From these

Run	Interaction	Beam Momentum (GeV/c)	Number of Events	Sensitivity (events/pb)
1990	π^-Be	515	30×10^6	8.6
	π^-Cu			1.4
1991	pBe	800	23×10^6	7.3
	pCu			1.8
	pH			1.5
	(p,π^+)Be	530	14×10^6	6.4
	(p,π^+)Cu			1.6
	(p,π^+)H			1.3
	π^-Be	530	4×10^6	1.4
	π^-Cu			0.3
	π^-H			0.3

Table 6.1: The E706 runs summary.

projections, it is apparent that the beam was well centered on the beam hodoscope but not on the targets during the 1990 run.

6.1.2 Muon Rejection

A possible major source of background to the events with high p_T showers is muon triggered events. Muons in the beam halo traveled nearly parallel to the beam line, but were frequently displaced several feet away from it. A fraction of these muons interacted in the calorimeter and produced photons via the bremsstrahlung process, thereby mimicking high p_T showers in the EMLAC. As already mentioned, during data acquisition, the information from the three veto walls was used to reject many of the events generated by the muons. The trigger logic rejected events whenever the upstream veto walls recorded a signal in coincidence with the logical OR of the signals from two downstream veto walls for the quadrant shadowing the triggering octant within $\pm$ 75 ns of the interaction time. However, due to inefficiencies in the veto walls, gaps between the scintillation counters in the veto wall geometry, and the limited duration of the on-line veto wall window, some muons escaped on-line detection.

An off-line veto wall signal was used to identify muon triggered events. For each quadrant of the EMLAC, a logical expression VW = (VW1 + VW2)*VW3 was evaluated. The logicals VW1, VW2 and VW3 were TRUE if there was a signal from the corresponding veto wall within a $\pm$ 20 ns time window. The logical OR of VW's was formed in a 300 ns wide window centered around the interaction. If the result was TRUE for the quadrant which contained the highest p_T object in that event, the event was rejected. Although this off-line veto condition eliminated a substantial fraction of events triggered by muons, it did not entirely eliminate them. To reject the remaining muon triggered events, two more muon cuts were applied :

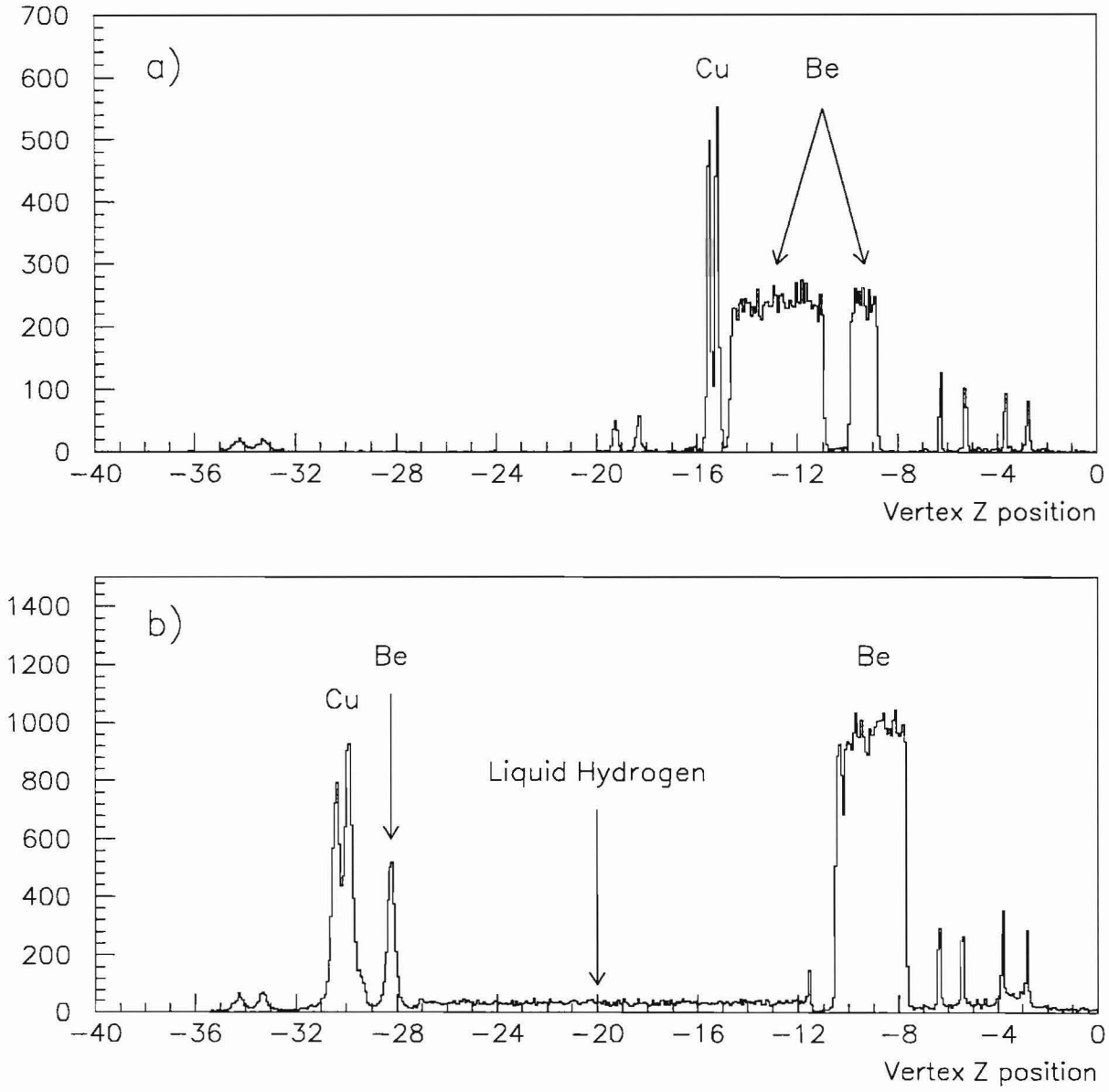

Figure 6.1: The distribution of the reconstructed z position of the primary vertex containing π^0 events whose p_T is greater than 5.5 GeV/c; a) 1990 run; b) 1991 run.

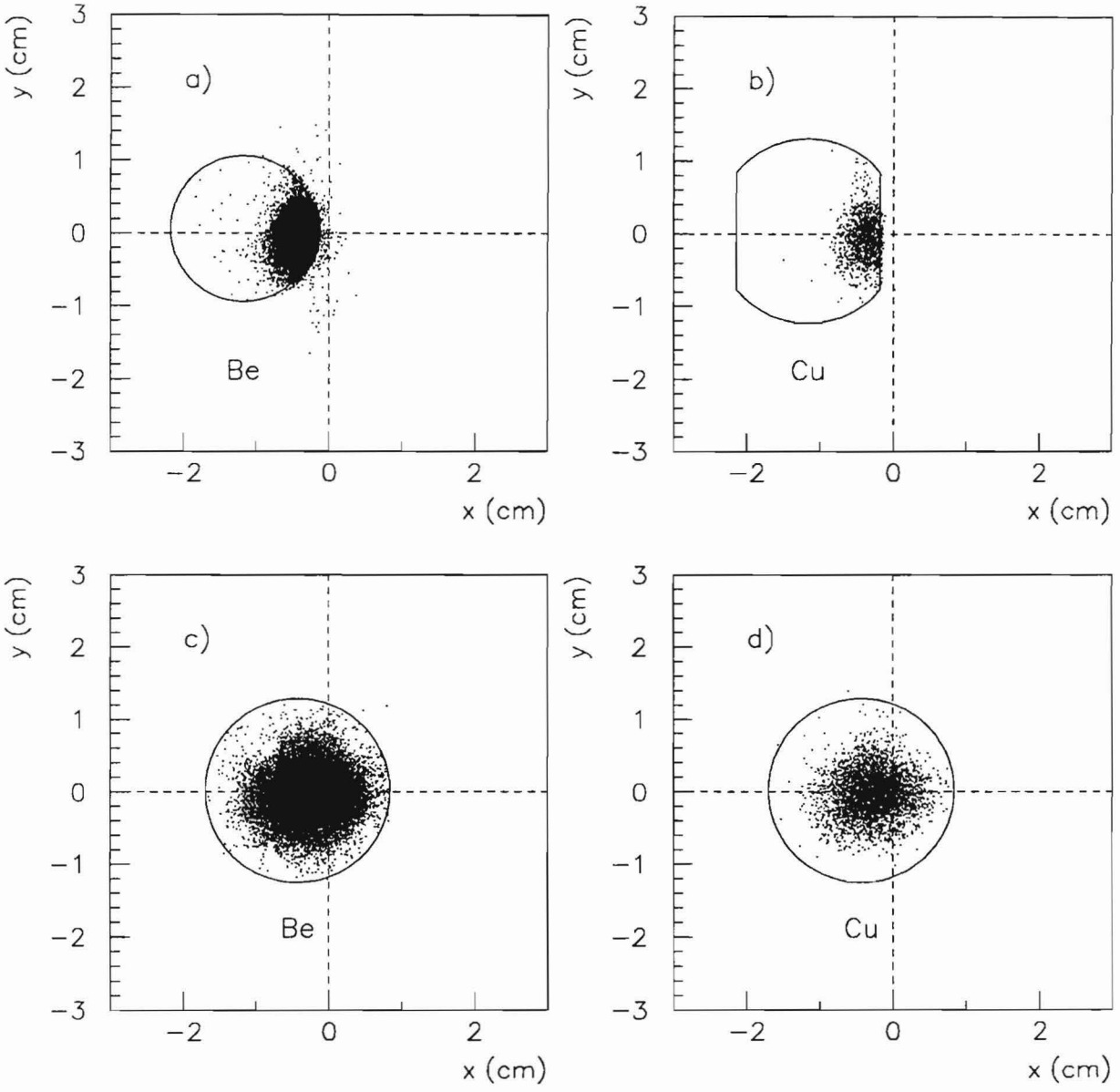

Figure 6.2: The distribution of the reconstructed x–y position of the primary vertex containing π^0 events whose p_T is greater than 5.5 GeV/c. Plots a) and b) are for the 1990 run and c) and d) for the 1991 run.

- directionality (Dir)
- scaled χ^2 in r view

The parameter Dir, called directionality, associated with a shower is defined as:

$$Dir = R_f - \frac{Z_f^{LAC}}{Z_b^{LAC}} R_b \tag{6.1}$$

where R_f, R_b, Z_f^{LAC} and Z_b^{LAC} were radial positions of the shower and z coordinates of the first EMLAC cell in the front and in the back sections. For showers originating from the target area, the directionality value would be in the vicinity of zero, but for muons travelling nearly parallel to the beam its value would be large and positive. The directionality of showers detected in the inner part of the EMLAC was not clearly determined, while the directionality of muons became larger as their radial position increased. The cut on directionality reflected this dependency on the radial position R, and was defined as

$$\begin{aligned} Dircut &= 0.2, \text{ if } R \leq 40 \text{ cm} \\ &= 0.0048 \times R, \text{ if } R \geq 40 \text{ cm}. \end{aligned} \tag{6.2}$$

The directionality cut was applied to the highest p_T shower in an event.

Another variable designed to cut muon-like showers was defined as the ratio of the photon r view χ^2 to its energy. The event was rejected if the value of the scaled r view χ^2 [50] of the highest p_T shower was greater than 0.1.

6.2 Trigger Particle Definition

Once we have a clean sample of high p_T showers originating from the target region, most of the events are considered to include π^0's, η's and direct photons. However, in order to identify well defined π^0's and direct photons as trigger particles, additional cuts are applied.

6.2.1 EMLAC Fiducial Volume

The energy and position of showers near the edges of the calorimeter are less accurately determined since part of the showers occur in uninstrumented regions. To exclude such poorly reconstructed photons from further analysis, a fiducial cut was made on the photon positions. The condition was that the photon position should be at least 2 r strip widths away from the following boundaries:

- inner edge of the octant (cut on the rapidity[1] in the forward region)
- outer edge of the 235th r strip, the last full EMLAC r strip (cut on the rapidity in the backward region)
- octant and quadrant ϕ boundary (cut on the azimuthal coverage)

The π^0 position was defined as the energy weighted average of photon positions.

6.2.2 Hadron Rejection

In addition to the showers from photons, there are also showers from charged and neutral hadrons. The fact that electromagnetic and hadronic showers have a different longitudinal profile development was used to discriminate between hadronic and electromagnetic showers. A typical electromagnetic shower tends to deposit most of its energy in the first few radiation lengths of the detector, while a typical hadron deposits more of its energy in the back section of the EMLAC due to its small interaction length. Thus, many hadronic showers can be eliminated by using the ratio E_f/E_t, which is the ratio of the energy deposited in the front section of EMLAC to the total energy deposited in the EMLAC. The peak at low values of E_f/E_t is attributed primarily to hadronic showers, whereas electromagnetic showers tend to

[1] We do not distinguish between the rapidity (y) defined by $\tanh y = p_z/E$ and the pseudorapidity (η) defined by $\tanh \eta = \cos\theta$; since m_{π^0} is negligible compared to E, $p_z = E\cos\theta$.

populate the high end of the E_f/E_t distribution. All showers with $E_f/E_t < 0.2$ were excluded from the analysis.

6.2.3 π^0 Definition

π^0 mesons were reconstructed via the effective mass of two photon pairs, each of which already satisfied the fiducial and E_f/E_t cuts. Also, both photons were required to be in the same octant. Figure 6.3 presents the invariant mass spectrum of $\gamma\gamma$ pairs with vector sum p_T greater than 5.5 GeV/c. The π^0 and η mass peaks are clearly visible at $\sim$ 135 MeV/c^2 and $\sim$ 550 MeV/c^2, respectively. The dashed line is the same distribution with energy asymmetry cut of 0.75.

The energy asymmetry A, is defined as

$$\begin{aligned} A &= \frac{\mid E_1 - E_2 \mid}{E_1 + E_2} \\ &= \beta \cos\theta^*, \end{aligned} \tag{6.3}$$

where E_1 and E_2 are the energies of two photons and θ^* is the decay angle with respect to the direction of the π^0. Since the π^0 meson is a spin zero particle, the two photon decay in the π^0 center of mass is isotropic. The distribution of the π^0's as a function of the cosine of the decay angle θ^* relative to the direction of flight of the parent pion should be flat. For π^0's travelling near the speed of light ($\beta \sim 1$), A is equal to $cos\theta^*$.

Highly asymmetric decays of π^0's produce photons with very low energy and at large angle relative to the π^0's in its rest frame. The limited acceptance of the EMLAC and the reconstruction inefficiency at low energies result in a substantial loss of π^0's with high asymmetry. The top two plots of Figure 6.4 shows the asymmetry distributions in the π^0 mass region and its sideband region, respectively. The entries in the bottom plot were calculated by extending the fit to the background under the π^0 mass peak ($0.1 < m_{2\gamma} < 0.18$) and subtracting it from the signal. The resulting

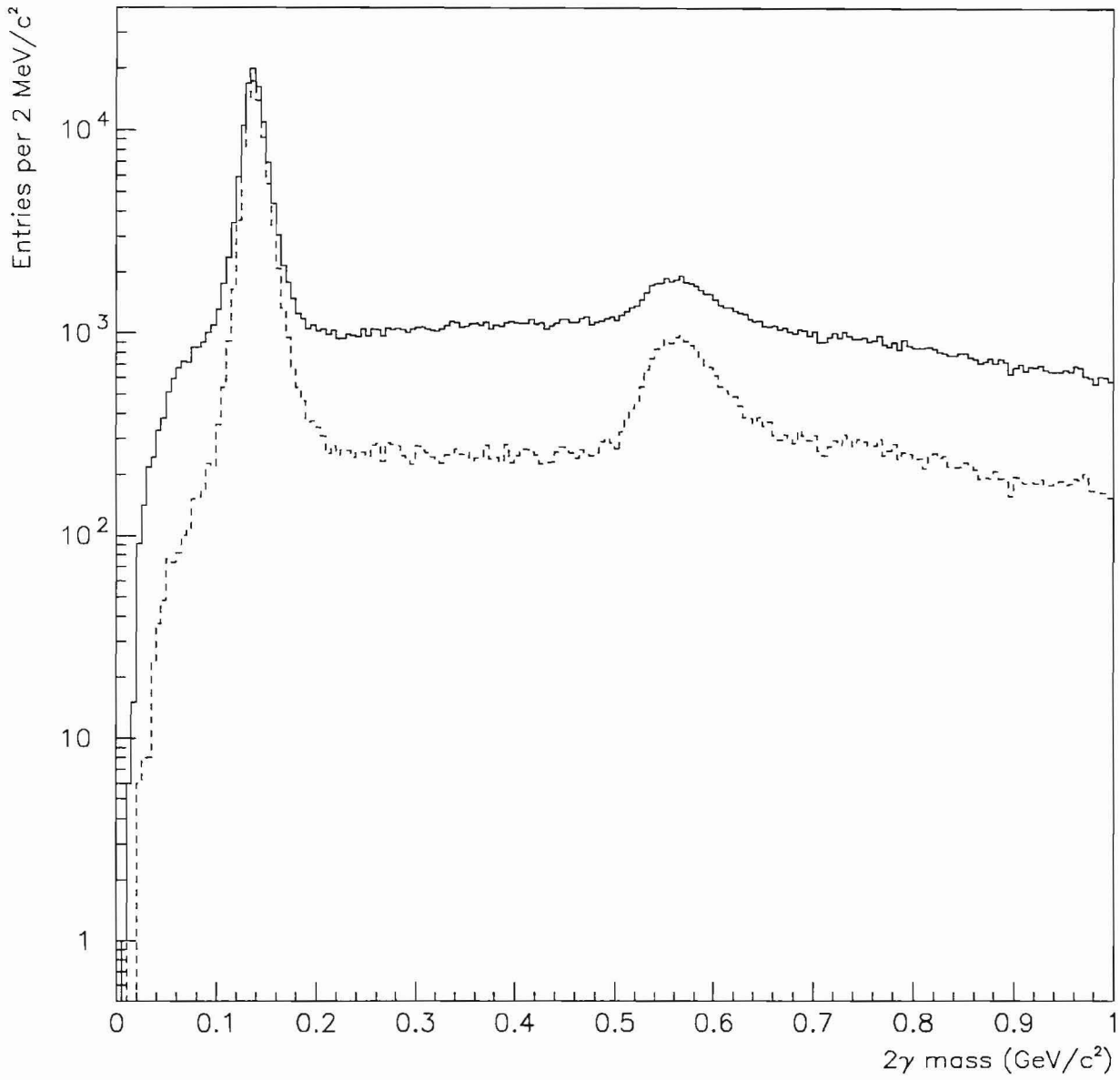

Figure 6.3: Two photon mass distribution with p_T above 5.5 GeV/c. The dashed line is after applying the asymmetry cut.

distribution is nearly flat up to an asymmetry of 0.7 and drops to zero around 0.95. The asymmetry cut value was set to 0.75 and the same value was used in the π^0 geometric acceptance and reconstruction efficiency calculations.

The following is the summary of requirements on the π^0 signal:

- All the event level cuts were satisfied
- p_T of $\pi^0 > 5.5$ GeV/c
- Mass range: $0.10 < m < 0.18$ MeV/c^2
- Asymmetry cut A < 0.75
- $E_f/E_t > 0.2$ for both photons
- Fiducial region cut for both photons

6.2.4 Direct Photon Definition

Any high p_T photon which did not combine with other photons to form a π^0 or η was accepted as a direct photon candidate. It satisfies the following cuts.

- All the event level cuts were satisfied
- p_T of Direct Photon > 5.5 GeV/c
- $E_f/E_t > 0.2$
- Photon is in the fiducial region of the EMLAC
- There are no charged tracks within 1.5 cm of the photon at the front face of the EMLAC

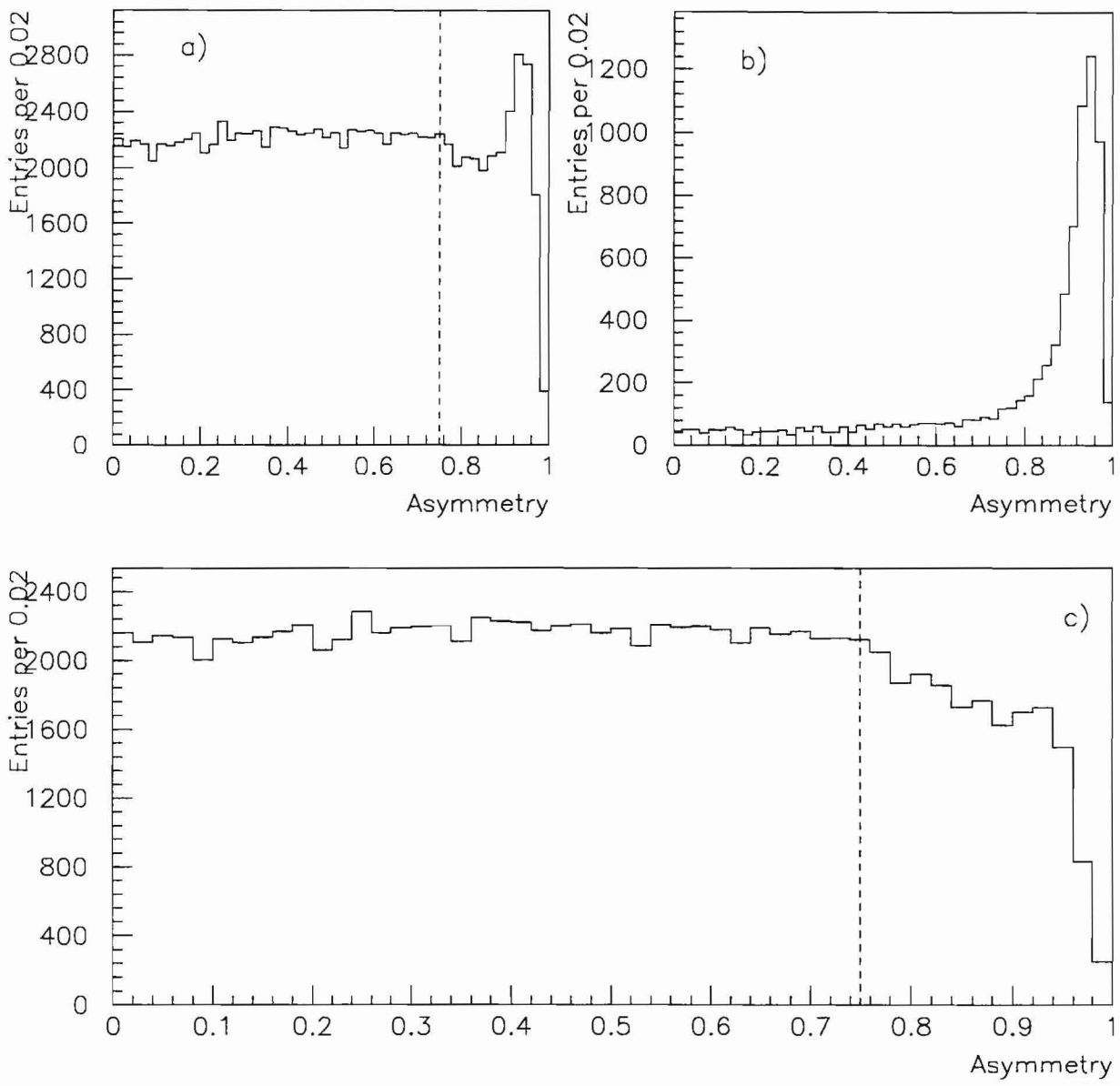

Figure 6.4: The asymmetry distribution of π^0's at $P_T \geq 5.5$ GeV/c; a) before the side band subtraction, b) only the side band c) after the side band subtraction, (Side bands: $0.08 < m < 0.10$ MeV/c^2 and $0.19 < m < 0.21$ MeV/c^2).

6.3 Jet Reconstruction

The jet reconstruction algorithm is based on a well known "cone" algorithm which has been adopted by many different experiments. This algorithm is widely used because it is easy to understand and the application is simple. Throughout the jet analysis, all the charged tracks are assumed to be pions and all the electromagnetic showers which are not linked to tracks are assumed to be photons.

6.3.1 Jet Algorithm

In reconstructing jets, we first define two seed directions in the hadron center of mass frame. One seed direction is given by the direction of the trigger particle, and for the other seed, we choose the highest p_T particle in the opposite (away-) side of the trigger particle. The away-side is defined as more than 100^0 away azimuthally from the trigger particle and the seed particle in the away-side is called the "leading particle". The algorithm makes use of only those reconstructed charged particles that satisfy the criteria described below.

- Each charged particle must have $p_T > 250$ MeV/c.
- Each charged particle must have pseudorapidity $|\eta| < 1.75$.
- Each charged particle must have y view impact parameter < 1.5 cm at the primary vertex.

The leading particle can be either a charged particle or a photon, but must have a p_T greater than 500 MeV/c. The leading particles have to satisfy the following additional requirements.

- The leading photon or charged particle must have pseudorapidity $|\eta| < 1.75$.
- A leading photon must have energy in the range, 5 GeV $\leq E \leq$ 250 GeV.

- The leading photons must not have matching charge particles within 1.5 cm at the face of EMLAC to avoid the double counting.

Once the initial seed directions of trigger and away-side are set, the cone algorithm assigns the selected charged particles to an appropriate jet based on the value of ΔR associated with them. The quantity ΔR for each charged particle in a given jet is defined as follows:

$$\Delta R = \sqrt{(\Delta\eta)^2 + (\Delta\phi)^2} \tag{6.4}$$

where $\Delta\eta$ and $\Delta\phi$ are the differences in pseudorapidity and azimuthal angle, respectively, between the direction of the given jet and the charged particle. For each charged particle, we calculate the values of ΔR for both trigger and recoil jets and assign the charged particle to one of the jets if $\Delta R < 1$ (inside the cone). Using these initial assignments, the momentum vectors of the trigger and recoil jets are calculated by summing the momenta of the charged particles assigned to each jet axis. These new estimates of the jet directions are used to make another iteration of the assignments of the charged particles to both jets. The directions of the jets are re-evaluated after this second iteration. This procedure is repeated up to a maximum of 10 iterations unless the new direction is the same as the previous one.

6.3.2 Trigger and Recoil Jet Definition

The reconstructed trigger and recoil jets have to satisfy the following additional criteria:

- The reconstructed p_T of the recoil jet must be greater than 20% of the p_T of the trigger particle.

- The azimuthal angle between the recoil jet axis and the trigger particle must be greater than 1.75 radians.

- The rapidity of the recoil jet is limited to $|\eta_{jet}| < 1.0$ to minimize the overlapping effect from the beam/target jet.

6.4 Fragmentation Function

The reconstruction of jets recoiling against high p_T π^0's or direct photons provides an opportunity to study how the recoiling partons evolve into the observable hadrons. Not much is known yet for the nature of the fragmentation of quarks and gluons, except that the fragmentation of gluon-initiated jets should be softer [2] than that of quark-initiated jets. As discussed in Chapter 1, jets associated with direct photons should be dominated by gluon(quark) jets when $\pi^-(p)$ beams are used.

Our primary goal of the analysis on the fragmentation is to compare the fragmentation of jets dominated by gluon or quark jets from the data and identify any difference between them. From our data, we present the fragmentation function of four different recoil jets, using two different trigger particle types (γ and π^0) and two different beam types (π^- and p).

The dominance of either a gluon or quark jet in each fragmentation function is examined qualitatively by employing recently developed phenomenological models in HERWIG. We also present the fragmentation functions from fully detector-simulated MC data which have gone through the same reconstruction and analysis package as the data.

[2] *softer* fragmentation means that there are more particles inside the jet, each sharing a smaller fraction of the longitudinal momentum.

6.4.1 Definition of Z and Rescaling

The fragmentation variable z represents the longitudinal fraction of the momentum of the jet carried by a given charged particle and is defined as

$$z = \frac{\vec{p}_{ch} \cdot \vec{p}_{jet}}{|\vec{p}_{jet}|^2} \tag{6.5}$$

where $\vec{p}_{ch}$ is the momentum vector for a charged particle and $\vec{p}_{jet}$ for the jet in the center of mass frame. The fragmentation function $D(z)$ of the recoil jet for charged particles with z defined above is given by

$$D(z) = \frac{1}{N_{jet}} \cdot \frac{dn_{ch}}{dz} \tag{6.6}$$

where N_{jet} is the total number of recoil jets and dn_{ch} is the number of charged particles in the interval dz.

Unlike conventional di-jet experiments, we initially selected the events based on the p_T of trigger particles without any consideration of the p_T of recoiling jets. The steeply falling p_T spectrum of trigger particles combined with the k_T [3] effect introduce a non-negligible trigger bias which results in a p_T imbalance between recoil jet and trigger jet. Figure 6.5 shows the amount of p_T imbalance suffered by the jet that lies opposite to the trigger particle. The magnitude of the recoil jet momentum can be scaled such that p_T(recoil jet) = p_T(trigger jet) to account for any losses in the recoil jet reconstruction. The process by which the recoil jet momentum is corrected is called the *rescaling* and the z value of each charged particle associated with the jet is corrected by the following equation:

$$z_{rescaled} = z \cdot \frac{p_T(recoil\ jet)}{p_T(trigger\ jet)} \tag{6.7}$$

In Figure 6.6, we plot four different fragmentation distributions of charged particles in the recoil jet, comparing π^0 and direct photon data for two different beam

[3] k_T is defined as the initial transverse momentum carried by colliding partons with respect to the incoming hadrons.

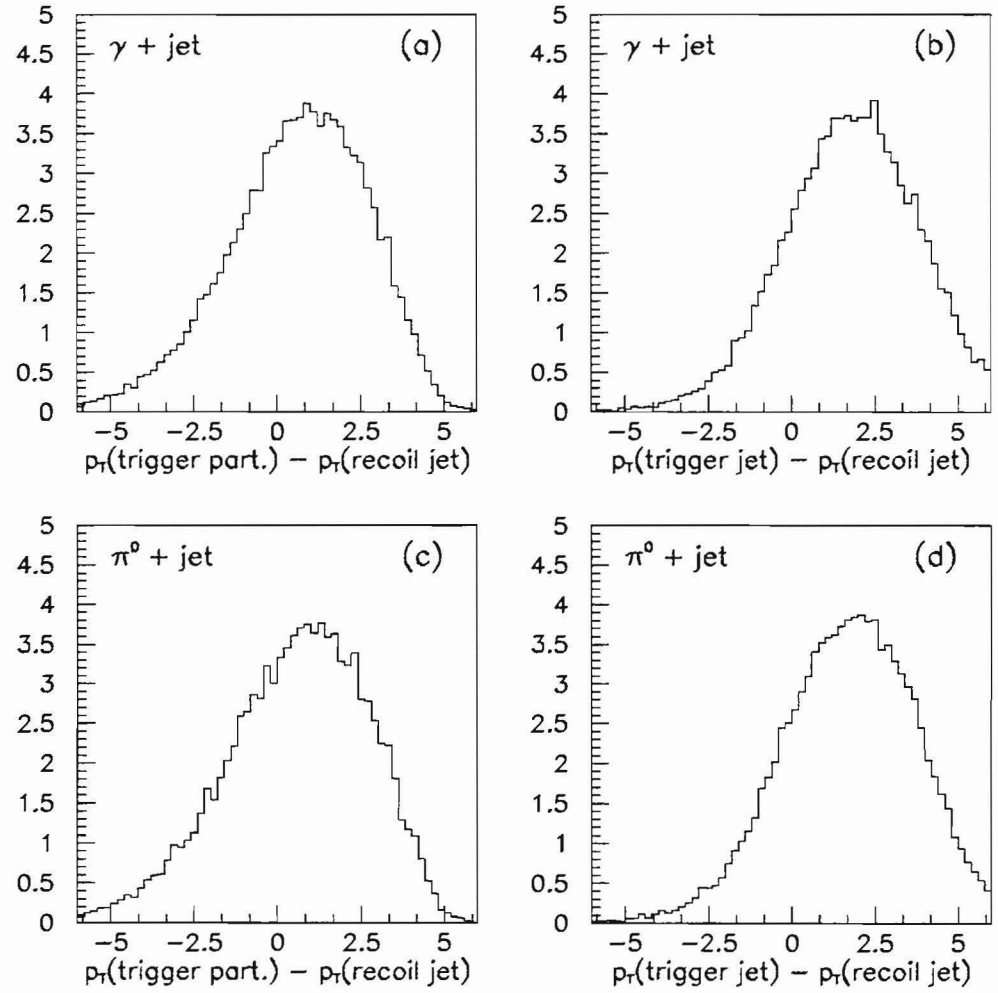

Figure 6.5: The p_T imbalance of recoil jet. a) and c) are the p_T difference between the trigger particle and the recoil jet of γ and π^0 respectively: b) and d) are the p_T difference between the trigger jet and the recoil jet of γ and π^0 respectively.

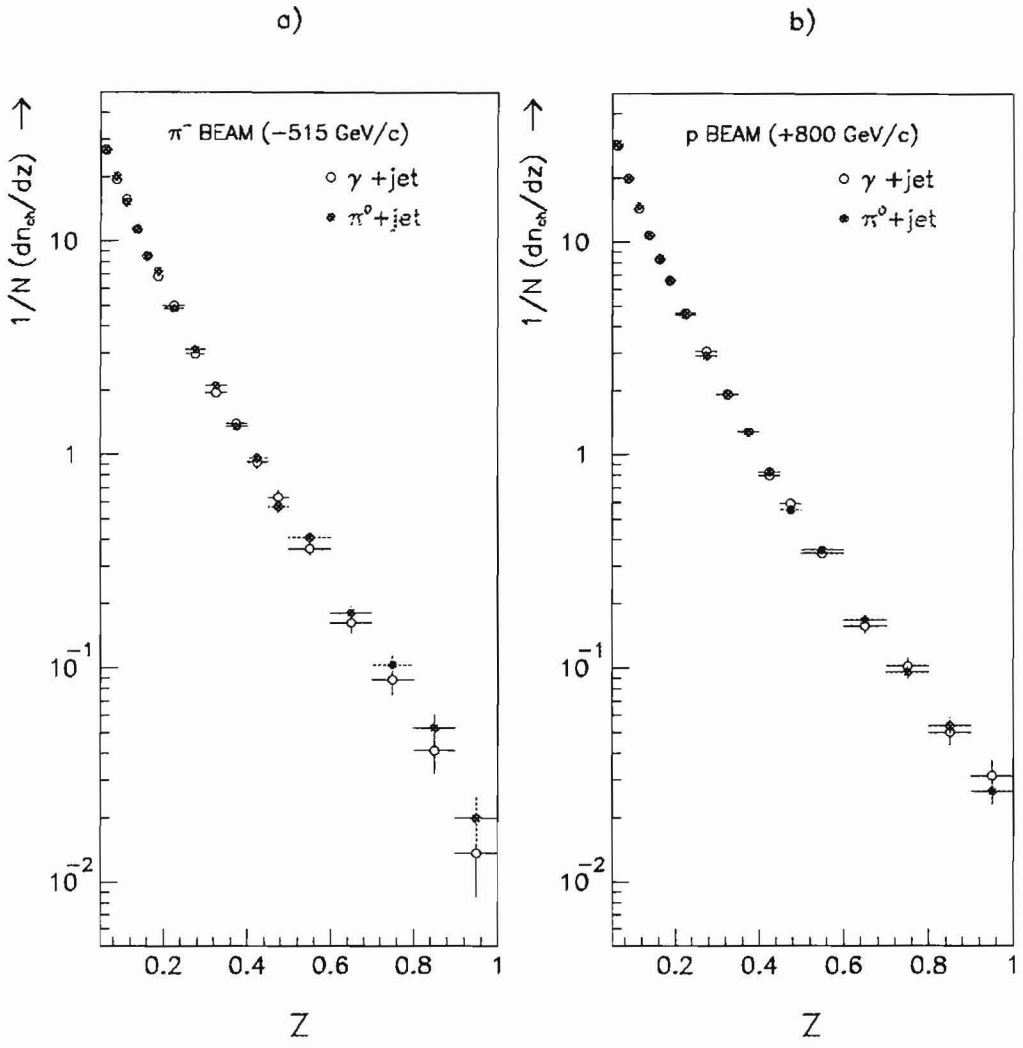

Figure 6.6: The fragmentation function $D(z)$ of four different samples with z rescaled to trigger jet. The plot a) compares the fragmentation function of γ+jet with that of π^0+jet for π^- beam. The plot b) compares the fragmentation function of γ+jet with that of π^0+jet for p beam. γ+jet events are not background subtracted.

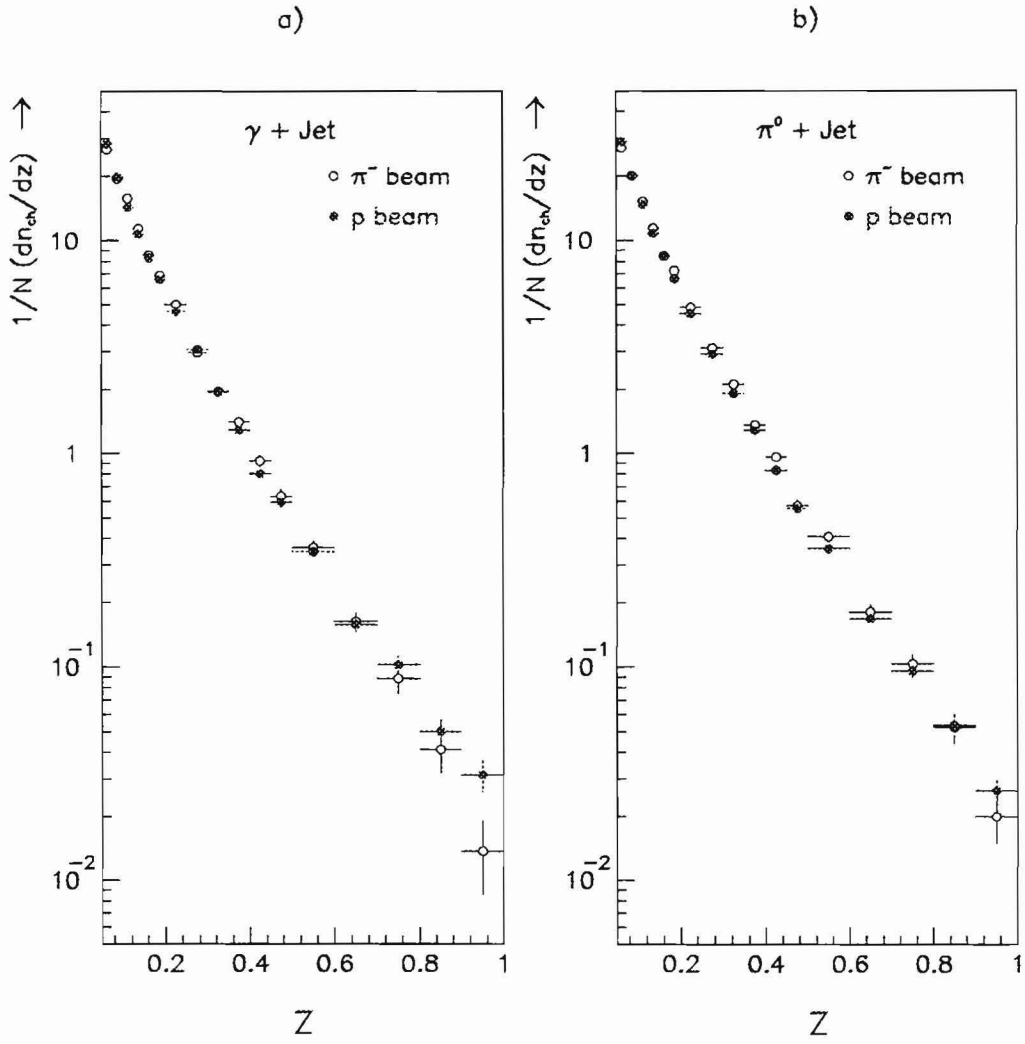

Figure 6.7: The fragmentation function $D(z)$ of four different samples with z rescaled to trigger jet. The plot a) compares the fragmentation function of γ+jet for π^- beam with that for p beam. The plot b) compares the fragmentation function of π^0+jet for π^- beam with that for p beam. γ+jet events are not background subtracted.

types (π^- and p). The data were chosen so that the trigger particle p_T was greater than 5.5 GeV/c and the rapidity range for both trigger and recoil jet was, $|\eta|$ <0.75. For the π^- beam data, we are tempted to argue that the fragmentation of the recoil jet from direct photon events looks softer [4] than that from π^0 events. Considering the fact that our direct photon candidates contain substantial background from π^0's, the subtraction of this background contribution might enhance the difference. The detailed procedure for the background subtraction will be discussed later in this section.

In Figure 6.7, we are comparing the fragmentation function from the same γ+jet and π^0+jet events produced with two different beam types. One can observe that the fragmentations of the recoil jets from π^0 events with either a π^- or p beam seem to show almost the same amount of hardness. However, the comparison between γ+jets indicates that the fragmentation of γ+jet with a p beam is slightly harder than that with a π^- beam in the high z region. From our expectation based on QCD, this was the plot we have anticipated to see the difference between gluon and quark jet fragmentations, but their difference is just barely visible.

So far, we have been looking at π^0+jet and unsubtracted γ+jet fragmentations with two different beam types. By how much should their fragmentations be different? There are questions of how much softness or hardness in fragmentation we should expect from the π^0+jet and γ+jet events with π^- and p beams. We are going to examine the fragmentation models in HERWIG and also see how they turn out to appear when simulated with our detector geometry.

[4] The slope of the *softer* fragmentation function is steeper than that of the *harder* fragmentation function.

6.4.2 Monte Carlo Predictions

First, we are going to examine Monte Carlo predictions without any detector simulation. As presented in Chapter 5, the HERWIG Monte Carlo program (v5.6) was adapted to generated π^0+jet and γ+jet events using two different beam types (π^- and p beams) and two target particle types (protons and neutrons). All the events were generated with a parton level p_T greater than 5.0 GeV/c, and later selected by requiring the p_T of the trigger particle (γ or π^0) greater than 5.5 GeV/c. These four types of generated MC jets provide a chance to examine the quark and gluon jet dominance and the original shape of the fragmentation function of those jets.

Unlike the simpler Monte Carlo event generator ISAJET, it has been known to be extremely difficult to determine which final state particle belongs to which jet in the HERWIG Monte Carlo. In order to address this situation, we apply the cone algorithm ($\Delta < 1$) to the generated final state particles and the known original jet directions. If a given particle lies inside the cone around a certain jet direction, then the particle is assigned to that particular jet.

In Figures 6.8 and 6.9, we plot the MC prediction of fragmentation functions of charged particles for the π^0+jet and γ+jet events with π^- and p beams. The corresponding percentage yield of q-jets and g-jets in the recoil jet is shown in Table 6.2. The results do not include any detector effects such as acceptance, reconstruction inefficiency and mis-reconstruction. They are presented without any rescaling of the fragmentation variable z.

The predictions on the difference of the fragmentation functions between π^0+jet and γ+jet for π^- beam and between γ+jet for π^- beam and γ+jet for p beam are much more dramatic than our data. These predictions are consistent with the expectation that q-jets should be harder than g-jets.

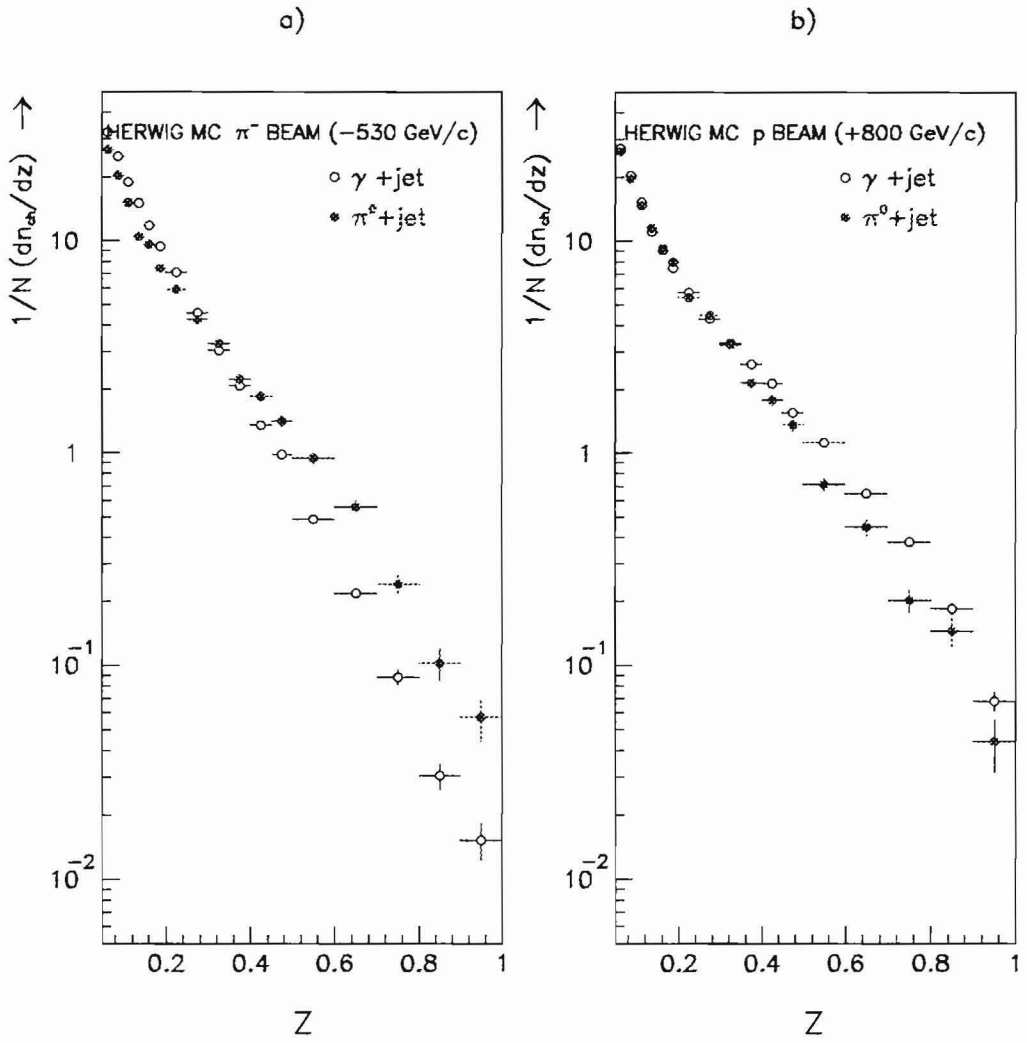

Figure 6.8: The prediction of fragmentation functions using a HERWIG Monte Carlo model without any detector simulation, comparing π^0+jet and γ+jet events with π^- and p beam types.

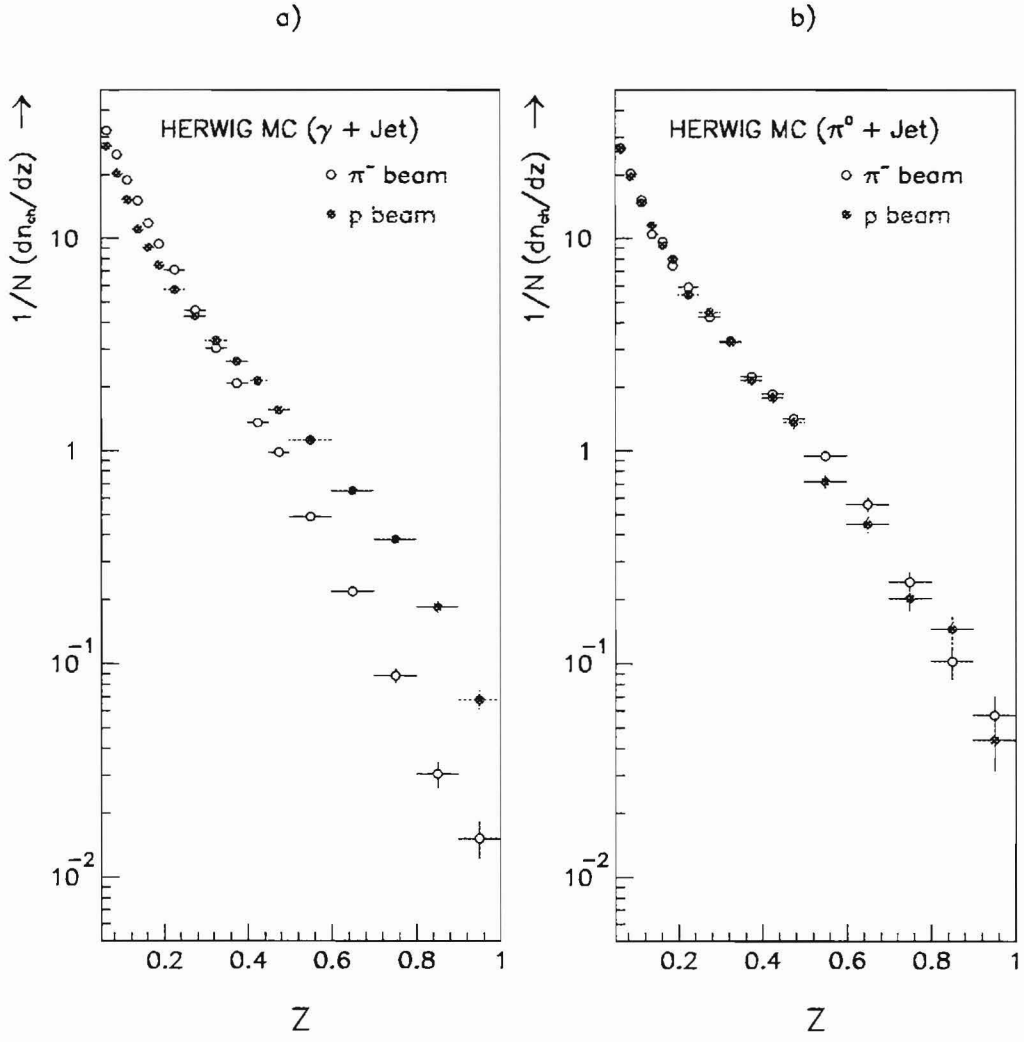

Figure 6.9: The prediction of fragmentation functions using a HERWIG Monte Carlo model without any detector simulation, comparing π^- and p beam types for π^0+jet and γ+jet events.

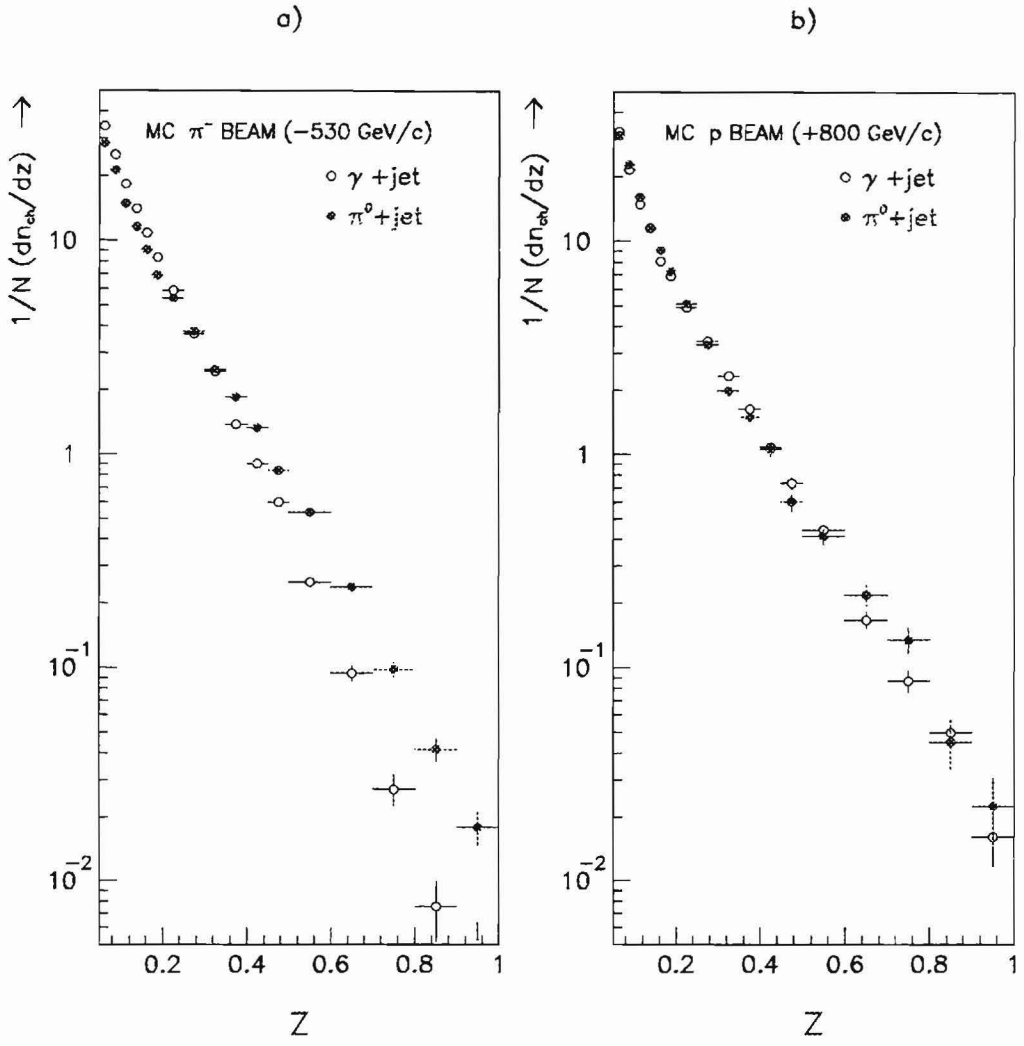

Figure 6.10: The Monte Carlo fragmentation $D(z)$, comparing γ+jet and π^0+jet in π^- (a) and p (b) beam types. The MC events are fully detector-simulated through GEANT and reconstructed by the same reconstruction package as used for the data. z is rescaled to the trigger jet

	Target	π^- beam		p beam	
		quark	gluon	quark	gluon
γ +jet	proton	17	83	91	9
	neutron	30	70	92	8
π^0+jet	proton	70	30	60	40
	neutron	79	21	68	32

Table 6.2: The prediction of the HERWIG Monte Carlo for the percentage yield of q-jets and g-jets in the recoil jet in π^0+jet and γ+jet events with p_T cut of 5.5 GeV.

Now, it is very interesting to investigate how these predicted fragmentation functions would appear when all the experimental effects are added. We processed the generated HERWIG MC data through the E706 Monte Carlo detector simulation package (Chapter 5) and reconstructed and analyzed them exactly the same way as we did our data. The resulting fragmentation functions are shown in Figure 6.10. Note that the differences in the fragmentation of quark and gluon dominated jets are much less than in the HERWIG unreconstructed prediction. Nevertheless, they are still distinguishable.

Even though it is known that the fragmentation scheme in HERWIG has been tuned to many recent collider experiments, not much evidence of agreement has been reported when compared with the data from fixed target experiments. However, it is an important part of this analysis to study how the original fragmentation would be observed with our experimental setup, with all the reconstruction techniques applied. In a sense, if the prediction from HERWIG (Figure 6.8 and 6.9) represents 'true' fragmentation, then the results from the detector simulated MC (Figure 6.10) should be what we can observe from the data.

6.4.3 Background Subtraction

The direct photon events we have been analyzing contain a significant fraction of background due to single photons arising from the mis-reconstructed π^0's and η's. The major reasons for the mis-reconstruction are:

- failure to reconstruct low energy photons from highly asymmetric decays of π^0's,
- geometrical losses due to the active fiducial regions and the finite acceptance of the EMLAC, and
- coalescence of nearby photons from symmetric decays of high energy π^0's.

What fraction of our direct photon candidates are *fake* direct photons which actually come from π^0's, but reconstructed as direct photons? What is their contribution to the fragmentation function? How do we account for this contribution from our γ+jet data?

In order to answer these questions, fully detector-simulated Monte Carlo π^0+jet events are utilized once again. All of the MC events were generated with high p_T π^0's in them, but some of them are reconstructed as direct photon events due to the reasons listed above. The level of background contamination in our γ+jet data can be estimated based on the ratio of the number of the fake γ+jet events, N_γ^{mc}, to that of the π^0+jet events, $N_{\pi^0}^{mc}$, reconstructed from the MC π^0+jet data.

Suppose we have N_γ^{exp} ($N_{\pi^0}^{exp}$), γ+jet (π^0+jet) events in the data. If we assume that our γ+jet data contain N_γ^{fake} γ+jet events, the total number of 'true' γ+jet events in the data, N_γ^{true} is determined by

$$\begin{aligned} N_\gamma^{true} &= N_\gamma^{exp} - N_\gamma^{fake} \\ &= N_\gamma^{exp} - N_{\pi^0}^{exp} \times \frac{N_\gamma^{mc}}{N_{\pi^0}^{mc}}. \end{aligned} \tag{6.8}$$

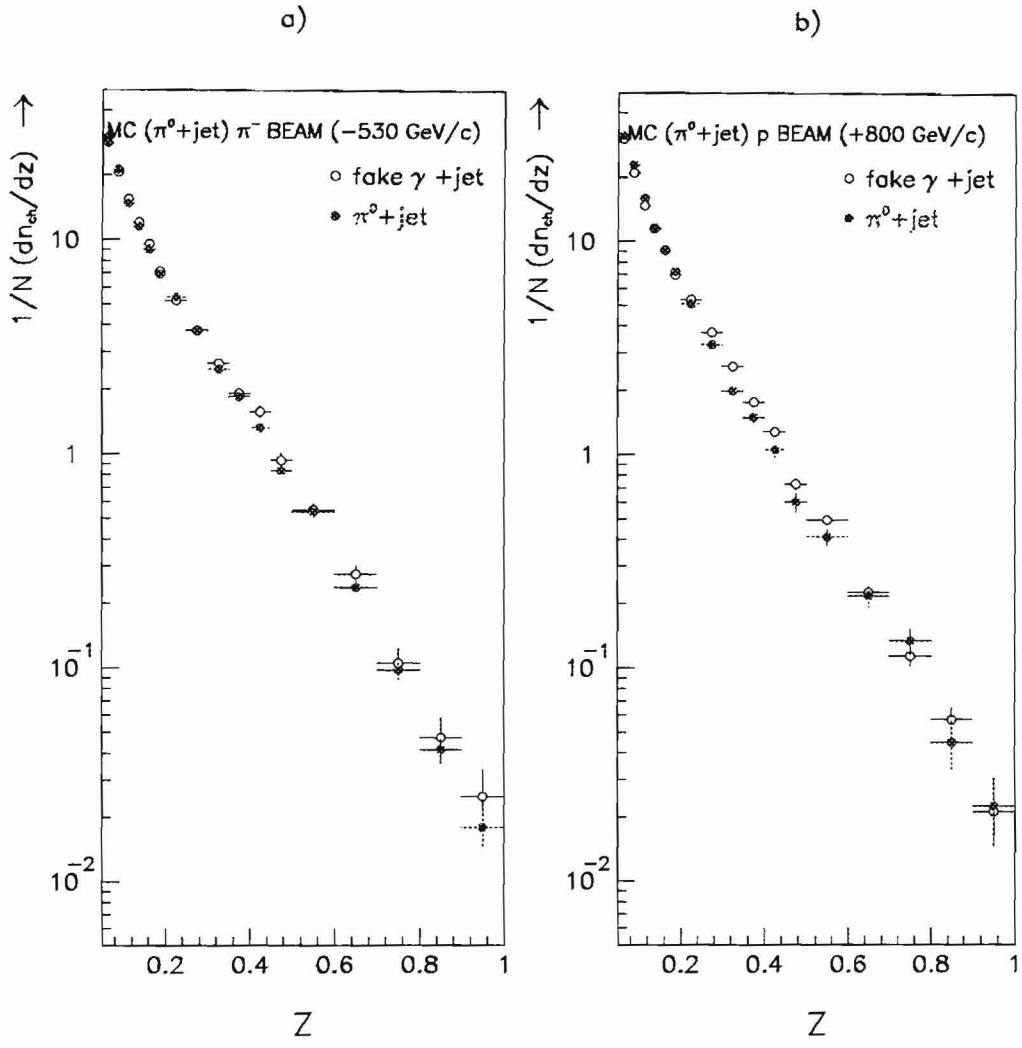

Figure 6.11: The Monte Carlo fragmentation $D(z)$, comparing π^0+jet and fake γ+jet in π^- (a) and p (b) beam types. The MC π^0+jet events were generated in order to estimate the background level in the γ+jet data. Fully detector-simulated through GEANT and reconstructed by the same reconstruction package as for the data. z is also rescaled to trigger jet.

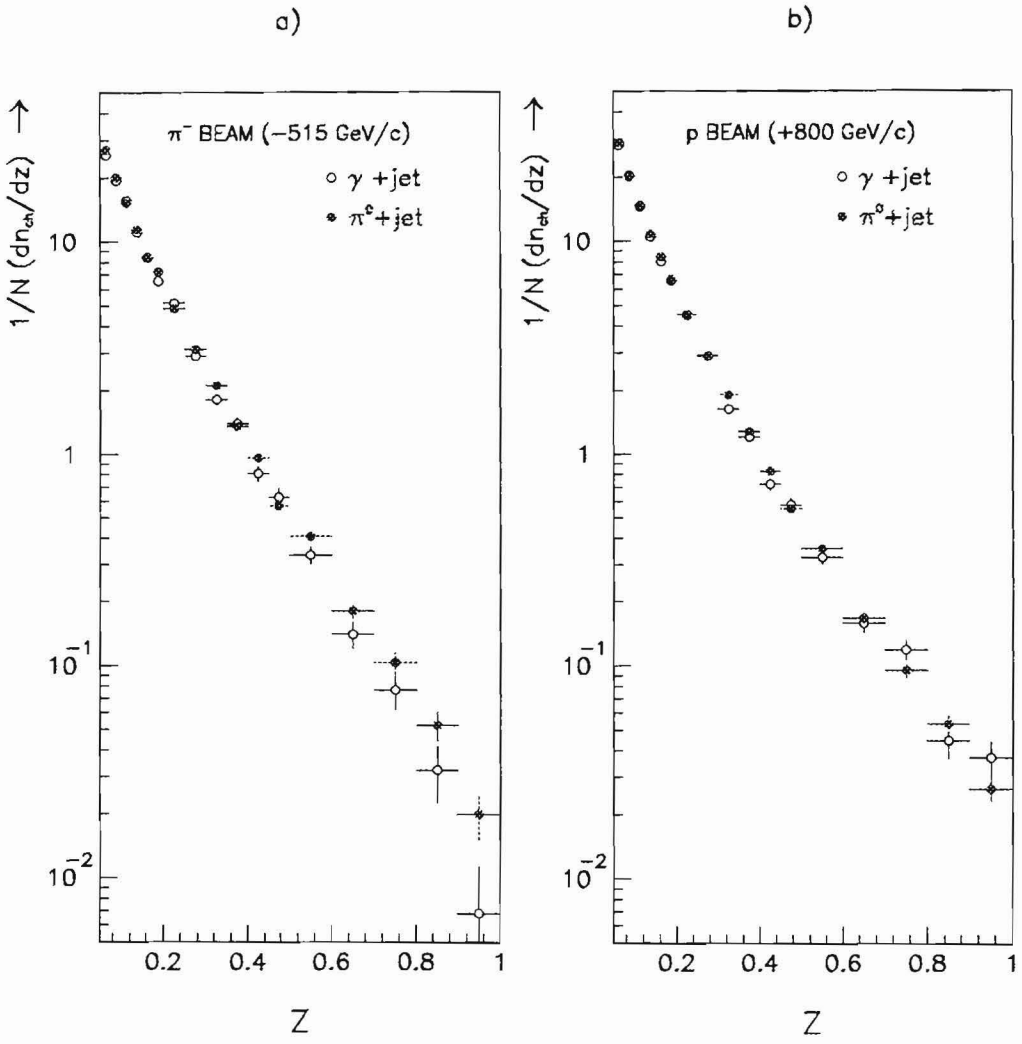

Figure 6.12: The fragmentation function of π^0+jet and background-subtracted γ+jet with π^- (a) and p (b) beam types.

Note that $N_{\gamma}^{mc}/N_{\pi^0}^{mc}$ is used as a measure of what fraction of our γ+jet data actually comes from π^0+jets.

Now, the contribution of those fake γ+jets to the fragmentation function can also be determined in the same fashion. In analogy with equation 6.8, the corrected fragmentation function for the γ+jet data should be given by

$$\begin{aligned}(dn_{ch}/dz)_{\gamma}^{true} &= (dn_{ch}/dz)_{\gamma}^{exp} - (dn_{ch}/dz)_{\gamma}^{fake} \\ &= (dn_{ch}/dz)_{\gamma}^{exp} - (dn_{ch}/dz)_{\pi^0}^{exp} \times \frac{(dn_{ch}/dz)_{\gamma}^{mc}}{(dn_{ch}/dz)_{\pi^0}^{mc}}, \end{aligned} \tag{6.9}$$

where (dn_{ch}/dz) represents an unnormalized fragmentation function, meaning a number of charged particles in a given range of dz.

It should be noted from Figure 6.11 that the fragmentation function of fake γ+jets seems a bit harder than that of π^0+jets. The main reason for this effect might be explained as follows. The trigger side p_T of the fake γ+jet is smaller than that of the original π^0+jet because of the loss of a low energy photon resulting from the mis-reconstruction. As a result, when the fragmentation variable z is rescaled to the trigger jet, the fragmentation becomes harder. This effect has been taken care of in Equation 6.9.

Combining Equation 6.8 and 6.9, the background subtracted fragmentation function for γ+jet events can be written as

$$D(z)_{\gamma}^{true} = \frac{1}{N_{\gamma}^{true}} \cdot (dn_{ch}/dz)_{\gamma}^{true}. \tag{6.10}$$

Figure 6.12 shows the fragmentation function of π^0+jet and background subtracted γ+jet events for π^- and p beam types.

6.5 Angular Distribution

In the parton-parton center of mass frame, the distribution of $\cos\theta^*$ is normalized to the number of events at $\cos\theta^* = 0$ and fitted with a function

$$\frac{1}{2}\left[\frac{1}{(1+\cos\theta^*)^a} + \frac{1}{(1-\cos\theta^*)^a}\right]. \tag{6.11}$$

Four different data samples, γ+jets and π^0+jets with π^- and p beam types, are used for the measurement of the angular distribution. The emphasis is on the comparison of γ+jets and π^0+jets for each beam type.

The results from the data are compared with the MC predictions to see how well they agree with QCD predictions which were discussed in Chapter 1.

6.5.1 Kinematic Variables

Let us consider a hard scatter process that produces a di-jet event. We determine the direction and magnitude of jets during the jet reconstruction in the hadron center of mass frame. In order to measure $\cos\theta^*$, we have to boost these quantities to the parton center of mass frame where the two jet directions are back to back as illustrated in Figure 6.13. This Lorentz boost is performed along the direction of the incident hadrons, assuming that intrinsic transverse momentum (k_T) effects can be ignored. The amount of the boost, η_b, and the pseudorapidity of the di-jet system in the parton center of mass frame, η^*, are determined by solving the following set of equations where it is assumed that the jet and corresponding parton pseudorapidities are the same.

$$\begin{aligned} \eta^*_{tjet} &= \eta_{tjet} + \eta_b \\ \eta^*_{rjet} &= \eta_{rjet} + \eta_b = -\eta^*_{tjet}, \end{aligned} \tag{6.12}$$

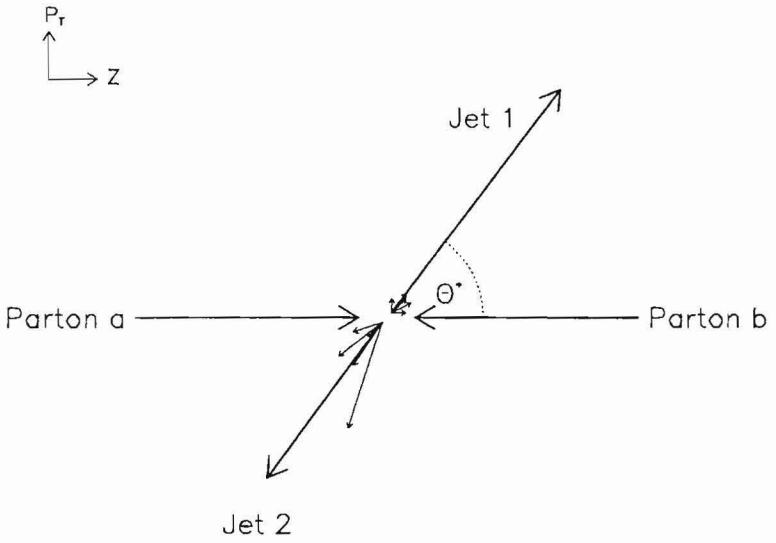

Figure 6.13: The hard scattering in the parton-parton center of mass frame.

where η_{tjet} and η_{rjet} are the pseudorapidities of the trigger and recoil jet, respectively. So,

$$\eta^* = \eta^*_{tjet} = -\eta^*_{rjet} = 0.5 \times (\eta_{tjet} - \eta_{rjet}) \tag{6.13}$$

$$\eta_b = 0.5 \times (\eta_{tjet} + \eta_{rjet}), \tag{6.14}$$

where we take the direction of η^* as the direction of η^*_{tjet}. The corresponding angle $\cos\theta^*$ and the trigger particle's center of mass momentum p^* for the di-jet system can be determined by

$$\cos\theta^* = \tanh(\eta^*) \tag{6.15}$$

$$p^* = p_T \times \cosh(\eta^*) = p_T / \sin\theta^*. \tag{6.16}$$

6.5.2 Biases in $\cos\theta^*$

The distributions of $\cos\theta^*$ contain two sources of bias, one from the p_T requirement on the trigger particle and the other from the acceptance of the detector. In order to observe the correct angular distribution, these biases should be eliminated from the data.

The angular distribution of the di-jet system can be measured as a differential cross section $d^2N/dp^* d\cos\theta^*$, where we integrate over a range of the trigger particle's center of mass momentum p^*. With the p_T threshold imposed on the trigger particle, the range of integration (especially, the minimum value) for p^* should depend on a given p_T cut and a range of $\cos\theta^*$. Figure 6.14 illustrates the relationship between the p_T threshold and the center of mass momentum p^*. The shadowed region bounded by p^*_{min} and p^*_{max} above the p_T cut indicates the region without any bias from the p_T threshold. In order to measure the angular distribution over the range $|cos\theta^*|$ <0.55 in the data with a trigger particle p_T cut of 5.5 GeV/c, p^* should be greater than $\sim$

6.6 GeV/c^2. Figure 6.15 plots p_T vs $\cos\theta^*$ and shows the effect of the transformation to p^*. For the purpose of eliminating the trigger bias, the p^* in Eq. 6.16 is chosen as the p^* of the trigger particle, rather than that of the trigger jet, because the bias comes from the p_T requirement on the trigger particle.

The other bias comes from the limited geometrical acceptance of the detector, especially the calorimeter. Figure 6.16 shows η_{tjet} vs η_{rjet} for the γ+jet data on the horizontal-vertical axis and the diagonal axes are the transformation to η^* vs η_b. Since $\cos\theta^* = \tanh(\eta^*)$, the $\cos\theta^*$ range of interest is determined by the range of η^*, or the ranges of rapidity coverage for the trigger and recoil jets. The limits on the η_{tjet} and η_{rjet} indicated by the dotted line in Figure 6.16 imply that $\eta^* = 0.62$ is the maximum value that could be measured in the uniform region of acceptance; this corresponds to $\cos\theta^* \sim 0.55$.

The $|cos\theta^*|$ distribution of π^0+jet and γ+jet events are shown in Figure 6.17 for 515 GeV/c π^- beam data and Figure 6.18 for 800 GeV/c p beam data. The distributions are normalized to the number of events at $cos\theta^* = 0$ and the curves are fitted functions as illustrated in Eq. 6.11. Even before background subtraction, the difference between the π^0+jet and γ+jet distributions for both π^- and p beam types is striking. As a result of fitting, $a = 2.75\pm0.08$ (2.23 ± 0.11) for π^0+jet (γ+jet) with the π^- beam type and $a = 2.86\pm0.06$ (2.15 ± 0.12) for π^0+jet (γ+jet) with the p beam type.

6.5.3 Background Subtraction

The procedure of background subtraction for the $\cos\theta^*$ distribution for γ+jet is not much different from the procedure for the fragmentation study. The same HERWIG MC model was used to generate high p_T π^0+jet and γ+jet events with a full detector simulation. After making the exact same analysis cuts which eliminate biases, the ratio of the number of fake γ+jets to that of π^0+jets is determined.

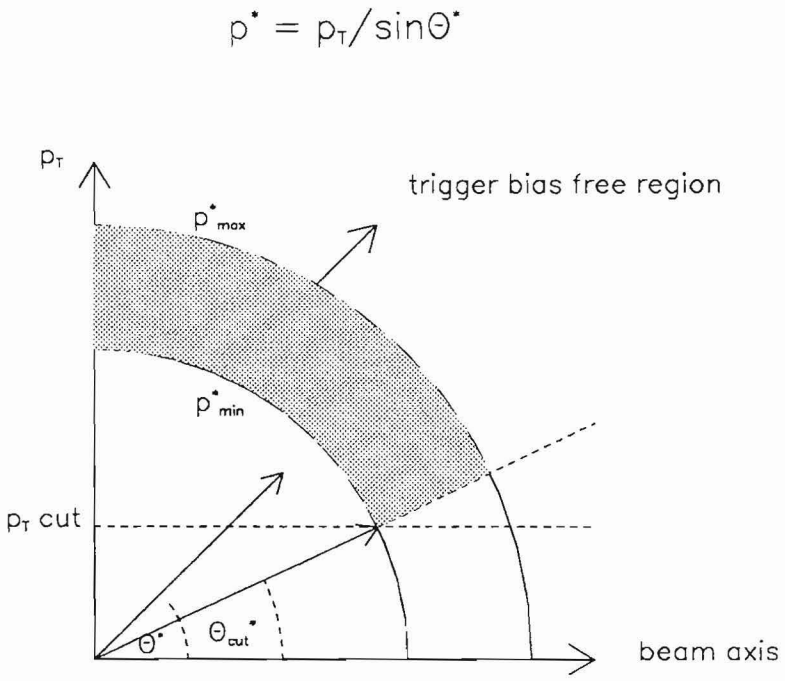

Figure 6.14: A graphical display of the relation between the p_T and p^* of the trigger particle. The shadowed region is the bias-free region.

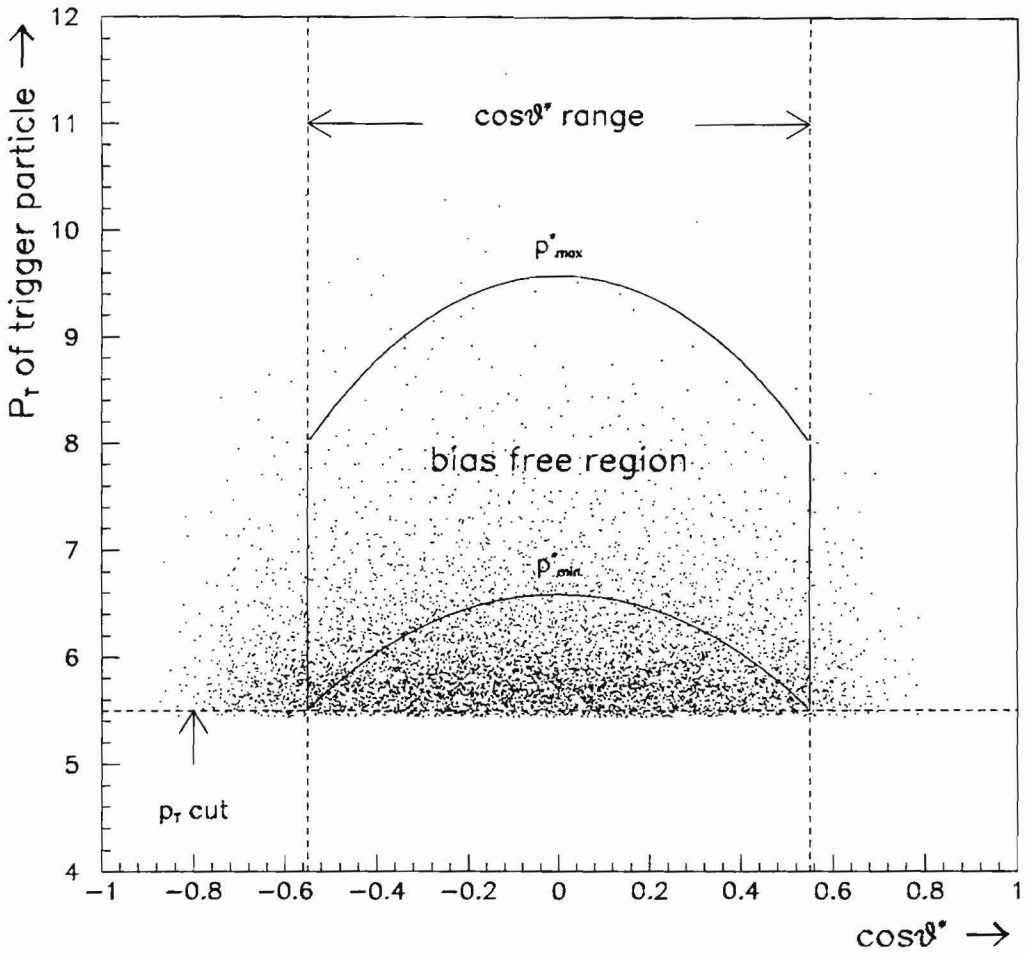

Figure 6.15: The effect of mass cut on angular distribution. The vertical lines represent the $\cos\theta^*$ ranges and the horizontal line shows the p_T cut of 5.5 GeV/c. The lower curve shows the p^*_{min} value of 6.6 GeV/c.

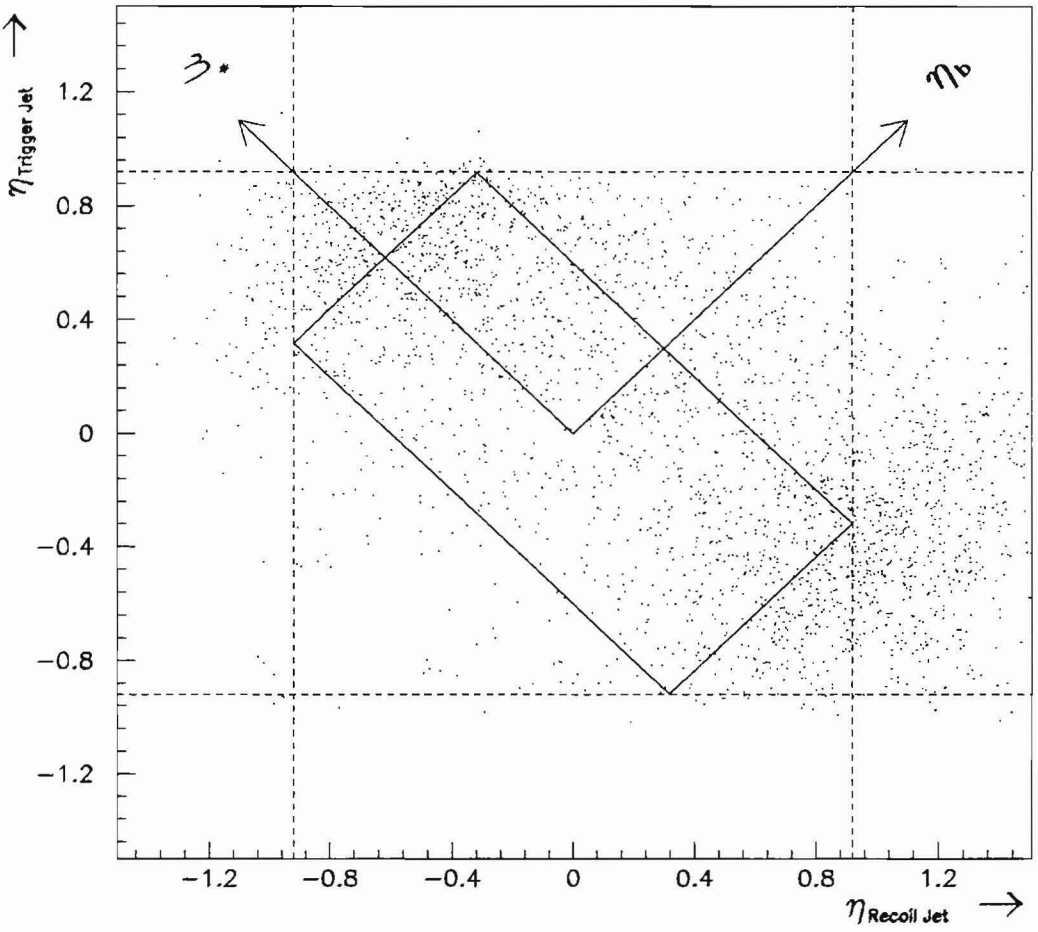

Figure 6.16: The rapidity of the trigger jet vs the rapidity of the recoil jet. The diagonal axes are the sum (η_b) and difference (η^*) axes. The dotted lines indicate the limits in the rapidity of the jets. The inner area of the rectangle represents the region where the acceptance is uniform and the upper and lower limits in η^* corresponds to the $|\cos\theta^*| < .55$.

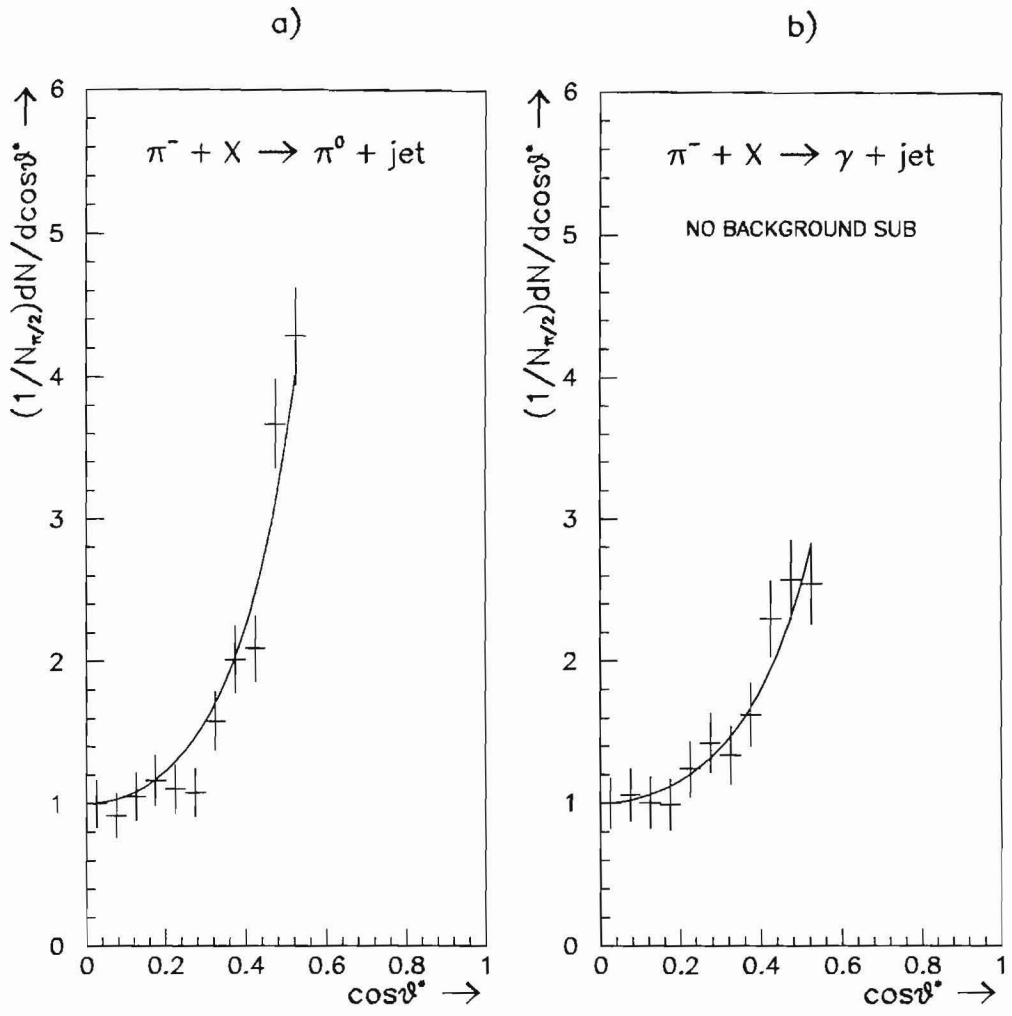

Figure 6.17: The $|\cos\theta^*|$ distribution of π^0+jet (a) and unsubtracted γ+jet (b) for π^- beam. The distribution is normalized to the number of events at $\cos\theta^* = 0.$ and the curve represents the fitted curve to the data points.

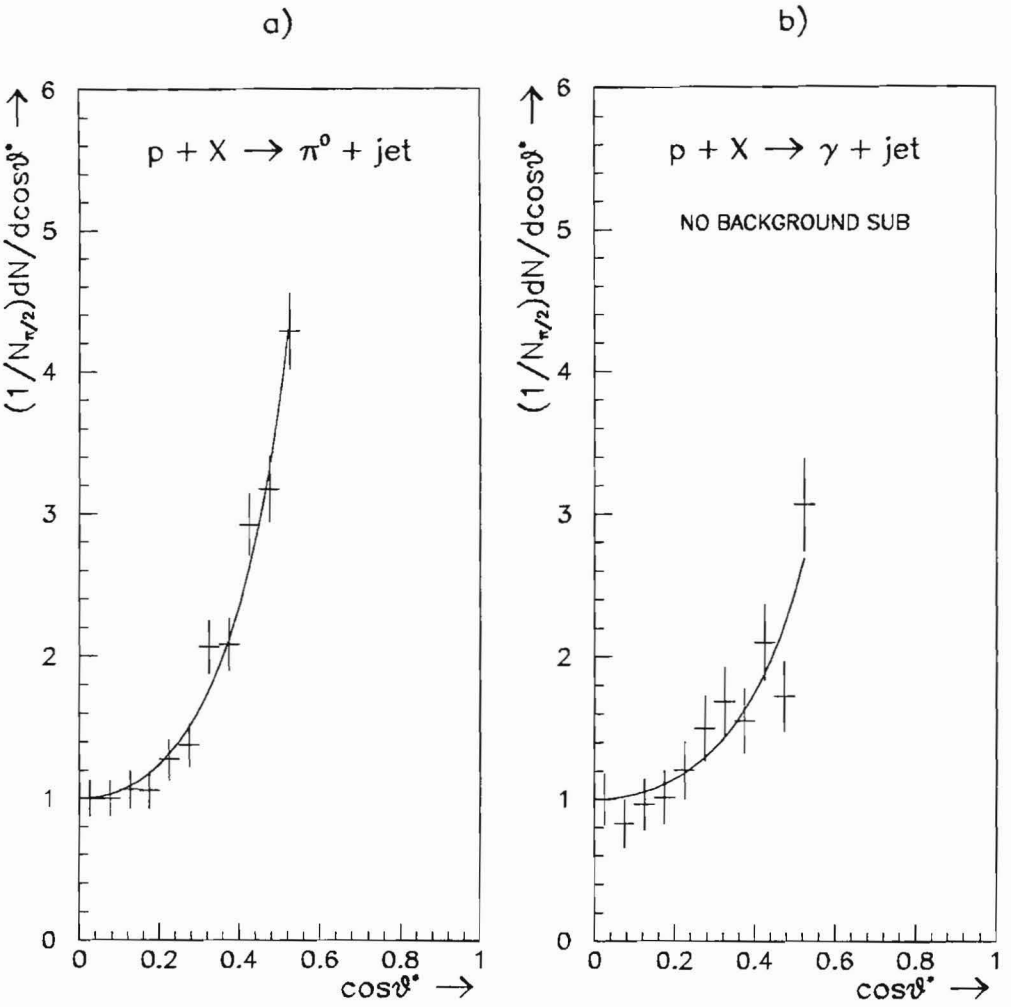

Figure 6.18: The $|\cos\theta^*|$ distribution of π^0+jet (a) and unsubtracted γ+jet (b) for p beam. The distribution is normalized to the number of events at $\cos\theta^*= 0.$ and the curve represents the fitted curve to the data points.

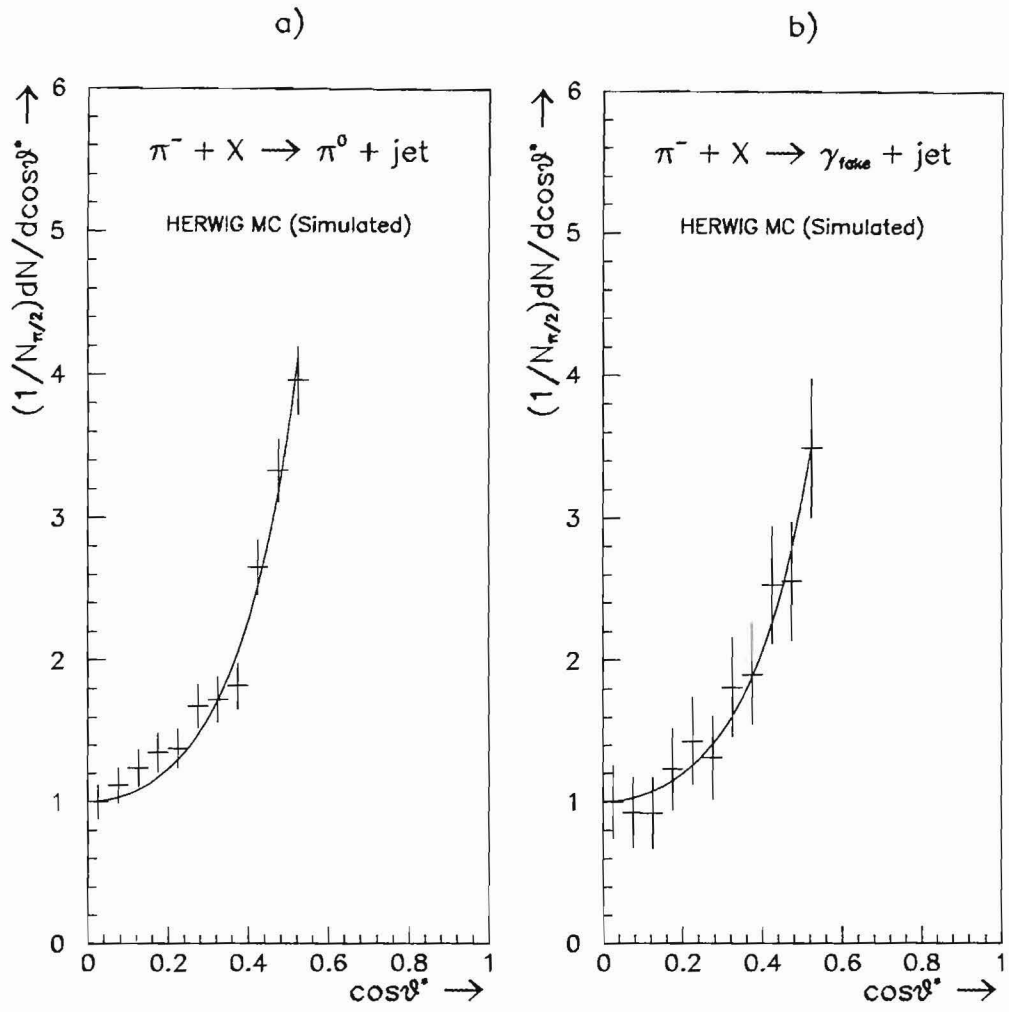

Figure 6.19: $|cos\theta^*|$ plots of π^0+jet (a) and fake γ+jet (b) events from π^0+jet Monte Carlo events. The events are generated using HERWIG and simulated using GEANT package.

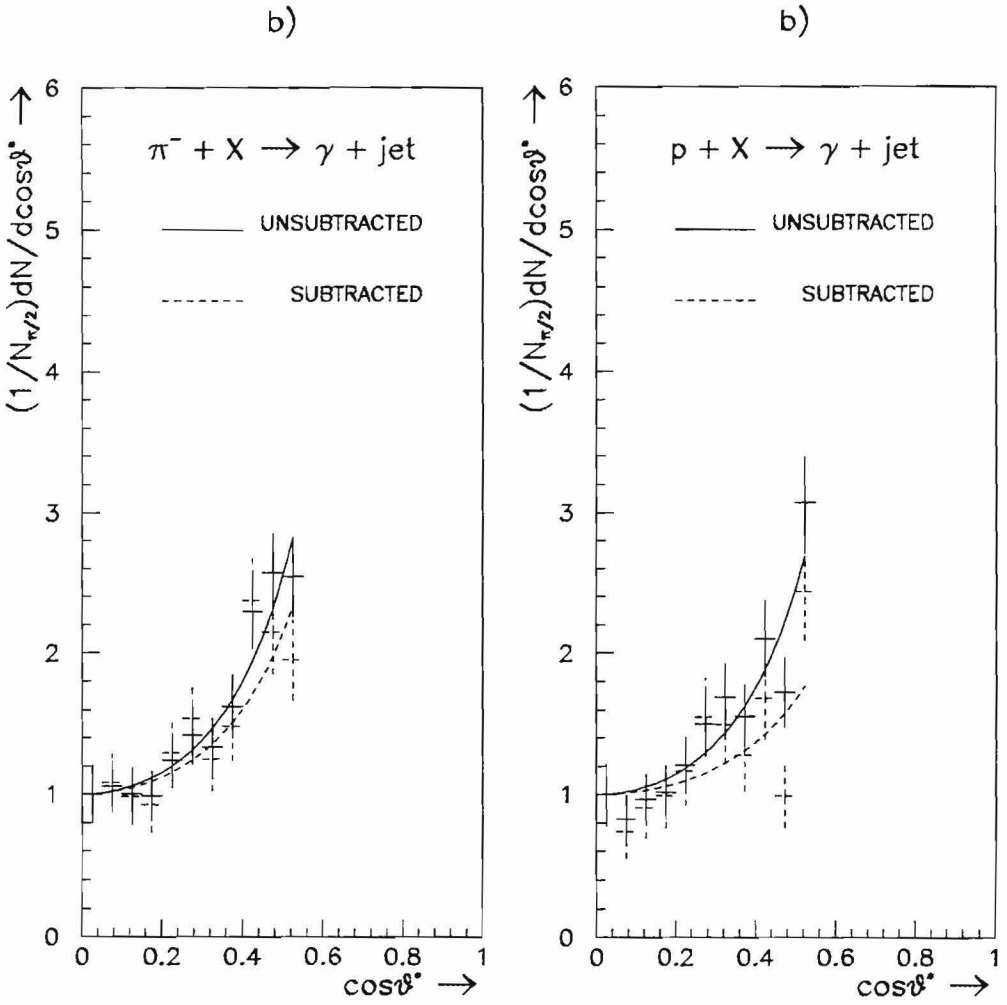

Figure 6.20: $|cos\theta^*|$ distribution of background subtracted γ+jet events, compared with unsubtracted distribution for both π^- (a) and p (b) beam types.

Because there is no reason to believe that the $cos\theta^*$ distribution for fake γ+jet is different from that for π^0+jet, the contribution was subtracted directly from the π^0+jet data,. Figure 6.19 shows the Monte Carlo prediction of $cos\theta^*$ distribution for π^0+jet and fake γ+jet events. The results of background subtraction is presented in Figure 6.20.

6.6 Nuclear Effects

Our data can also be used to investigate nuclear effects in γ+jet and π^0+jet production. The data can be separated into different groups based on the materials in which the primary vertex occurred. The characteristics of E706 targets are listed in Table 2.1. We focus our analysis of nuclear effects on the correlation of trigger and recoil jets in the transverse momentum plane.

Results reported from experiment (Fermilab E609) [16] showed that the distribution of azimuthal opening angle ($\Delta\phi$) between two jets from a Pb target was broader than that from an H target. They also showed that the angular width of a jet was nearly independent of atomic mass A, which indicated that the fragmented hadrons did not contribute much to the A dependence. Moreover, there are evidences [52] [53] that initial-state partons experience much less nuclear scattering than final-state partons. This suggests that the broadening of the back-to-back azimuthal correlation of outgoing di-jets is mainly caused by multiple scattering of outgoing partons.

The correlation in ϕ between the trigger and recoil jet in the plane transverse to the beam are studied as a function of the target nucleus. In Figures 6.21 and 6.22, the azimuthal angle difference $\Delta\phi$ between trigger and recoil jet is plotted for different nuclear target materials. There is an indication that as the target nucleus gets massive, the $\Delta\phi$ distribution becomes broader.

As discussed in Chapter 1, an appropriate parameter commonly used to to observe

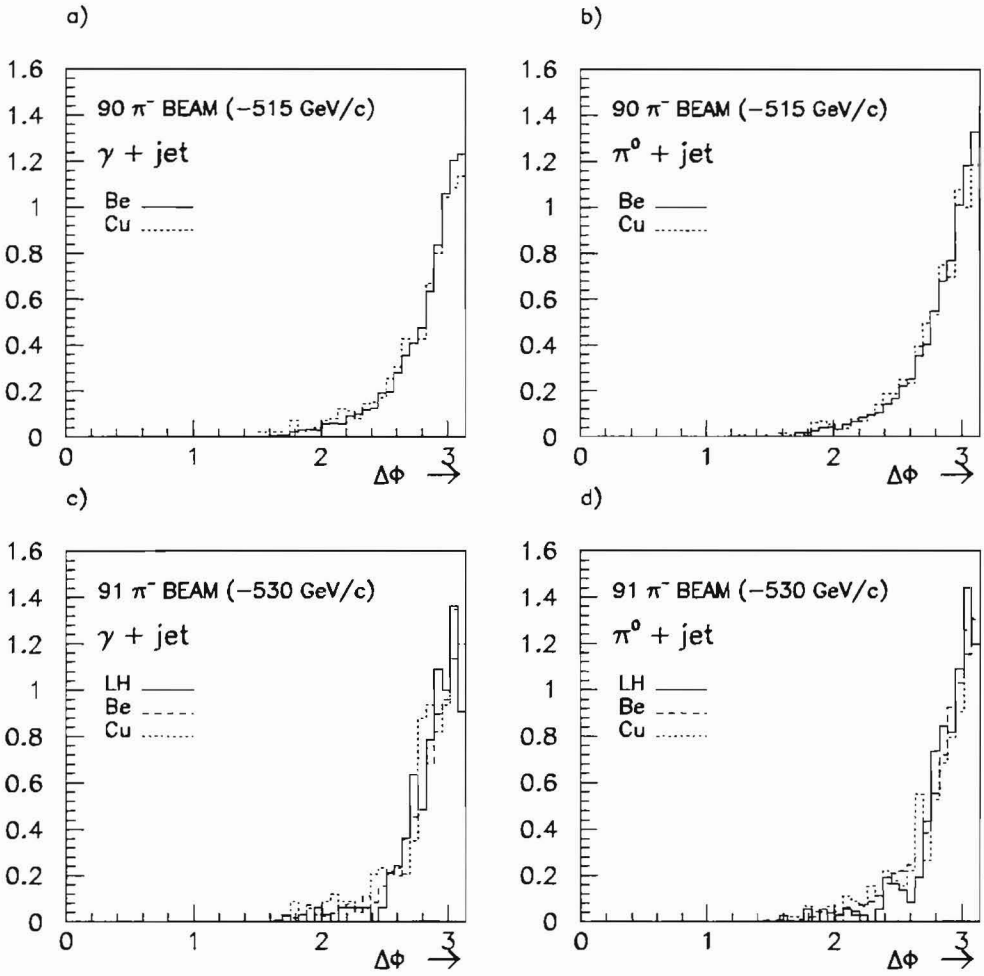

Figure 6.21: Decorrelation of $\Delta\phi$ in π^- beam

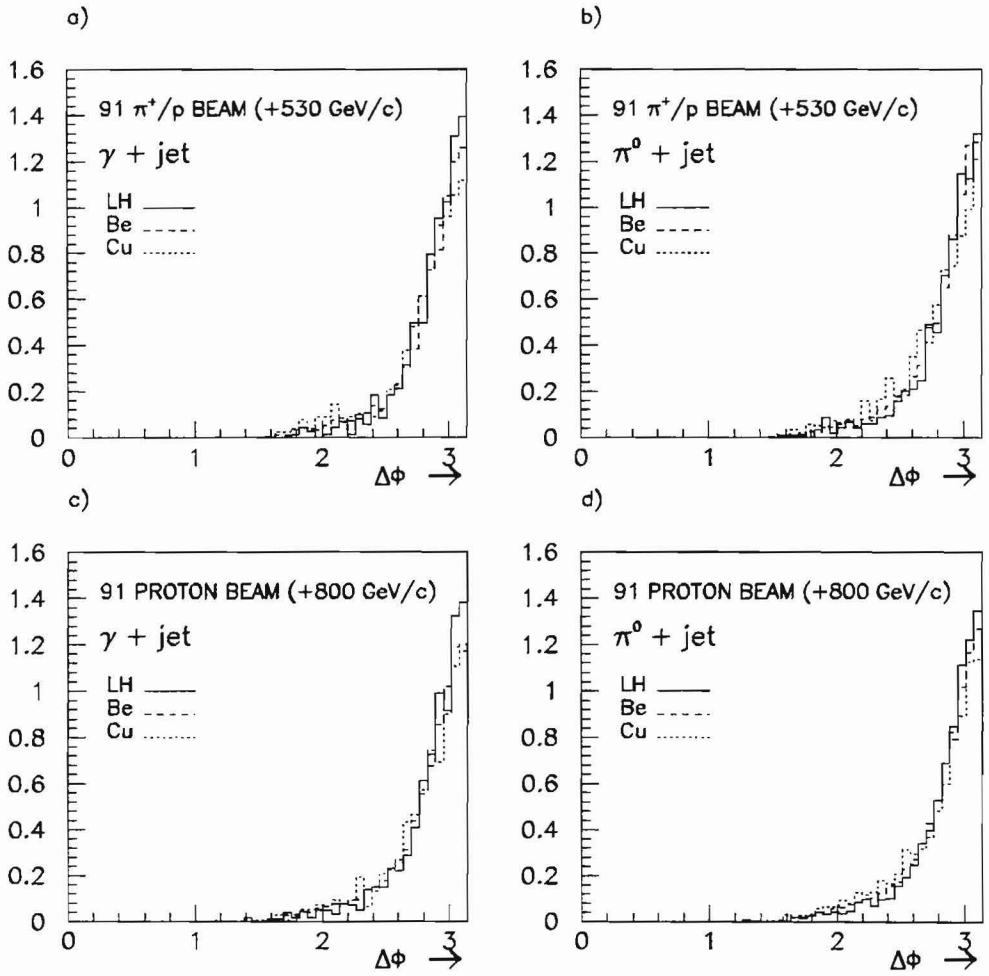

Figure 6.22: Decorrelation of $\Delta\phi$ in π^+ and p beam

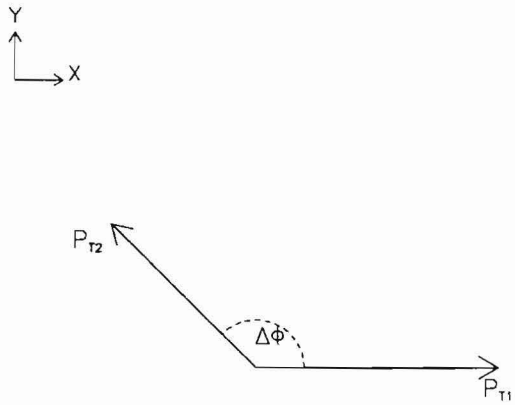

Figure 6.23: The definition of $k_{T\phi}$

nuclear effects is the RMS value of $k_{t\phi}$. We define the momentum of the di-jet system transverse to the scattering plane as

$$k_{T\phi} = \frac{p_{T1} + p_{T2}}{2} \cdot sin(\Delta\phi) \tag{6.17}$$

where p_{T1} and p_{T2} are the transverse momenta of two jets. Figure 6.23 illustrates how $k_{t\phi}$ can be measured. We plot the distributions of $k_{T\phi}$ in Figure 6.24 for Be, Cu, Si and Liquid Hydrogen targets for π^0+jet events in the 800 GeV/c p beam data. The silicon data comes from reconstructed primary vertices in the silicon strip detectors. It turns out that these $k_{T\phi}$ distributions get broader as the nuclear mass gets larger.

The distribution of $< k_{t\phi}^2 >$ can be extracted from Figure 6.24. Since the mean value of the $k_{t\phi}$ distribution is zero, the mean value of $k_{t\phi}^2$ equals the square of the RMS of the $k_{t\phi}$ distribution (σ^2).

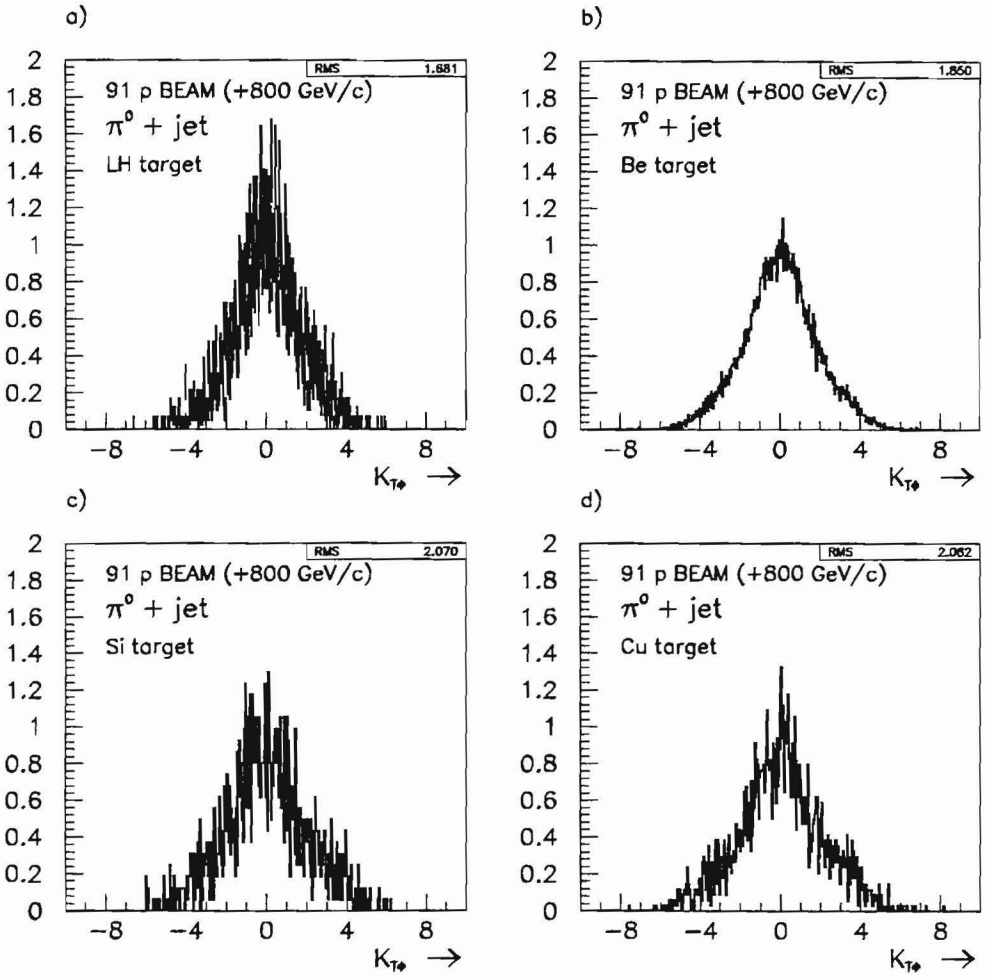

Figure 6.24: $k_{T\phi}$ distribution for Be, Cu, Si, LH target

CHAPTER 7

Results and Conclusion

So far, we have studied the structure of recoiling jets, and the correlation of trigger and recoil jets in azimuthal and rapidity space by the reconstruction of jets in events containing high p_T π^0's and direct photons. Monte Carlo simulation has been used extensively to subtract the background contribution of fake γ+jet events and to compare the results with predictions. The Monte Carlo also provided insights to guide our study of jets.

We present the results of an analysis on fragmentation, angular distributions and nuclear effects, along with the comparisons with MC simulation and the results from other experiments.

7.1 Fragmentation

Four different samples of recoil jets from the data are compared with each other in searching for differences between quark and gluon jets. The data were selected with a p_T cut of 5.5 GeV/c on trigger particles (π^0's and/or γ's) and a rapidity range, $|\eta| < 0.75$, for both trigger and recoil jets. The background was subtracted for γ+jets, according to the method described in Chapter 6. In Figure 7.1, the fragmentation functions of four different jets are plotted, along with the MC comparisons. In order

to make comparisons easier, MC fragmentation functions were fitted with a form $Az^{-B}\exp^{-Cz}(1-z)^{D}$ which does not have an obvious theoretical basis [30].

According to QCD predictions on the quark and gluon content of recoil jets (Table 6.2), recoil jets in direct photon events produced with a π^- beam are expected to be the only gluon-dominated jets among our data. The fragmentation function of recoil jets for γ events produced with a π^- beam looks considerably softer than that for π^0 events with the same beam type. The fragmentation of the recoil jets in π^0 and γ events produced with a p beam do not differ substantially from one another.

Let us compare the data with fully simulated MC predictions. MC fragmentation functions for π^0 and γ events are compared with the data in Figure 7.1. Figure 7.1 also shows MC fragmentation functions for pure quark and gluon jets, which were extracted from the di-jet sample. Those two outermost curves naturally define the limits on both extreme hardness and softness. Based on qualitative observation, we conclude that the gluon content of the recoil jet in π^0 events should be a bit more than the prediction ($\sim 25\%$ according to Table 6.2) and the discrepancy in the fragmentation of γ+jet events between MC and the data is quite apparent.

The errors in the data fragmentation functions are statistical only and do not include systematic uncertainties such as the reconstruction efficiency of recoil jets and trigger particles and the limited acceptance due to detector geometry. These effects cancel out in the comparisons of the various data sets. All known systematics are included in the MC data.

Figure 7.2 shows ratios of the fragmentation functions that were presented in Figure 7.1, now plotted in a linear scale. They are also compared with MC. An advantage of these plots is the cancellation of common systematic effects. Figure 7.2a and 7.2c represent the ratio of the "soft" fragmentation function (γ+jets with a π^- beam to the "hard" fragmentation functions (π^0+jets with a π^- beam and γ+jets with a p beam), whereas Figure 7.2b and 7.2d compare "hard" and "hard" fragmen-

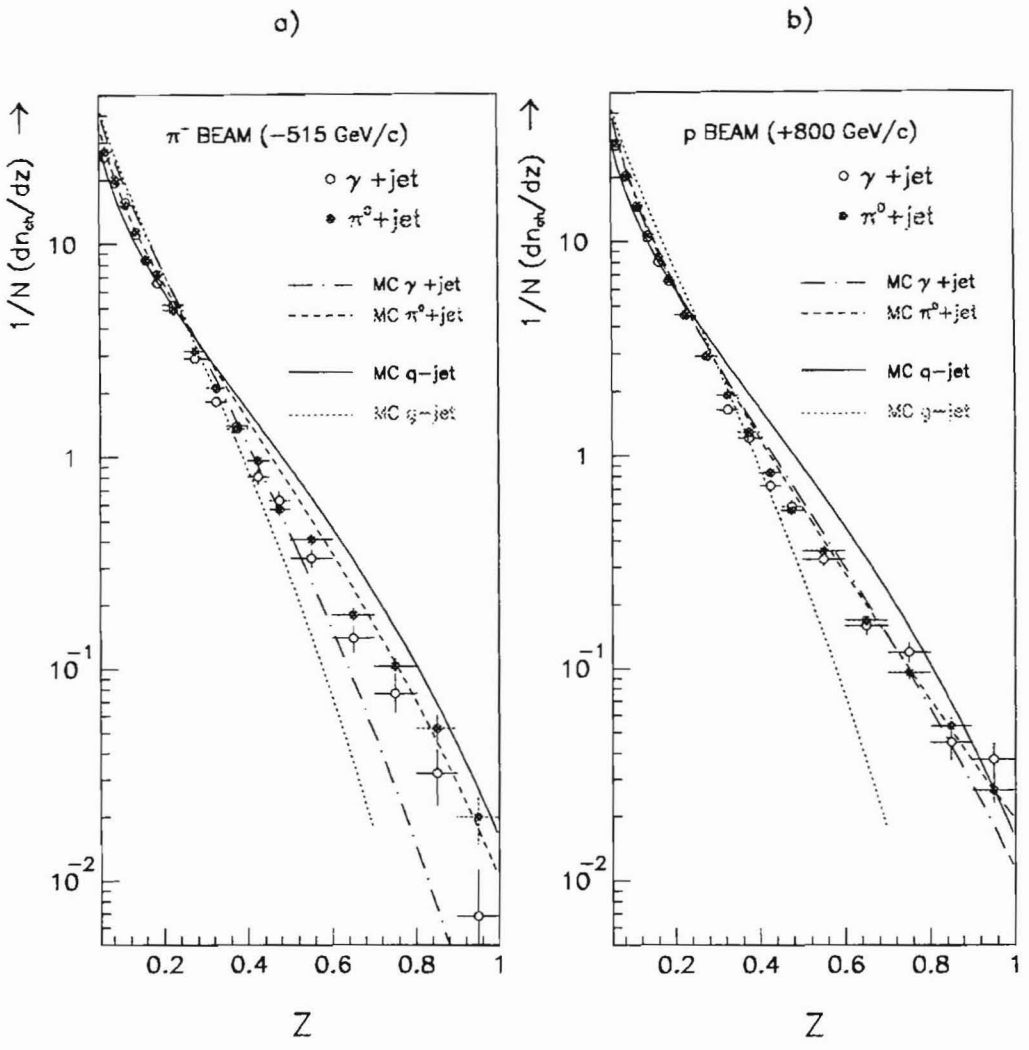

Figure 7.1: The fragmentation function of π^0+jet and background subtracted γ+jet with π^- (a) and p (b) beam types, are compared with fully detector simulated MC data. The curves are fragmentation functions fitted to the MC data with a functional form $Az^{-B}\exp^{-Cz}(1-z)^D$. Two outermost curves are for 100% quark and gluon jets.

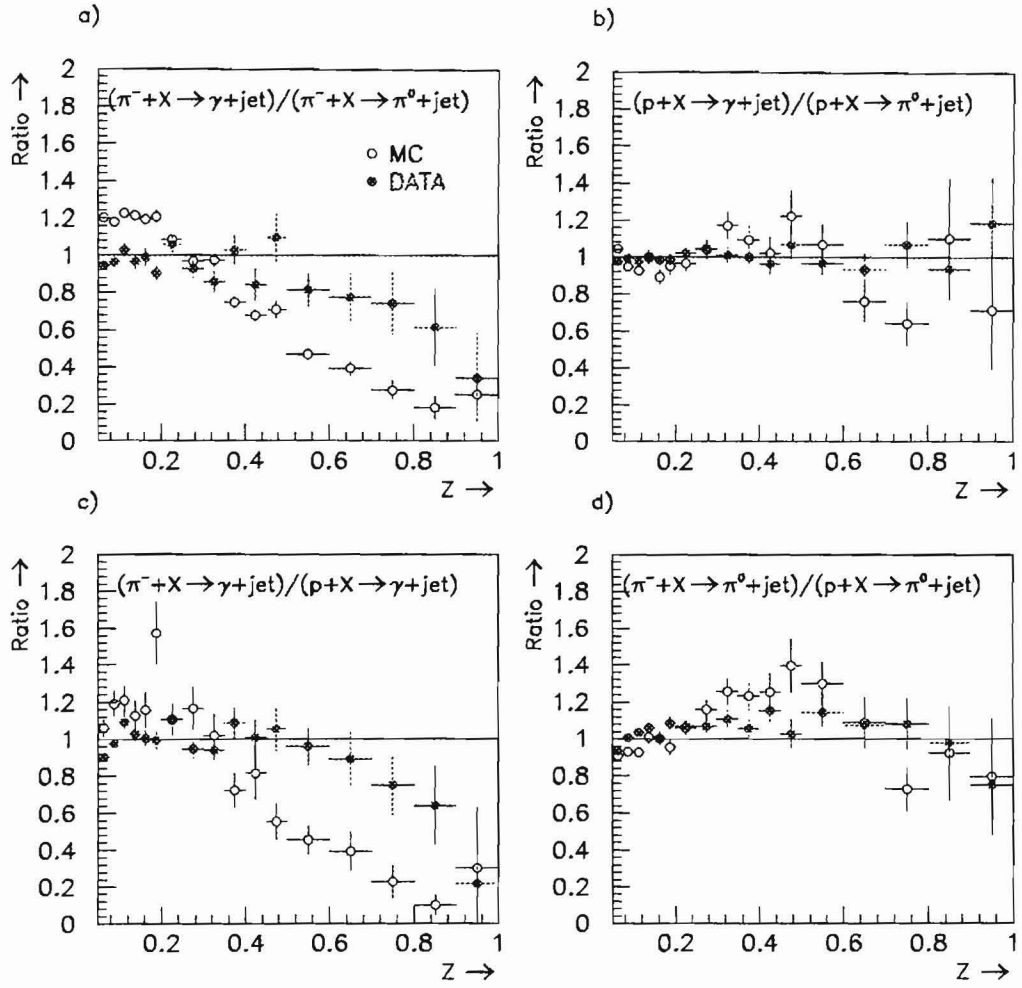

Figure 7.2: The ratio of fragmentation functions: a) γ+jet to π^0+jet with 515 GeV/c π^- beam; b) γ+jet to π^0+jet with 800 GeV/c p beam; c) the same γ+jets with π^- beam to p beam; d) same π^0+jets with π^- beam to p beam. The data are also compared with MC.

tation functions. The difference between gluon-dominated and quark-dominated jets are clearly demonstrated in the data. The corresponding difference is more dramatic in MC than in the data.

7.2 Angular Distribution

As pointed out in the last chapter, we have used the same four sets of data (γ+jets and π^0+jets with 515 GeV/c π^- and 800 GeV/c p beams) for the study of the angular distribution, and our focus is on the comparison of γ+jets and π^0+jets. In Figure 7.3 and 7.4, we present the $cos\theta^*$ distribution of π^0+jets and background subtracted γ+jets produced with π^- and p beams, respectively. All the data were selected with an effective mass cut, M_{eff}=13.171 GeV/c^2 and $|\eta_b| < 0.3$ to eliminate biases. The $cos\theta^*$ distributions from both original HERWIG predictions and detector simulated MC are overlaid with the data. The $cos\theta^*$ distributions were fitted with a function

$$\frac{1}{2}\left[\frac{1}{(1+\cos\theta^*)^a}+\frac{1}{(1-\cos\theta^*)^a}\right]. \tag{7.1}$$

The values of a were determined to be 2.75±0.08 (1.93±0.14) and 2.86±0.06 (1.48±0.20) for γ+jets (π^0+jets) with π^- and p beams, respectively. The differences in the $\cos\theta^*$ distribution between π^0+jet and γ+jet events were clearly observed.

Corrections were applied for the acceptance and the reconstruction efficiency of trigger particles and their conversion probabilities in target materials for both data and MC. With a p_T cut of 5.5 GeV/c, the efficiency for jet finding was around 99%. Note that the data display very good agreement with the simulated MC. The errors shown are statistical only.

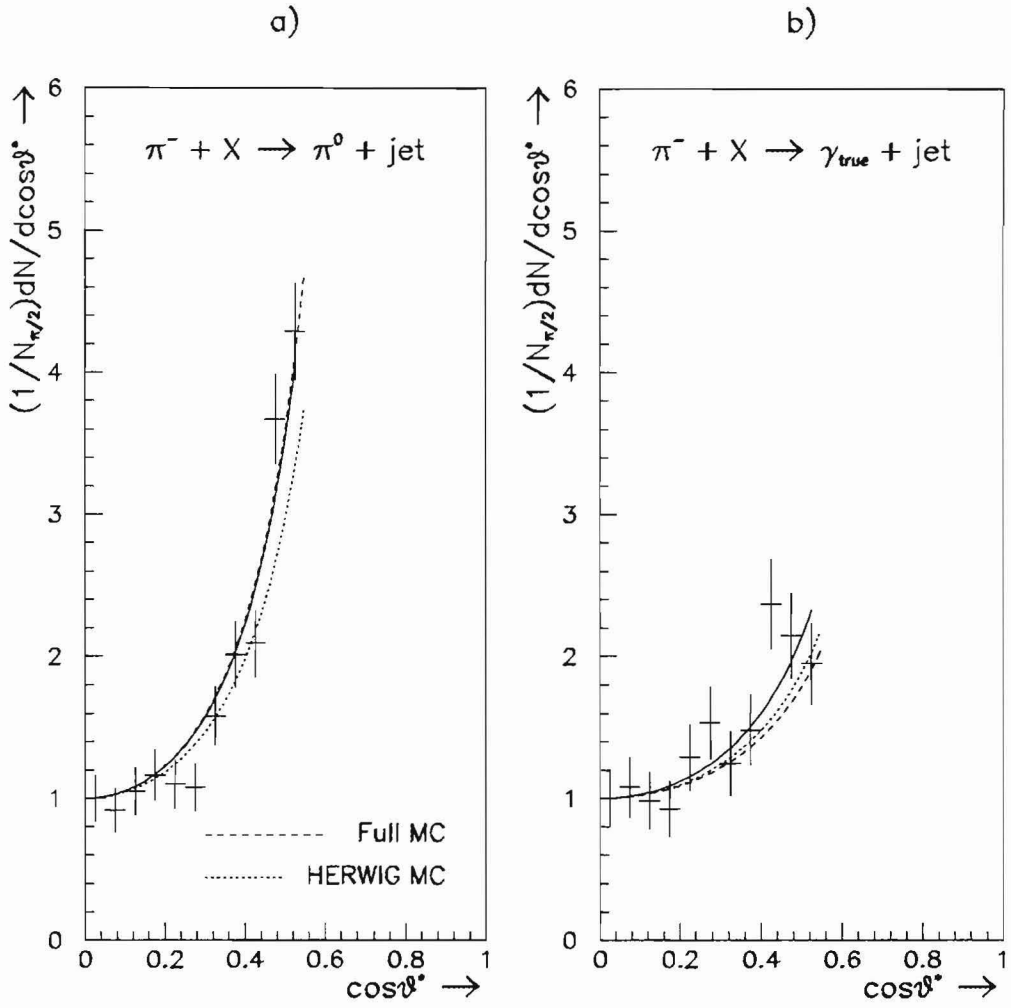

Figure 7.3: $|cos\theta^*|$ distribution of π^0+jet and γ+jet events for 515 GeV/c π^- beam. The solid curves are the best fit to the data and the dotted curves are the predictions from HERWIG (QCD) and fully detector-simulated Monte Carlo results. The background was subtracted in the distribution of γ+jet events.

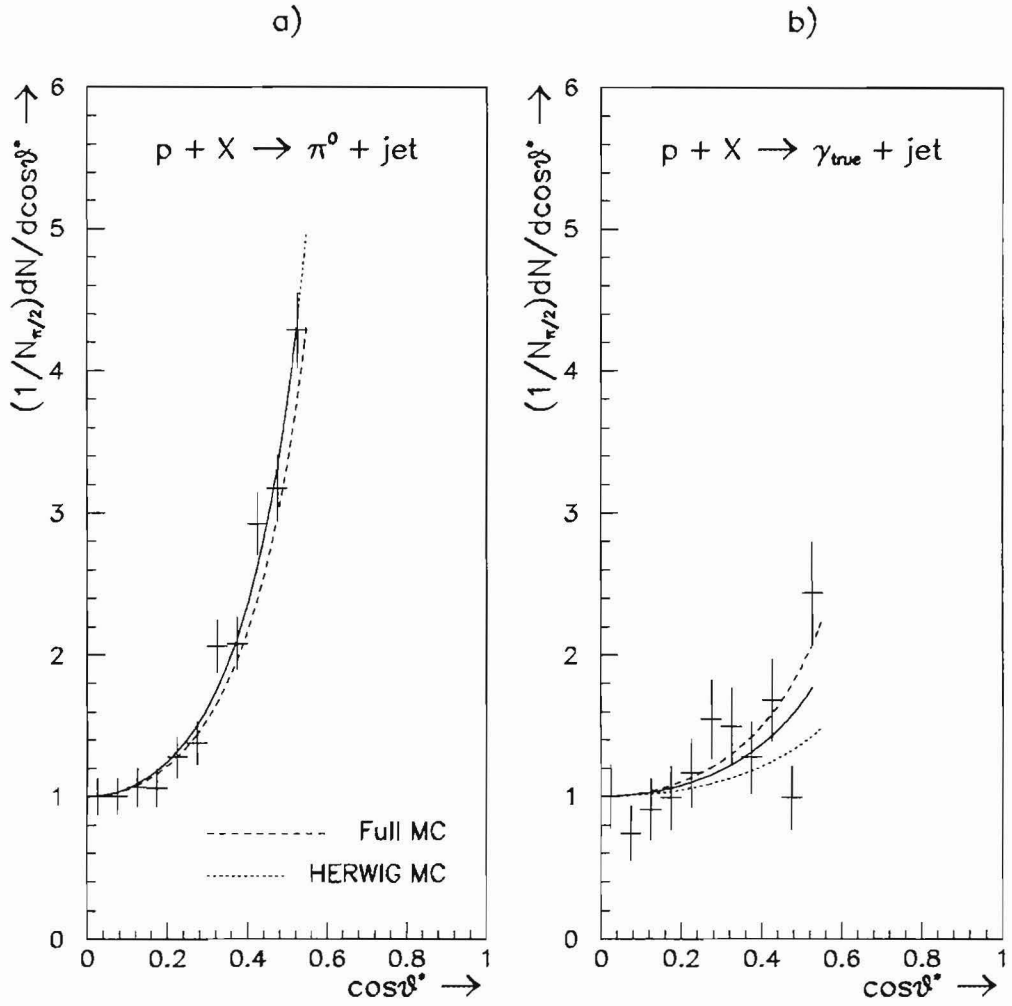

Figure 7.4: $|cos\theta^*|$ distribution of π^0+jet and γ+jet events for 800 GeV/c p beam. The solid curves are the best fit to the data and the dotted curves are the predictions from HERWIG (QCD) and fully detector-simulated Monte Carlo results. The background was subtracted in the distribution of γ+jet events.

7.3 Nuclear Effects

The distribution of $< k_{t\phi}^2 >$ is presented as a function of atomic mass in Figure 7.5, 7.6 and 7.7 for π^0+jets and γ+jets produced with 515 GeV/c π^-, 530 GeV/c and 800 GeV/c p beams. The data were chosen with a p_T cut of 5.5 GeV/c on trigger particles and the rapidity range for both trigger and recoil jets was $|\eta|$ <0.75. Two data sets with the same π^- beams, one for the 1990 run and the other for the 1991 run, were combined in Figure 7.5. The results with 530 GeV/c and 800 GeV/c p beams are shown in Figure 7.6 and 7.7, respectively. The Monte Carlo program was not utilized for the study of nuclear effects. Thus, the γ+jet data were not background subtracted.

In all three data sets, the value of $< k_{t\phi}^2 >$ becomes consistently larger as the target atomic mass increases. This trend is measured quantitatively by fitting the data to the form $< k_{t\phi}^2 > = C_0 + C_1(A-1)^\alpha$. It is expected that the γ+jet data should display less dependence on A when compared to the π^0+jet (di-jet) data. This results from the conjecture that photons should not rescatter as much as partons inside the nucleus. We see no significant differences between the γ+jet and π^0+jet data.

Recently, Fermilab fixed target experiment E683 [54] reported their values of $< k_{t\phi}^2 >$ for photon-nucleus (γA) and pion-nucleus (πA) data. Their targets include hydrogen, deuterium, Be, C, Al, Cu, Sn and Pb and the energy of the beams used vary from 50 GeV to 380 GeV. Since they used photon and π^- beams and selected di-jet events, comparing our results with theirs is of interest. The result from E683 in Figure 7.8 shows a clear nuclear enhancement with increasing atomic mass, which is consistent with our data. They also report that $< k_{t\phi}^2 >$ depends on the energy of the beam and the difference in $< k_{t\phi}^2 >$ between different targets becomes larger as the beam energy increases. The difference of the value of $< k_{t\phi}^2 >$ between Cu and Be targets in our data is larger than that measured by E683. Since our $\sqrt{s}$ is higher

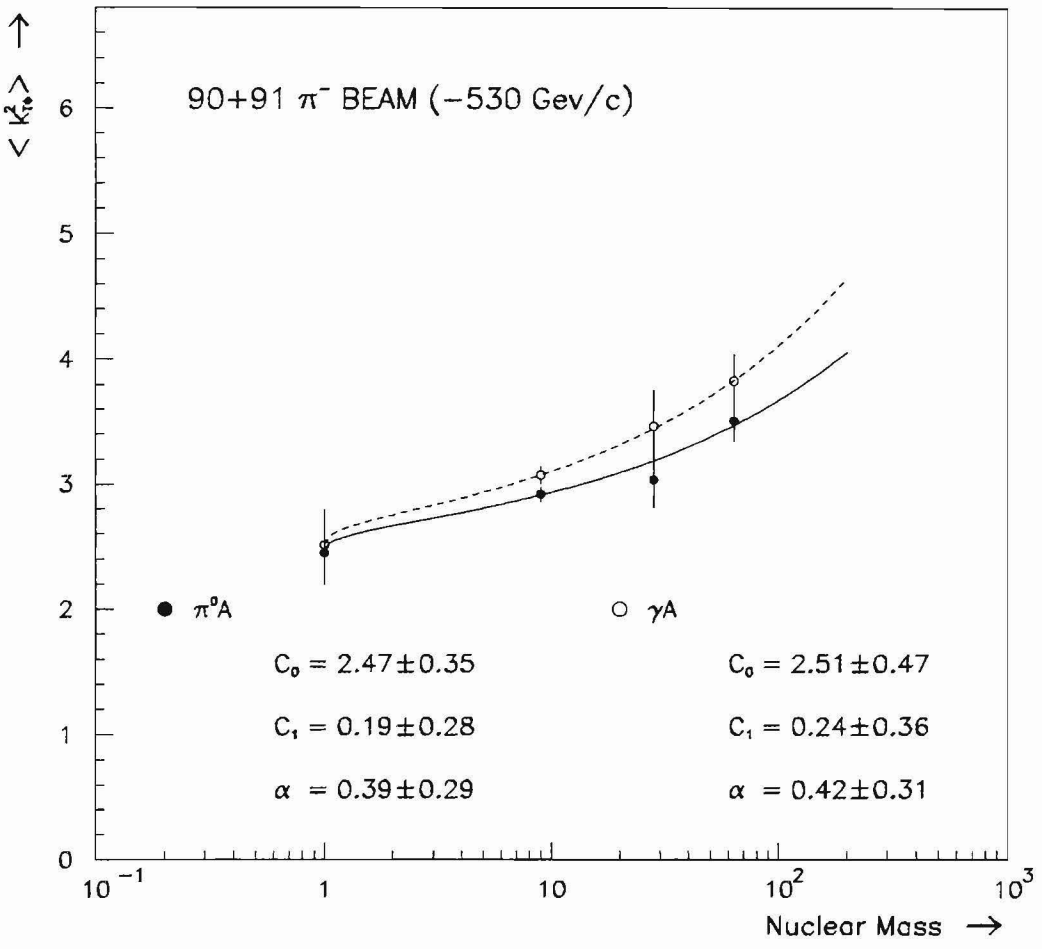

Figure 7.5: $< k_{t\phi}^2 >$ distribution as a function of atomic mass for π^0+jet and γ+jet produced with 515 GeV/c $\pi-$ beams. The curves are the best power law fit to the form $< k_{t\phi}^2 > = C_0 + C_1(A-1)^{\alpha}$. The dotted curve is for γA and the solid curve for π^0A. Be, Cu and Si were used as targets in the 1990 data and Liquid Hydrogen was added in the 1991.

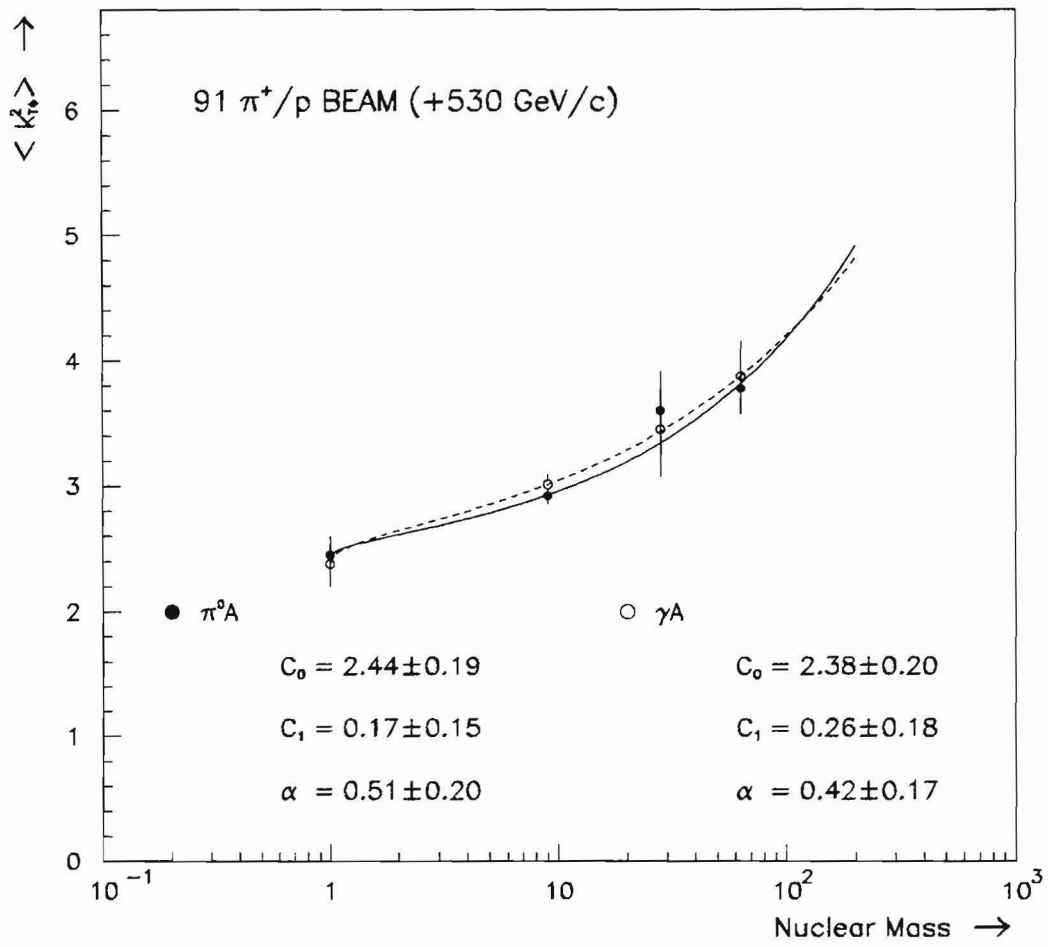

Figure 7.6: $< k_{t\phi}^2 >$ distribution as a function of atomic mass for π^0+jet and γ+jet produced with 530 GeV/c p and π^+ beams. The curves are the best power law fit to the form $< k_{t\phi}^2 > = C_0 + C_1(A-1)^\alpha$. The dotted curve is for γA and the solid curve for π^0A.

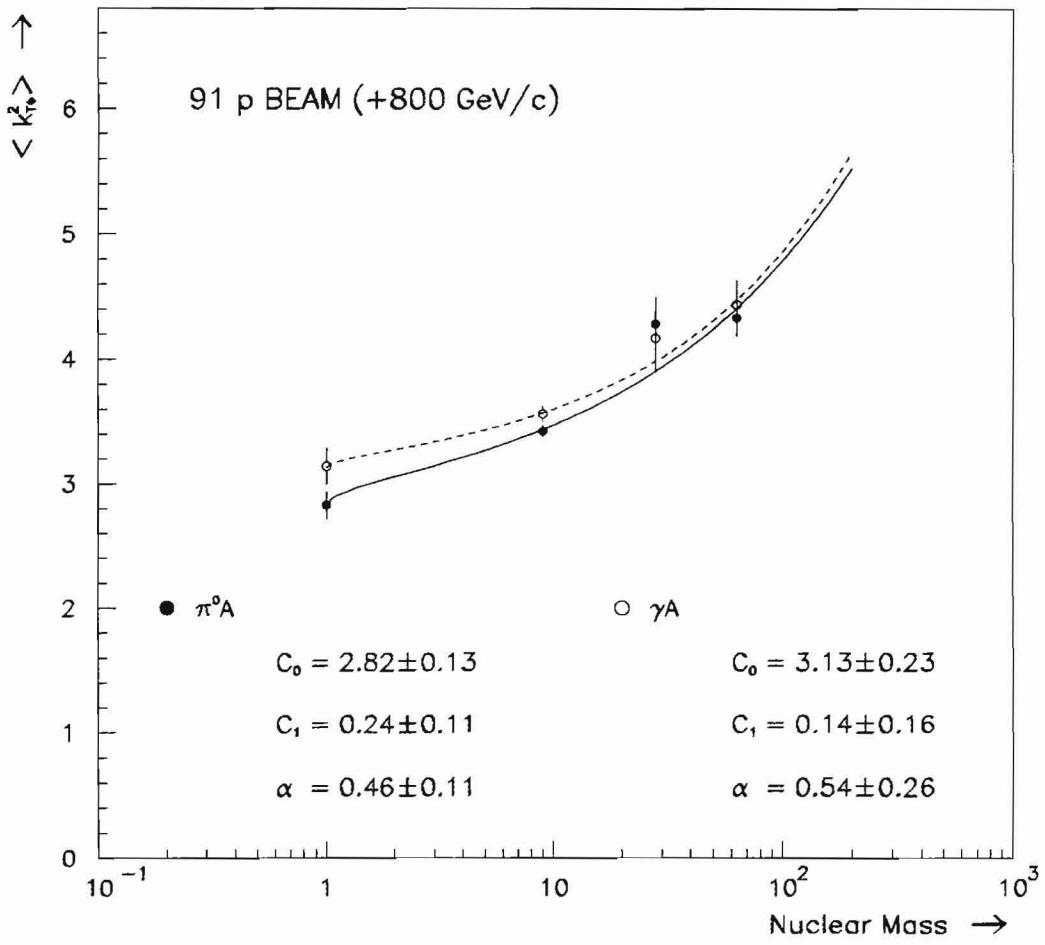

Figure 7.7: $< k_{t\phi}^2 >$ distribution as a function of atomic mass for π^0+jet and γ+jet produced with 800 GeV/c p beams. The curves are the best power law fit to the form $< k_{t\phi}^2 > = C_0 + C_1(A-1)^{\alpha}$. The dotted curve is for γA and the solid curve for π^0A.

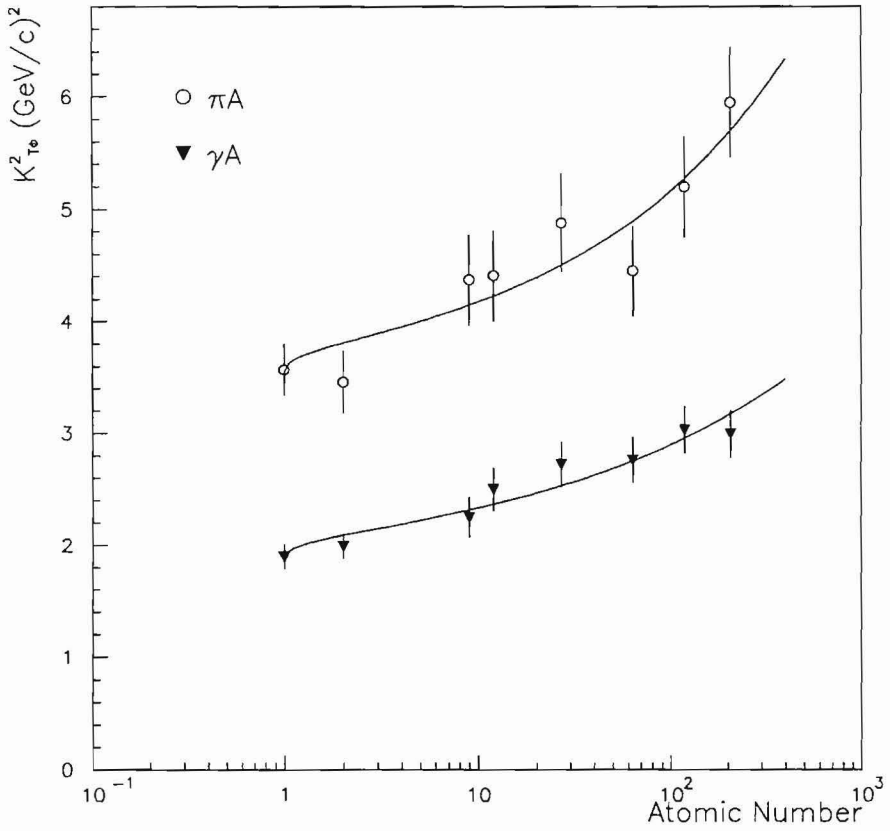

Figure 7.8: $< k_{t\phi}^2 >$ as a function of atomic weight for photon-nucleus (γ A) and pion-nucleus (π A) data in E683 experiment. The curves shown are the best power law fits to the form $< k_{t\phi}^2 >= C_0 + C_1(A-1)^\alpha$. For the photon data the minimum χ^2 fit yields $C_0 = 1.85 \pm 0.10, C_1 = 0.24 \pm 0.10, \alpha = 0.32 \pm 0.08$, and for pion data the fit yields $C_0 = 3.54 \pm 0.22, C_1 = 0.27 \pm 0.21, \alpha = 0.39 \pm 0.15$.

($\sim$ 31.5 GeV), this supports the observation reported by E683.

7.4 Conclusion

We have used the data from 515 GeV π^-, 800 GeV p and 530 GeV p (10% π^+) beams incident on nuclear targets to study the structure of jets for events containing high p_T ($>$ 5.5 GeV/c) π^0's and direct photons. We have measured the fragmentation function of recoiling jets from high p_T π^0's and direct photons. Also, we have studied the rapidity correlation of a two jet system (including γ+jet) for the angular distribution and the azimuthal correlation for the nuclear dependence. The data were compared with both QCD predictions and fully simulated Monte Carlo results.

In the study of fragmentation, we were able to see a small, but visible difference between gluon dominated γ+jets using a π^- beam and other jets which were predicted to be dominated by quarks. The fragmentation of those quark-dominated jets agrees well with MC, but the fragmentation of γ+jets from a π^- beam looks harder than predicted, corresponding to the gluon content of our γ+jets from the π^- beam being less than predicted by MC.

The distribution of $cos\theta^*$ for γ+jets and π^0+jets was measured in the range between 0 to 0.55. The comparison of the data with fully simulated MC shows very good agreement and the differences between γ+jets and π^0+jets were clearly observed.

Nuclear effects in high p_T di-jet and direct photon events were measured with a variable $< k_{t\phi}^2 >$ using liquid hydrogen, Be, Si and Cu targets. The comparison with other experiment (E683) confirms that our nuclear dependence measurements are comparable with their results, considering the difference in the $\sqrt{s}$ and p_T cuts. However, we do not observe a difference between the γ+jet and π^0+jet data as might be expected from the E683 results.

REFERENCES

[1] M. Breidenbach et al., *Phys. Rev. Lett.* 23, 16 (1969)

[2] M. Gell-Mann, *Phys. lett.* 8, 214 (1964).

[3] G. Zweig, CERN report 8182/Th. 401 (1964).

[4] M. Gell-Mann, *Acta Phys. Austriaca Suppl.* 9, 733 (1972).

[5] H. Fritzsch et al., *Phys. Lett.* B47, 365 (1973).

[6] D.J. Gross, F. Wilczek, *Phys. Rev. Lett.* 30, 1343 (1973).

[7] H.D. Politzer, *Phys. Rev. Lett.* 30, 1346 (1973).

[8] J.F. Owens, *Rev. Mod. Phys.* 59, 465 (1987).

[9] A.J. Buras, *Rev. Mod. Phys.* 52, 199 (1980).

[10] A. Kotanski and J. Kubar, Acta Phys. Pol. B11, 669, (1980).

[11] J. Ellis and I. Karliner, Nucl. Phys. B148, 141 (1979).

[12] S. J. Brodsky, T. DeGrand, and R. Schwitters, *Phys. Lett.* 79B, 1585 (1978).

[13] F. Costantini, (UA2 Collaboration), in Proceedings of the 7th Workshop on Proton-Antiproton Collider Physics, June 1988, edited by R. Raja, A. Tollestrup, and J. Yoh (World Scientific, Singapore, 1989), p. 345

[14] F. Abe, *Phys. Rev. Lett.* 71, 679, (1993).

[15] J.W. Cronin et al., *Phys. Rev.* D11 (1975), 3105.

[16] M. Corcoran et al., (E609 Collaboration), *Phys. Lett.* B259, 209 (1991).

[17] C. Stewart et al., (E557 Collaboration), *Phys. Rev.* D42, 1385 (1990).

[18] P. Straub et al., *Phys. Rev. Lett.* 68, 452 (1992).

[19] D.M. Alde et al., *Phys. Rev. Lett.* 66, 2285 (1991).

[20] M.R. Adams et al., (E665 Collaboration), *Z. Phys.* C61, 179 (1994).

[21] J. Ashman et al., (EMC), *Z. Phys.* C52, 1 (1990).

[22] D.S. Barton et al., *Phys. Rev.* D27, 2580 (1983).

[23] T. Fields, *Nucl. Phys.* A544, 565 (1992).

[24] G. Marchesini et al., HERWIG V5.6, CERN (1993).

[25] R. Brun et al., GEANT3 User's Guide, CERN DD/EE/84-1.

[26] E. Engels et al., *Nucl. Instr. Meth.* A279,272 (1989).

[27] S. Mani, Ph. D. Thesis, University of Pittsburgh (1986).

[28] J. Kemmer, *Nucl. Instr. Meth.* 169 (1980) 499.

[29] NATO series, Techniques and Concepts of High Energy Physics IV, edited by T. Ferbel, Plenum Press, New York (1987).

[30] D.D.S. Weerasundara, Ph. D. Thesis, University of Pittsburgh (1993).

[31] K. Hartman, Ph. D. Thesis, Pennsylvania State University (1990).

[32] C. Bromberg et al., *Nucl. Instr. Meth* A307, 292 (1991).

[33] W.E. DeSoi, Ph. D. Thesis, University of Rochester (1990).

[34] F. Lobkowicz et al., *Nucl. Instr. Meth.* A235, 332 (1985).

[35] C. Lirakis, Ph. D. Thesis, Northeastern University (1990).

[36] R. Benson, Ph. D. Thesis, University of Minnesota (1990).

[37] IEEE Standard FASTBUS, (1985), ISBN 471-84472-1.

[38] W. Dlugosz, Ph. D. Thesis, Northeastern University (1994).

[39] N. Varelas, Ph. D. Thesis, University of Rochester (1994).

[40] L. Sorrell, E706 Internal Note 201.

[41] G.O. Alverson, E.L. Pothier, E706 Internal Note 139 (1985).

[42] H.J. Klein, J. Zoll, PATCHY Reference Manual, CERN (1983).

[43] R. Brun et al., ZEBRA User's Guide, CERN DD/EE/85-6.

[44] S. Blusk, Ph. D. Thesis, University of Pittsburgh (1995).

[45] P. Chang, Ph. D. Thesis, Northeastern University (1994).

[46] J.P. Mansour, Ph. D. Thesis, University of Rochester (1989).

[47] H.U. Bengtsson, T. Sjostrand, *Comp. Phys. Comm* 46, 43 (1987).

[48] T.D. Gottschalk, Supercollider Phys., 94. (1985).

[49] R.M. Roser, Ph. D. Thesis, University of Rochester (1994).

[50] V. Zutshi, private communication.

[51] D.S. Brown, Ph. D. Thesis, Michigan State University, (1993).

[52] P. Bordalo *et al.,* Phys. Lett. B 193, 373 (1987).

[53] M. Zielinski, Nuclear Effects in High p_T Production of Nuclear Mesons and Direct Photons, Proceeding of 5th Conference on the Intersections of Particle and Nuclean Physics, St. Petersburg, Florida (1994).

[54] D. Naples et al., (E683 Collaboration), Phys. Rev. Lett. 72, 2341 (1994).